DESIGNING COMPOSITE-BASED CYLINDRICAL STRUCTURES AND MANUFACTURING COMPOSITE PROTOTYPES BY FILAMENT WINDING METHOD

A Thesis Submitted to
The Graduate School of
İzmir Institute of Technology
in Partial Fulfillment of the Requirements for the Degree of

DOCTOR OF PHILOSOPHY

in Mechanical Engineering

by
Seçkin MARTİN

June 2024

İZMİR

We approve the thesis of **Seçkin MARTİN**

Examining Committee Members:

Prof. Dr. Metin TANOĞLU
Department of Mechanical Engineering, İzmir Institute of Technology

Prof. Dr. Hatice Seçil ARTEM
Department of Mechanical Engineering, İzmir Institute of Technology

Prof. Dr. Engin AKTAŞ
Department of Civil Engineering, İzmir Institute of Technology

Prof. Dr. Evren Meltem TOYGAR
Department of Mechanical Engineering, Dokuz Eylül University

Doç. Dr. Seçkin ERDEN
Department of Mechanical Engineering, Ege University

28 June 2024

Prof. Dr. Metin TANOĞLU
Supervisor, Department of
Mechanical Engineering
İzmir Institute of Technology

Prof. Dr. M. İ. Can DEDE
Head of the Department of
Mechanical Engineering

Prof. Dr. Mehtap EANES
Dean of the Graduate School

ACKNOWLEDGMENTS

First of all, this Ph.D. thesis was jointly conducted within the scope of the TÜBİTAK (Scientific and Technological Council of Turkey) 2244-industrial PhD—program, including institutes including IZTECH and TAI (Turkish Aerospace Industries) TUBİTAK. So I am deeply thankful for their financial support (project number: 118C086) and collaboration.

I would like to express my thanks to Prof. Dr. Metin TANOĞLU for his helpful comments and for giving me the opportunity to participate in TÜBİTAK 2244- Industry Ph.D. program.

I would like to thank my PhD thesis jury members, Prof. H. Seçil ARTEM, Prof. Engin AKTAŞ, Prof. Dr. Meltem Evren TOYGAR, and Assoc. Dr. Seçkin ERDEN for their useful comments.

I would particularly like to sincerely thank Prof. Dr. H Seçil ARTEM for the support she has given me during the difficult processes I have gone through in my personal life.

I would like to thank to my lab. mates and friends M.Erdal ULAŞLI, Kaan NUHOĞLU, Mert ÖZKAN, Ceren TÜRKDOĞAN, Dora ÖZARSLAN, Mesut BAYHAN and the rest of other colleagues for their help and unconditional support.

I would like to thank my father Bahtiyar MARTİN, my mother Yıldız MARTİN and my sister Miray MARTİN for their unconditional love and support.

I would like to wholeheartedly thank my beloved spouse, Dilan MARTİN, for her unconditional support, understanding, and dedication throughout my entire doctoral journey. She has devoted her life to this process as much as I have and shown immense patience during the countless hours I spent in front of the computer.

Finally, I would like to thank the unsung academic heroes who offer reliable open-source contents on Youtube, Udemy or GitHub.

ABSTRACT

DESIGNING COMPOSITE-BASED CYLINDRICAL STRUCTURES AND MANUFACTURING COMPOSITE PROTOTYPES BY FILAMENT WINDING METHOD

This study reports the design, finite element modeling, optimization, fabrication and testing of relatively thick (radius/thickness ~ 7) and long carbon fiber reinforced polymers produced by filament winding against buckling damage under axial loading. The optimum winding angle and stacking sequence against Linear (Eigenvalue) buckling were determined in accordance with the predetermined design requirements utilizing genetic algorithm (GA) optimization via MATLAB. During the optimization process, the critical buckling load factor (λcr) was assigned as objective function, design constraints were natural frequency (fn) and angle of twist (Φ), and ply angles were considered to be variable and restricted with 20 to 87-degree continuous fiber angles in the laminate sequences. As a consequence of the test results, λcr of the proposed optimum model was found to be 3.2 times better than the reference model and both the analytical and finite element model satisfactorily predicted the critical buckling load for all CFRP rods consistent with the test results. The critical buckling loads calculated by applying a KDF of 0.95 for the finite element model and a KDF of 0.9 for the analytical solution were found to be reasonably appropriate for use in the preliminary design input. Additionally, results showed that a higher axial to the circumferential ratio of axial and bending stiffness (A11/A22, D11/D22) promises better buckling performance than other possible candidates. Finally, the microstructures of the produced rods were examined and the fiber volume ratios were calculated by means of chemical characterization.

ÖZET

KOMPOZİT ESASLI SİLİNDİRİK YAPILARIN TASARLANMASI VE FİLAMENT SARMA YÖNTEMİ İLE KOMPOZİT PROTOTİP İMALATI

Bu çalışma, eksenel yükleme altında burkulma hasarına karşı filament sargı ile üretilmiş nispeten kalın (yarıçap/kalınlık ~ 7) ve uzun karbon fiber takviyeli polimerlerin tasarımını, sonlu eleman modellemesini, optimizasyonunu, üretimini ve testini rapor etmektedir. Optimum sarım açısı ve katman sıralaması, genetik algoritma (GA) optimizasyonu kullanılarak MATLAB aracılığıyla belirlenen tasarım gereksinimlerine göre Lineer (Özdeğer) burkulmaya karşı belirlendi. Optimizasyon sürecinde, kritik burkulma yük faktörü (λ_{cr}) hedef fonksiyon olarak atanmış, tasarım kısıtlamaları doğal frekans (f_n) ve burulma açısı (Φ) olarak belirlenmiş ve katman açılarının sürekli fiber açıları 20 ile 87 derece arasında değişken olacak şekilde sınırlanmıştır. Test sonuçlarının bir sonucu olarak, önerilen optimum modelin λ_{cr} değeri referans modelden 3.2 kat daha iyi olduğu bulunmuş ve hem analitik hem de sonlu eleman modeli, tüm CFRP çubuklar için test sonuçlarıyla tutarlı olarak kritik burkulma yükünü tatmin edici bir şekilde tahmin etmiştir. Sonlu eleman modeli için 0,95 KDF ve analitik çözüm için 0,9 KDF uygulanarak hesaplanan kritik burkulma yüklerinin ön tasarım girdisinde kullanılması nispeten uygun bulunmuştur.Ayrıca, sonuçlar, eksenel ve eğilme rijitliklerinin eksenelden çevresel oranın (A11/A22, D11/D22) diğer olası adaylardan daha iyi burkulma performansı vaat ettiğini göstermiştir. Son olarak, üretilen çubukların mikro yapıları incelenmiş ve fiber hacim oranları kimyasal karakterizasyon yoluyla hesaplanmıştır.

TABLE OF CONTENTS

LIST OF FIGURES

Figure **Page**

Figure **Page**

Figure **Page**

Figure **Page**

LIST OF TABLES

CHAPTER 1

INTRODUCTION

In the last fifty or sixty years, modern composites have emerged and are now widely used in a wide range of technical applications, including aerospace, automotive, sports goods, etc. By way of example, CFRP composites are utilized in the automobile sector to produce body panels, chassis components, and internal parts, which considerably reduces vehicle weight, promotes fuel economy, and lowers CO_2 emissions. Similarly, CFRP composites are widely used in the sports goods sector for enhancing the functionality and endurance of high-performance products including racing boats, bicycles, tennis rackets, and golf clubs. CFRP composites are greatly beneficial in both areas owing to such benefits. However, aerospace structures that require high strength-to-weight and stiffness-to-weight ratios are an area where modern composites are particularly promising.[1–4] Figure 1.1 illustrates schematically the comparison of conventional materials and composite materials.

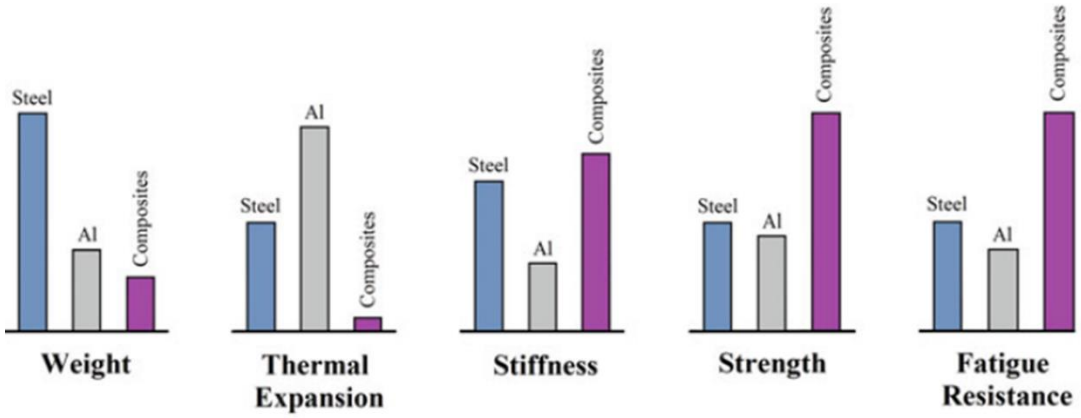

Figure 1.1 Comparing composite materials with traditional monolithic materials. (Source: Krishan K. Chawla, 2019)

Focusing on aircraft, their materials must meet many tight requirements for optimum performance and safety.[5] They must have a high load-carrying capacity while remaining light to preserve the structural integrity required to convey passengers and goods. Long service lives, resistance to environmental factors, and the ability to tolerate damage without catastrophic failure are other requirements for these materials to

maximize financial benefits. Easy manufacturing and repair to save expenses and downtime, as well as affordability, are also prerequisites.

The use of composite materials in both military and commercial aircraft has increased significantly over time, as Figure 1.2 illustrates. Boeing's 737 spoiler marked the beginning of the use of composites in civil aviation nearly three decades ago. The trend has continued with the 737 Classic and Next Generation models, 757, 767 and 777, replacing light alloys with composites to produce control surfaces and empennage, making them lighter and requiring less maintenance.[6] In addition, the Airbus A320, A330, A380, A380, A350 and Bombardier C Series have all turned to composite as the main material, resulting in a significant reduction in aircraft weight, improved fuel efficiency and reduced CO_2 emissions.[7]

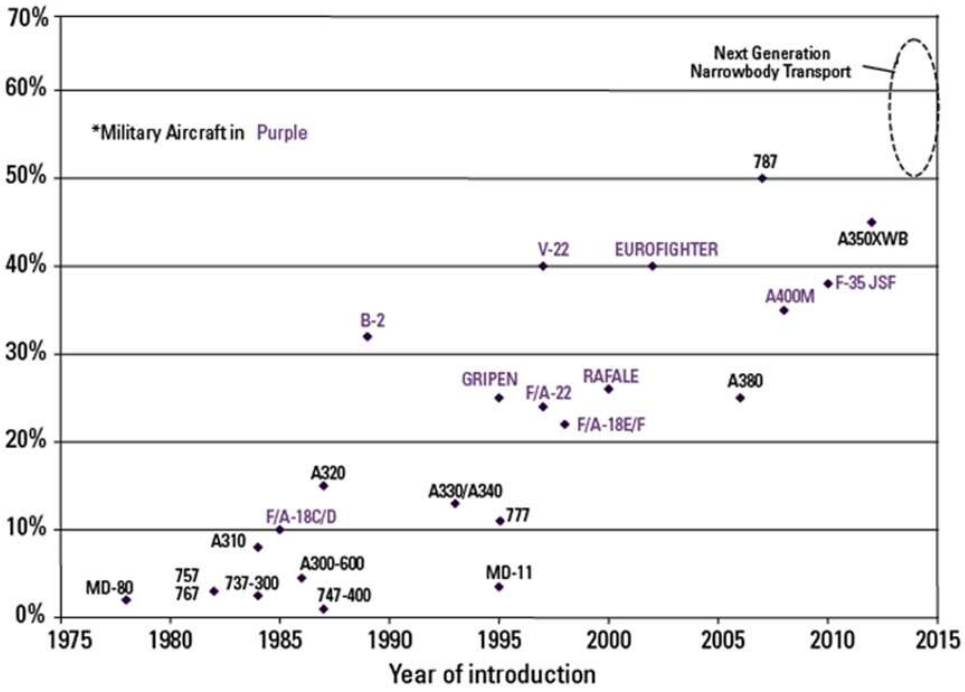

Figure 1.2 The proportion of weight increase in composite structures on significant aircraft programs.(Source: Smith, 2013)

As depicted in Figure 1.2, the 787 aircraft has a 50% structural use of composites. Given its all-composite skin, fuselage, wing box and propeller, the 787 marked a tremendous breakthrough as the first passenger aircraft to be built entirely from composite materials (see Figure 1.3).

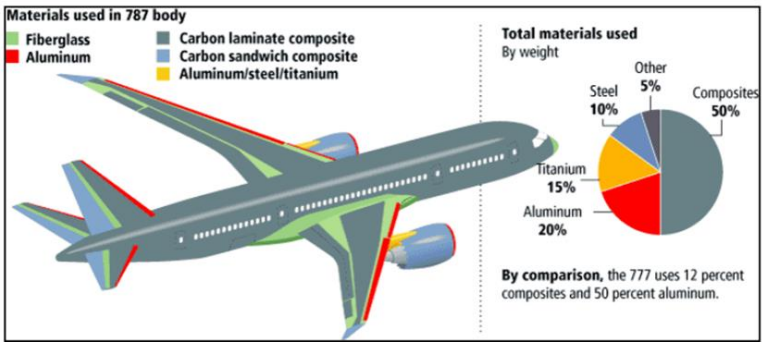

Figure 1.3 The use of composites by weight on the Beoing 787 Dreamliner

Apart from laminated or sandwich panels such as skin, fuselage, wing box, or control surfaces, cylindrical aviation structures, including rocket motor cases, struts, rods, pressure vessels, shafts, and antenna masts, are also produced from carbon or glass-reinforced polymer matrix composites. In this respect, several examples have been shared in Figure 1.4.[8,9]

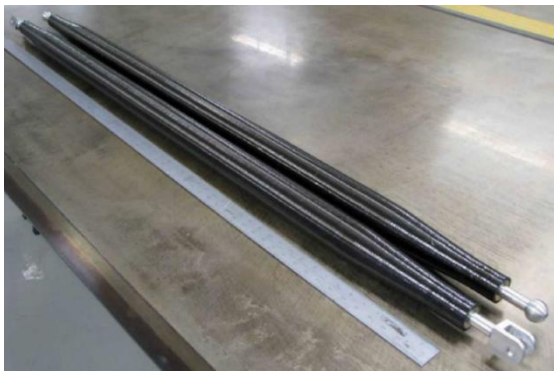

(a)

(b)

Figure 1.4 Structural examples of cylindrical composites (a) struts, (b) pressure vessel, and (c) hybrid drive shaft

(cont. on next page)

(c)

Figure 1.4 **(cont.)**

CFRP struts in aerospace applications are lighter and more robust than traditional materials, thus improving the overall efficiency of the aircraft. Similarly, CFRP pressure vessels benefit from the low weight and considerable strength of the material, which is necessary to minimize extra weight while maintaining structural integrity, while CFRP or hybrid drive shafts outperform conventional drive shafts in terms of corrosion resistance, design flexibility, and vibration damping.

On the other hand, the airworthiness of every part developed, designed or modified must be verified and its components tested in accordance with the regulations established by the European Aviation Safety Agency (EASA) and the Federal Aviation Administration (FAA).[5]

The building block approach (BBA), broadly acknowledged in the aerospace industry, is a well-organized process that starts with coupons and progresses to full-scale components for comprehensive testing to generate and ultimately design data. Concurrently, statistical methods (A and B basis), analysis methods (Finite Element Modeling) and non-destructive testing methods (Tap, AUTT etc.) also contribute to this process as supporting technologies. This approach allows each level of the structure to be thoroughly evaluated for strength and performance before moving on to more complex assemblies, ultimately ensuring the integrity of the entire structure like an aircraft. An example schematic representation is shared in Figure 1.5.

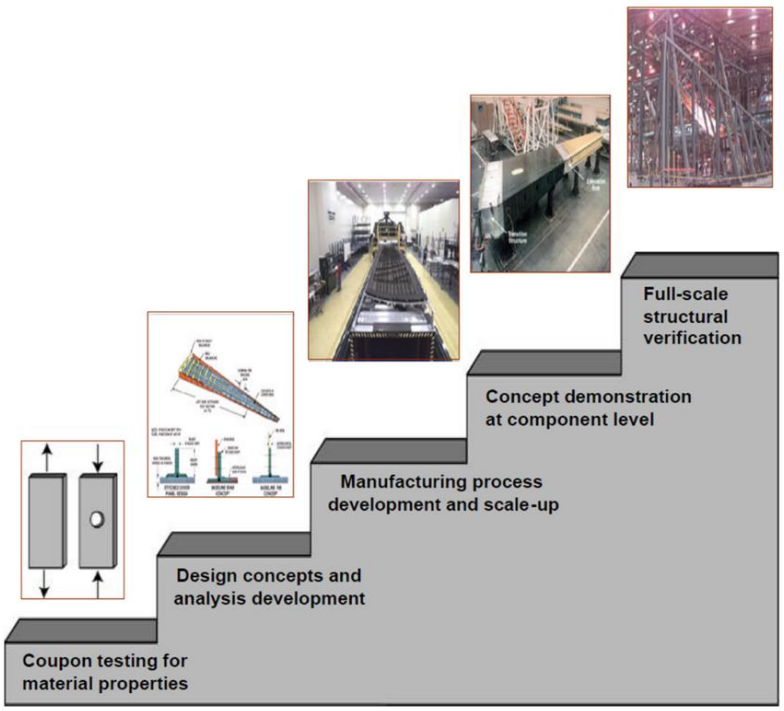

Figure 1.5. Building Block Approach

This thesis investigates the design, finite element modeling, optimization, fabrication and testing of relatively thick (radius/thickness ~7) and long (800 mm) carbon fiber reinforced polymers produced by filament winding to be used as rods in aircraft for buckling damage under axial loading. The optimum winding angle and stacking sequence against Linear (Eigenvalue) buckling were determined in accordance with the predetermined design requirements utilizing genetic algorithm (GA) optimization via MATLAB. During the optimization process, the critical buckling load factor (λ_{cr}) was assigned as the objective function, design constraints were natural frequency (f_n) and angle of twist (Φ), and ply angles were considered to be variable and restricted with 20 to 87-degree continuous fiber angles in the laminate sequences. The outcomes of the research are reported under the following headings.

1.1. Motivation and Aim of the Study

The main goal of this thesis is to design, optimize, and manufacture composite rods with optimized filament winding and layer arrangement according to the desired boundary conditions by evaluating the natural frequency and torsion angle of cylindrical composite structures subjected to axial loading within the given boundary conditions.

To the best of the author's knowledge, there is no study in the literature on the buckling of relatively thick (radius/thickness ~ 7) CFRP rods. It also aims to verify both the buckling analysis of the finite element model and analytical solution with smeared properties created after mechanical characterization.

The use of composite materials in the aerospace industry, where weight reduction is essential for enhancing performance and fuel efficiency, is a major driving force behind this study. By substituting composite rods for traditional aluminum and steel rods, aircraft weight could potentially significantly be decreased, resulting in lower fuel consumption and increased payload capacity. The objectives of the study are also set out in bullet points below.

- Use of filament winding process in the production of composite reinforced polymer matrix composite rods to substitute two force member conventional aluminum, steel rods.
- Mechanical property characterization of CFRP plates produced by filament winding method.
- Investigation of thermo-mechanical properties of CFRP.
- Using Genetic algorithm (GA) to optimize the ply orientation to yield the desired results under given boundary conditions.
- Using classical lamina theory, calculation of A and D matrices to determine whether the produced CFRP bars can support given axial loads.
- Finite element modeling (ANSYS) of eigenvalue buckling, natural frequency and angle of twist of CFRP rods by employing the properties obtained from characterization and determining knock-down factor (KDF)
- Analytical solution of CFRP rods by means of smeared properties to find KDF.
- Performing buckling tests of non-optimized and optimized rods with ply orientation produced by filament winding.
- Conducting fiber volume fraction calculations of the produced CFRP rods and
- Investigation of microstructure of CFRP rods by optical and scanning electron microscopy

1.2. Novelty of the Thesis

Although CFRP composites are used in many fields such as defense and aerospace, when the literature is examined, it is seen that, to the author's knowledge, there are no studies focusing on the buckling damage of relatively thick (radius/thickness ~ 7) and long (800mm) CFRP rods.

This study reports the design, finite element modeling, optimization, fabrication and testing of relatively thick (radius/thickness ~ 7) and long carbon fiber reinforced polymers produced by filament winding against buckling damage under axial loading. The optimum winding angle and stacking sequence against Linear (Eigenvalue) buckling were determined in accordance with the predetermined design requirements utilizing genetic algorithm (GA) optimization via MATLAB. During the optimization process, the critical buckling load factor (λ_{cr}) was assigned as objective function, design constraints were natural frequency ($f_{n)}$ and angle of twist (Φ), and ply angles were considered to be variable and restricted with 20 to 87-degree continuous fiber angles in the laminate sequences. The findings of this study make a unique contribution to the literature because there is no theoretical or experimental study on the optimization of the buckling behavior of rods with the radius/thickness ratio and length reported in the literature.

In addition to that, this thesis presents a highly optimized, performance-driven approach to the design and execution of composite materials in engineering structures despite aiming to fill a gap in the literature. The outcomes suggest new options for producing lightweight, high-strength components in numerous industrial applications without compromising mechanical properties, particularly in aircraft where weight reduction is crucial, and promise to make a substantial contribution to composite materials engineering.

CHAPTER 2

COMPOSITE MATERIALS AND LITERATURE SURVEY

In order to create composite materials, two or more different materials are combined to produce enhanced properties beyond those of the constituent parts. A matrix and fibers are the main components of composites. The matrix binds the fibers and transfers the load between the fibers and the composite to external loads and supports. The fibers provide much of the stiffness and strength of the material. The fibers are also protected by the matrix against damage from the environment. Additional materials, such as fillers, can be added to improve needed qualities further. Fillers can improve dimensional stability and processability and minimize costs.[5,10–12]

Composites have the following attractive properties compared to traditional materials[13]:

- Low density
- High strength-to-weight ratio
- Fatigue resistance
- Corrosion resistance
- Easy to tailor requested properties
- Impact and damage tolerance
- Providing demanding properties

This list can be expanded and modified depending on the type of reinforcement material and matrix material. In this regard, Composites are classified according to both the matrix materials and the type of reinforcement materials. Details will be explained in the following sub-headings.

When focusing on composite applications in aerospace, it is crucial to be able to meet the design requirements of light weight, fatigue, corrosion resistance and impact and damage tolerance without compromising the demanding requests. More weight reductions convert into enhanced efficiency, greater payloads, more extended range, and decreased fuel consumption. The overall structural efficiency of 7075-T6 aluminum, Ti-6Al-4V, and carbon/epoxy is evaluated in Figure 2.1.

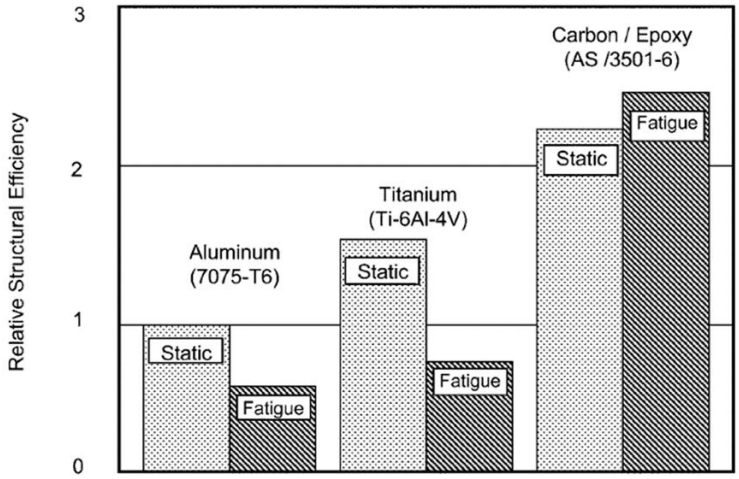

Figure 2.1 In comparison structural effectiveness of materials used in aerospace. (Source: Campbell, 2010)

2.1. Classification of Composite Materials

As mentioned above, under this heading, the classification of composites based on the reinforcing material and then based on the matrix material are explained respectively.

2.1.1. Classification by type of reinforcement materials

In composites, reinforcements can be particles, whiskers or fibers. Schematic presentation of reinforcement materials can be seen in Figure 2.2.

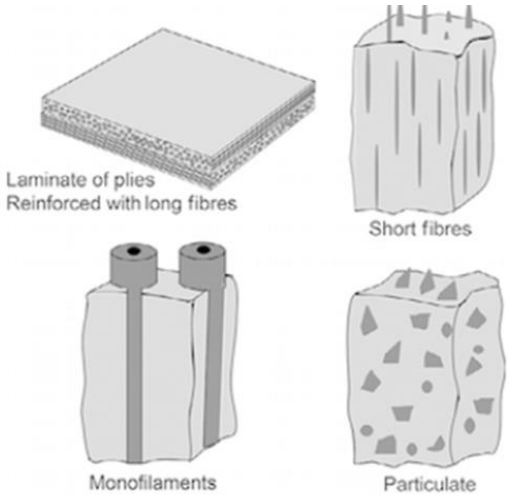

Figure 2.2 Different reinforcement configuration types

For fundamental instance of particulate reinforced composites, concrete is a particulate composite consisting of two types of particles: sand and stones, and cement operates as a matrix. On the other hand, the particle can be micron or nano-sized and can contribute to improving the desired properties (e.g. nanographene particles are employed to improve the wear behavior of metals).[2,14] Short or discontinuous fibers are also preferred for improving mechanical or physical properties due to their random orientation. However, continuous long fiber reinforced composites are preferred in aircraft structures compared to other reinforcement materials due to the high strength and modulus of the fibers. Glass, carbon, or Kevlar are some of the fiber materials that can be utilized in composites, depending on the application areas and cost considerations.

In Figure 2.3, a comparison of the strength values of conventional materials and fibers is shared.

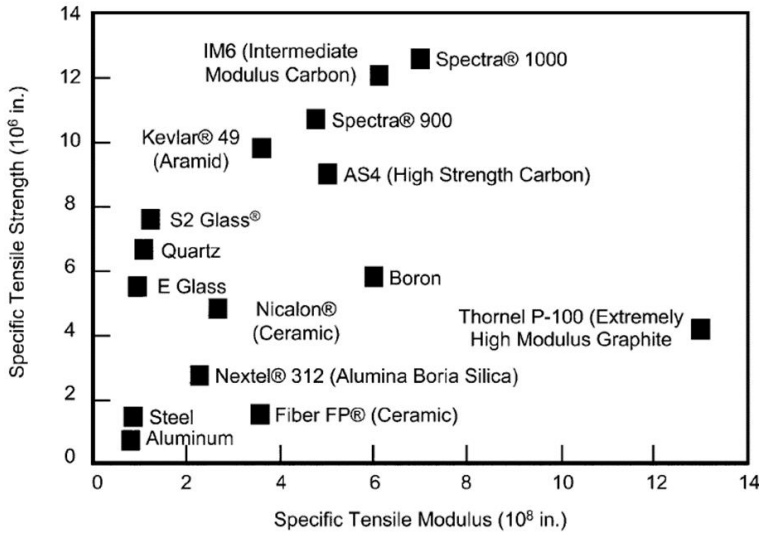

Figure 2.3 Strength and modulus comparison of several fibers and traditional materials

On the other hand, to provide the desired properties, continuous fibers are used as lamina (layer or ply) or laminate (several laminas stacked and bonded). In this way, for example, a composite rod, which works as two force members in the axial direction, can provide the desired stiffness value much lighter than conventional materials by stacking its plies at an angle of 0 and 90 degrees. Therefore, when calculating the mechanical properties of a predetermined stacking sequence, each lamina can be considered homogeneous for the purpose of estimating the elastic properties of the component as a whole, since the volume fraction and fiber distribution are constant everywhere. As a result, the properties of the laminate can be calculated for any given stacking sequence.

The flow for the calculation of structural element mechanical properties is shown in Figure 2.4.

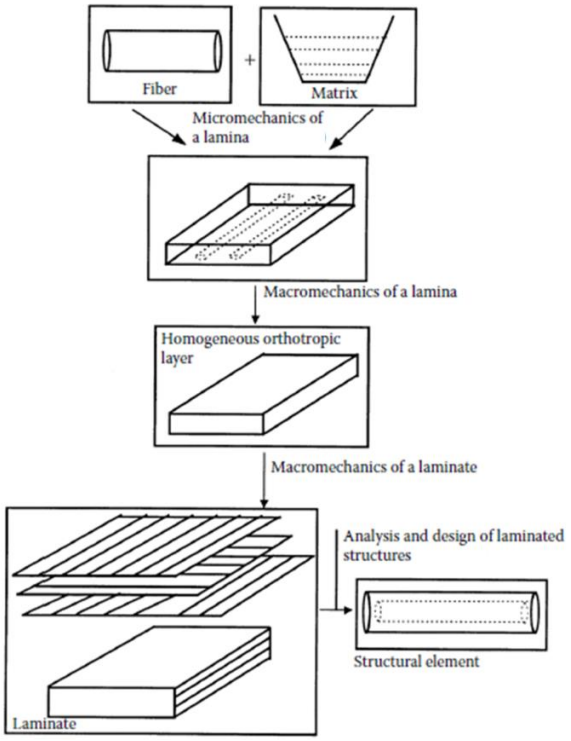

Figure 2.4 Mechanical properties calculation procedure of composites.

2.1.2. Classification by type of matrix materials

Composites can be categorized based on their matrix material, namely polymers (PMC), metals (MMC) or ceramics (CMC). In order to set a general framework, the properties of relatively common matrix materials are presented in Table 2.1.

Table 2.1 Outline of the properties for different matrix types.

Matrix	Density ρ (kg m^{-3})	Young's modulus E (GPa)	Shear modulus G (GPa)	Poisson ratio ν	Tensile strength σ_* (GPa)	Thermal expansivity α ($\mu\varepsilon$ K^{-1})
Epoxy	1250	3.5	1.27	0.38	0.04	58
Polyester	1380	3.0	1.1	0.37	0.04	150
Polyether ether ketone (PEEK)	1300	4	1.4	0.37	0.07	45
Polycarbonate	1150	2.4	0.9	0.33	0.06	70
Polyurethane rubber	1200	0.01	0.003	0.46	0.02	200
Aluminium	2710	70	26	0.33	0.1–0.3	24
Magnesium	1740	45	7.5	0.33	0.1–0.2	26
Titanium	4510	115	44	0.33	0.4–1.0	10
Borosilicate glass	2230	64	28	0.21	0.05	3.2

While the addition of reinforcement in metal matrix typically results in only relatively moderate improvements in stiffness, significant improvements in properties such as resistance to thermal degradation, wear, and creep behavior can yet be observed. In contrast, compared to metals, ceramics have relatively few possible slip systems and strong covalent and ionic bonds. Therefore, ceramics are known to have low failure strains as well as low toughness or fracture energies, and the aim of ceramic composite making is to relatively improve these properties with reinforcing materials.[15,16]

On the other hand, the most commonly used types of composite materials are PMCs, categorized according to whether the matrix is made of thermoset or thermoplastic polymers. Regardless of whether the polymer matrix is thermoset or thermoplastic, PMCs are considerably simpler to manufacture than metal or ceramic-matrix composites. This is mainly because the production of polymer-matrix composites needs relatively low processing temperatures and hence low cost.[13,17]

Properties of thermoset and thermoplastic composites are listed in Table 2.2.

Table 2.2 Comparison of thermoset and thermoplastic matrix composites. (Source: Chung, 2010)

Properties	Thermoset-Matrix Composites	Thermoplastic-Matrix Composites
Curing Process	Requires curing	No cure required
Shelf-life	Limited	Unlimited
Reprocessing	Not possible	Possible (for repair and recycling)
Health Risks	+ due to chemicals during processing	Fewer health risks due to chemicals during processing
Thermal shaping	Not possible	Possible
Toughness	-	+ (better damage tolerance)
Environmental Tolerance	-	+
Processing Temperatures	-	+
Viscosities	-	+
Prepreg Handling	Drapeable and tacky when a solvent is used	Stiff and dry without a solvent

By adding continuous fibers, including glass, carbon or aramid, toughness, stiffness, creep and wear resistance of polymer matrix can be tailored.

The aircraft industry is one of the industries that employ carbon fiber composites for which combinations of lightness, stiffness, and strength are highly attractive.

Composite materials are frequently utilized in spacecraft applications because they save weight and provide dimensional stability.[18,19]

Since CFRPs are studied in this thesis, this subject will be focused in the following chapters.

2.2. Manufacturing Techniques of FRP Composites

The temperature required to form the part and curing the matrix, the type of fibers and matrix, and the cost effectiveness of the procedure drive the choice of manufacturing process. When designing a composite structure, the manufacturing process is usually considered primarily. The factors mentioned above include cost, production volume, production speed and potential advantages of the production technique to produce the desired structure.

There are various production methods for continuous fiber composites in the literature and industry, such as hand lay-up, vacuum bagging, autoclave processing, resin vacuum-assisted resin transfer molding, pultrusion and filament winding. Details of these production methods are described in the following sections. In this thesis, continuous carbon fiber is used with thermosetting resin, so production methods and examples will be aligned in this context.

2.2.1. Hand Lay-up

Wet lay-up, another name for the hand lay-up technique, is the most traditional and simple production method. In general, it requires the hand placement of dry reinforcements on the mold followed by the application of resin. A schematic representation of the hand lay-up production method is shown in Figure 2.5.

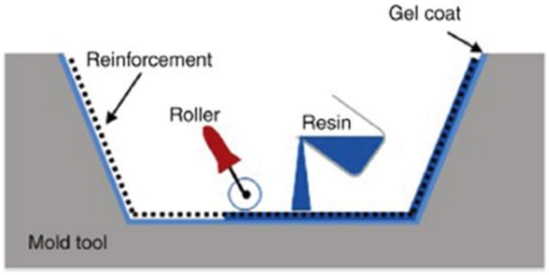

Figure 2.5 Hand lay-up operation. (Source: Long, 2005)

The hand lay up production method has applications in marine, aerospace, structural and consumer fields.

2.2.2. Vacuum Bagging

A curing technique known as vacuum bagging is employed to produce composites with higher fiber content and better porosity. A plastic film or bag is typically used to seal a composite that is assembled into the tool by hand. A vacuum pump is used to evacuate the air from the bag, subject the material to one atmosphere of pressure and produce a composite with improved properties, e.g. better fiber volume fraction if the composite is hand lay-up and lower porosity if it is prepreg. Figure 2.6 illustrates the schematic representation of the vacuum bagging method.

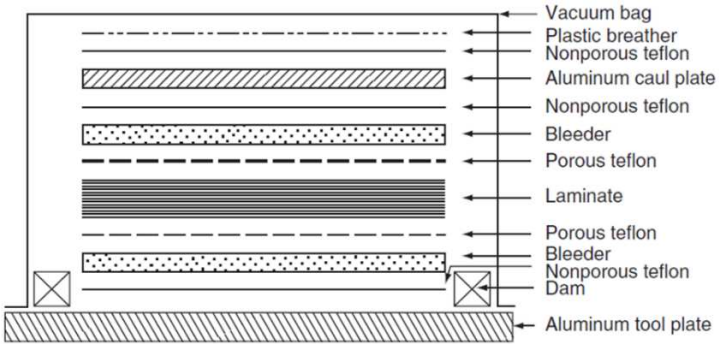

Figure 2.6 Schematic representation of vacuum bagging process.
(Source: Mallick, 2007)

2.2.3. Autoclave

The autoclave production technique of composites is an advancement of vacuum bag technology and enables greater compaction and void elimination at a higher pressure than vacuum. In an autoclave, practically any form can be cured as the gas pressure is isostatically applied to the designed component. In addition to the pressure, the temperature is also increased to initiate the curing of the polymer. In parallel with lowering the viscosity of the polymer, higher temperatures contribute to the consolidation and wetting of the reinforcement within the composite. In addition to curing very large parts such as aircraft wings and marine structures, many relatively small parts can also be cured in an autoclave.

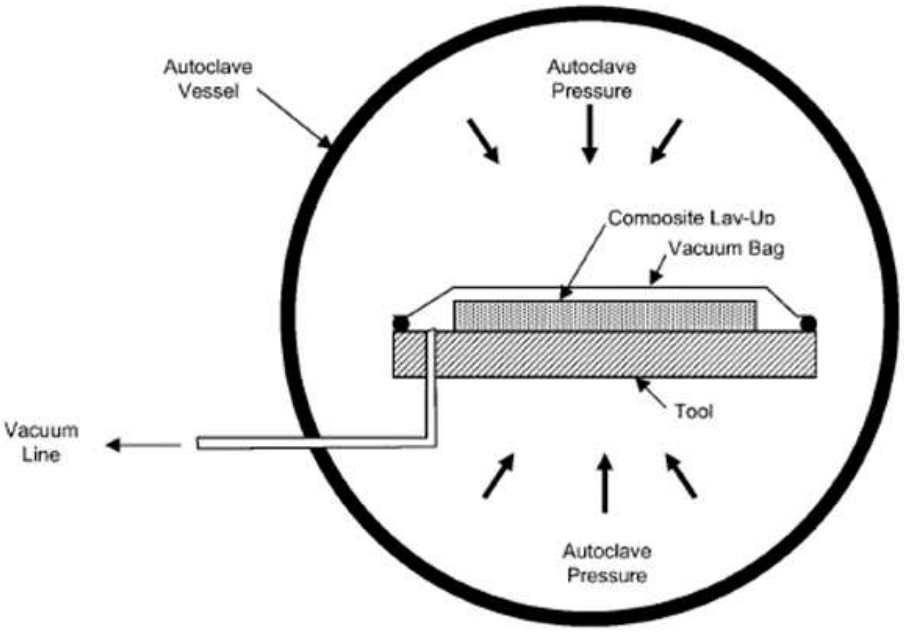

(a)

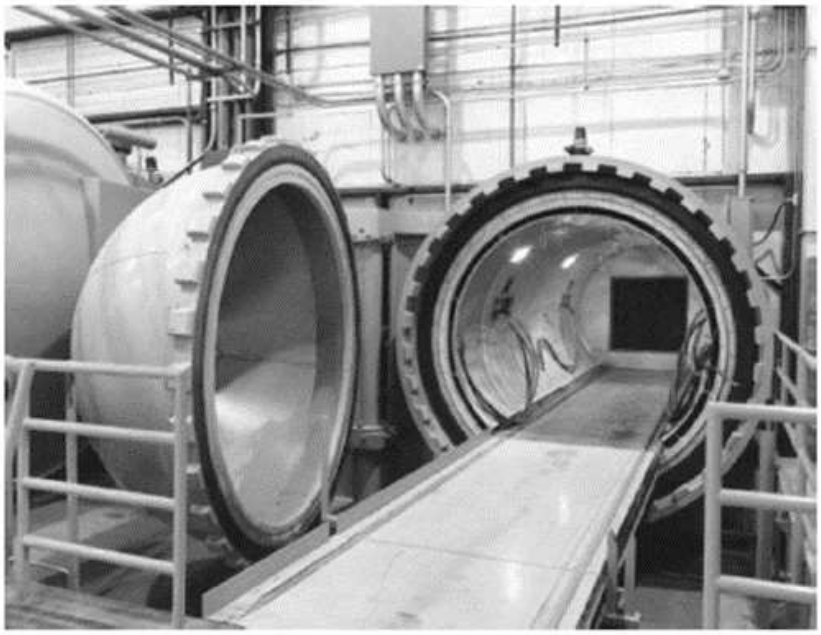

(b)

Figure 2.7 Autoclave process, (a) schematic representation, and (b) real-life example. (Source: Campbell, 2010)

2.2.4. Vacuum-Assisted Resin Transfer Molding (VARTM)

The lay-up is impregnated with thermosetting resin, usually injected under a pressure of 2 to 20 bar. The resin can be introduced in more than one place to accelerate its slow flow. The procedure depends on parameters such as the viscosity of the resin, pressure variations within the tool and the permeability and architecture of the lay-up. A vacuum is applied to draw the liquid resin from an external reservoir into the layer, and this process continues until there is no dry spot in the lay-up. When the lay-up is totally soaked by means of transferred resin, it is allowed to cure at desired conditions. The process can be seen in Figure 2.8.

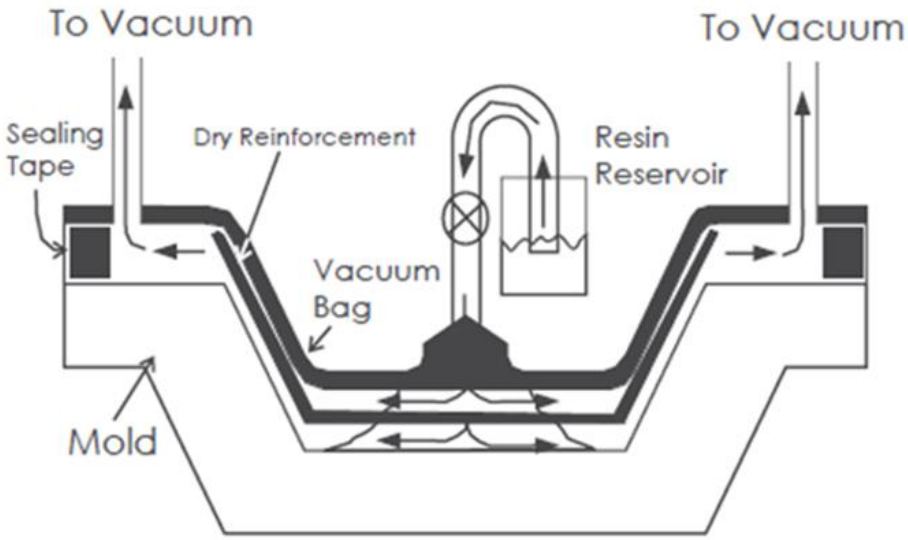

Figure 2.8 VARTM process

2.2.5. Pultrusion

This method produces continuous sections of fiber-aligned polymer matrix composites, mostly axially orientated. Solid bars, hollow tubes, flat sheets and beams with various cross-sections such as angles, channels, hat sections and wide flanged sections are among the products that are often pultruded. However, the major disadvantage of this process is that it is not possible to control the fiber orientation during the manufacturing process, except for the use of fabric.

2.2.6. Filament Winding

Filament winding (FW) is a promising fabrication technique for cylindrical structures in which glass or carbon fibers are deposited at required angles in a predetermined pattern on a rotating mandrel. Filament-wound composite (FWC) structures are likely to provide high fiber volume fraction, precise angle deposition, ply orientation flexibility, and cost effectivity; hence they have a wide range of applications in demanding areas, including the automotive, aerospace, and marine industries.[1,20–26] Schematic presentation can be seen in Figure 2.9.

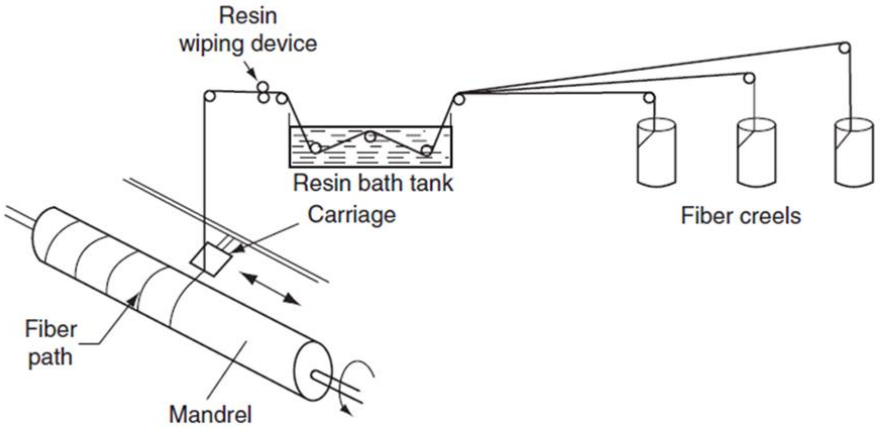

Figure 2.9 Filament winding setup. (Source: Mallick, 2007)

When considering the possible candidates for the production of cylindrical cross-section composites, they are hand lay-up, pultrusion and filament winding, respectively. Among these methods, filament winding is favored over the other production methods mainly due to the design flexibility on fiber orientation and automated production with low defect rates.[22–25,27–32]

Therefore, the filament winding method was chosen for filament-wound composite (FWC) rods, which are expected to meet the challenging boundary conditions that will be discussed in the following chapters.

2.3. Literature Survey

Carbon fiber reinforced polymers, or CFRPs, are a type of polymer composite that is of particular interest. Particularly useful in aviation, where every kilogram saved can

provide significant fuel savings and increased cargo capacity, CFRPs are characterized by remarkable strength-to-weight ratios. Under various loads, their significant tensile strength and stiffness ensure the structural integrity of aircraft components.[33,34]

Due to the corrosion resistance of CFRPs, these parts have a longer lifespan, which means less regular maintenance is required, reducing operating costs. These composites give designers the flexibility to seamlessly combine different structural elements and mold them into complex shapes, maximizing aerodynamic performance. The widespread use of CFRPs in vital aerospace parts such as fuselage sections, wings, tail structures, load bearing members (struts, rods) and interior components has significantly improved aircraft performance and design.[1,20,35,36]

Especially in aircraft applications, cylindrical carbon fiber-reinforced polymer matrix composites are becoming increasingly attractive. Given their ability to distribute loads and maintain structural integrity optimally, these cylindrical composites are useful when forming components such as fuselage frames, pressure vessels, and structural rods.[37–39] Cylindrical CFRPs are used in these applications due to their high strength and stiffness combined with the lightweight design required to maintain the overall performance and efficiency of the aircraft. Their capacity to withstand severe conditions in aircraft environments, such as high altitudes, fluctuating pressures, and extremely high temperatures, further validates their suitability for these vital uses. In conclusion, cylindrical carbon fiber-reinforced polymer matrix composites are a remarkable technological development that offers unique benefits for the design and maintenance of modern aircraft.

So far, the importance of composites, matrices, reinforcement types, and production methods has been briefly summarized. From this point on, the focus will be on these issues, as this study aims to design, optimize, producing rods by means of filament winding, and test carbon fiber-reinforced polymer matrix cylindrical rods according to the determined boundary conditions.

Due to their relatively high load-bearing capacity, the majority of the FWC structures are loaded in a membrane state.[40] Therefore, the stability of structures is a significant concern under compressive loads since buckling can result in catastrophic failure.[41–45] When replacing traditional materials with FWC, the desired requirement must be met and remain within reasonable limits, so optimizing parameters such as thickness[46–48], length [49], mean radius, ply orientation [50–55], and mechanical properties of constituent [56–58] play an essential role in the performance of FWC.

The literature contains several theoretical and experimental studies considering the aforementioned factors against critical buckling damage. Dawn C. Jegley[59] conducted a study to evaluate the structural efficiency of carbon-epoxy tapered struts by utilizing manufacturing, extensive analysis, commercial studies, and experimentation. The main concentration of this project is on the overloaded struts on the Altair lunar lander, some of which are significantly more loaded than struts used in applications such as satellites and telescopes. To meet lunar lander criteria, the strut must be tapered at both ends, complicating the design and reducing the manufacturing process. Figure 2.10 shows the appearance of the rods planned to be designed and manufactured on the spacecraft.

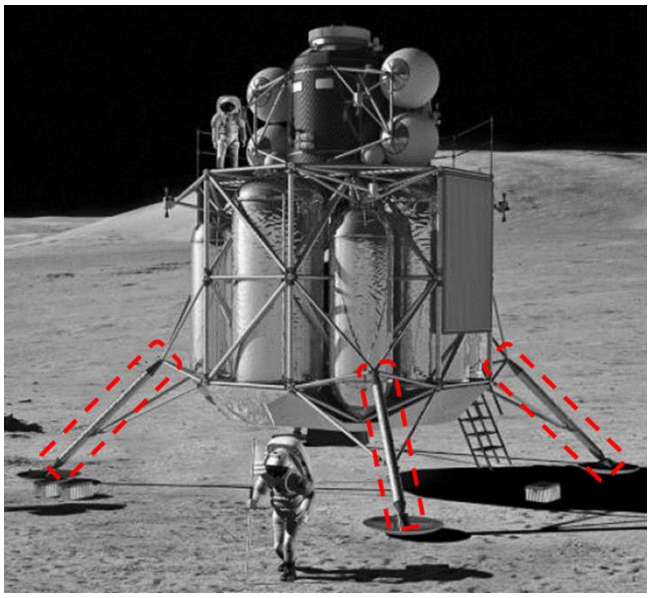

Figure 2.10 Altair lunar lander. (Source: Jegley et al., 2012)

A comprehensive analysis of various fibers, ply stacking arrangements, material strength allowances and strut shapes was conducted as part of the trade study to determine their effect on the weight of the strut assembly. Both strength-oriented failure mechanisms (e.g., exceeding failure strains) and stiffness-oriented failure mechanisms (e.g., buckling) were included in this analysis. The wide range of possible strut loads and geometries that can lead to markedly different behavior in different struts made this coupled approach crucial. As shown in Figure 2.11, the study showed that changes in stacking sequences have a significant impact on strut assembly weight, while diameter changes, which are barely noticeable, have a negligible impact. The optimum strut body diameter is approximately 6 inches when stacking sequences with plies of 0-30 ±45 degrees are analyzed. The most effective array has 63% 0-degree, 25% ±45-degree and

12% 90-degree plies in the axial direction. Remarkably, struts with only 0-degree plies weigh approximately the same as struts with 10% and 20% ±45-degree plies, indicating that these plies are useful for certain diameters and do not reduce efficiency. Off-axis loading and damage tolerance are not included in the Altair criteria, but ±45 degree plies are included to assess their impact. For such conditions, off-axis plies are used in conventional designs; therefore, it is critical to understand their effect on strut weight.

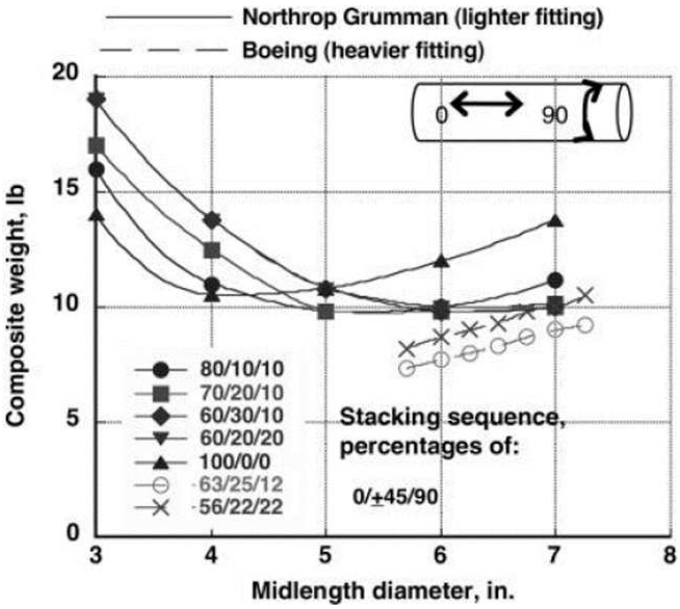

Figure 2.11 Influence of stacking sequence on weight and diameter.

Simply, 0-deg prepreg and 90-deg towpreg are deposited on the plaster mandrel and titanium inserts are placed at the beginning and end of the plaster mandrel at the beginning of production. For the strut design, which is 83.66 in. long and can withstand 107585 and 60000 lb. in compressive-tensile loadings, respectively, there were 16 to 18 layers in the composite strut bodies, according to Boeing or Northrop-Grumman research. The struts were intended to withstand 60,182 lb. of axial tensile load and 107,585 lb. of axial compressive load. The Northrop Grumman struts were stacked in $[90/0/\pm45/0/90]_s$, while the Boeing struts were stacked in $[\pm45/0/90/0]_s$. These sequences differ just by one ply, however the end-fitting and taper sections show more significant changes. Further, the failure load, stress distribution and buckling load of each manufactured strut were calculated by applying finite element analysis and results compared with experimental outputs. Regarding the experimental setup and finite element modeling illustrations can be seen in Figure 2.12.

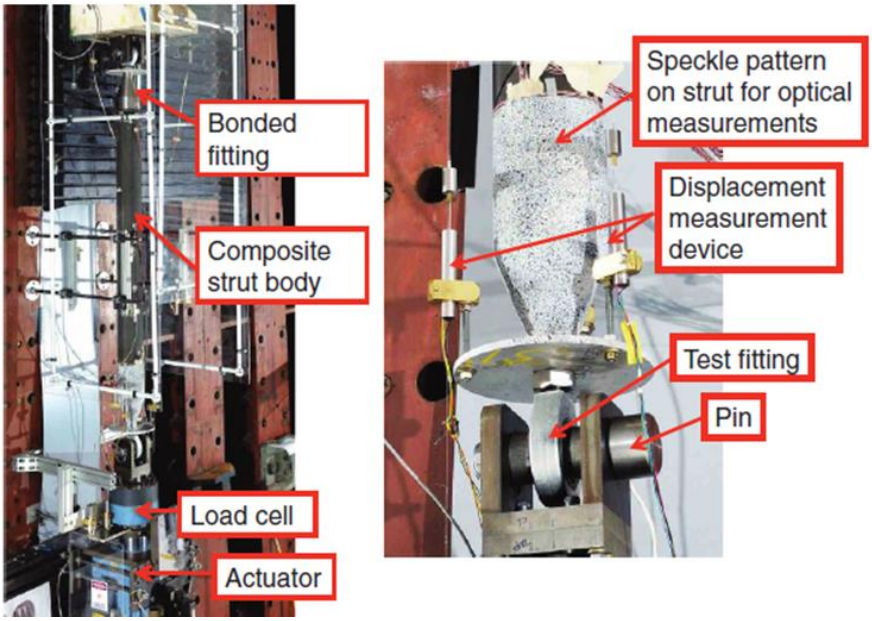

(a)

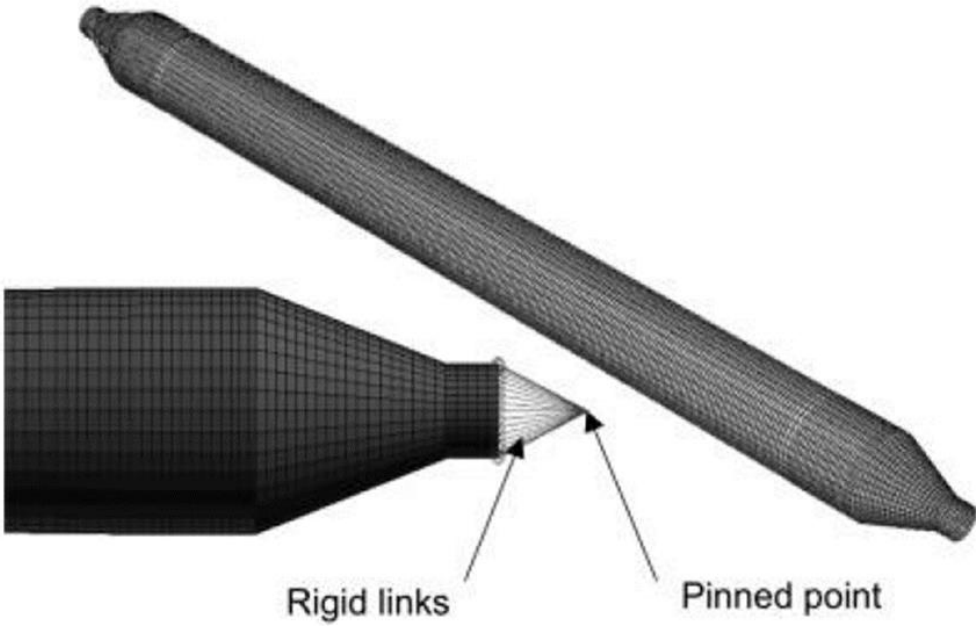

(b)

Figure 2.12 Images of (a) test setup, and (b)Finite element model

Figure 2.13 displays the structural efficiency of each strut design. The structural efficiency is visualized when the maximum compressive load of a strut is divided by its measured weight. Only undamaged struts starting compressive loading are included in this comparison. According to this metric, the highly loaded slotted plug-in struts, N-II-H, are the most structurally efficient struts.

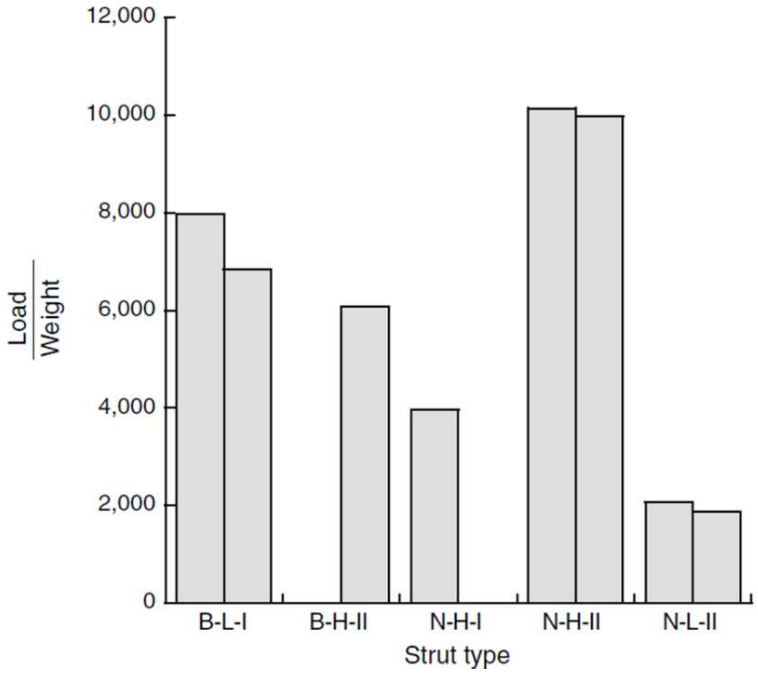

Figure 2.13 Structural efficiency of struts

As shown in the figure, while the finite element analysis and test results were consistent, more than 1.4 times the required compressive load was recorded in the tests, which is sufficient for the aviation static design limit criterion.[60] In addition, axial strain values were also reported to be within the desired range.

In conclusion, the weight difference between the composite and aluminum-lithium comparable struts is about 30% when the full set of struts with required loading range from 60,182 lb in tension to 107,585 lb in compression is taken into account. It can be attributed to the fact that CFRPs are not only lightweight but also optimizable, allowing them to be used in challenging conditions without compromising their strength. More thorough design and extra specifications would impact both composite and aluminum-lithium struts since their weights include the end fittings and interfaces.

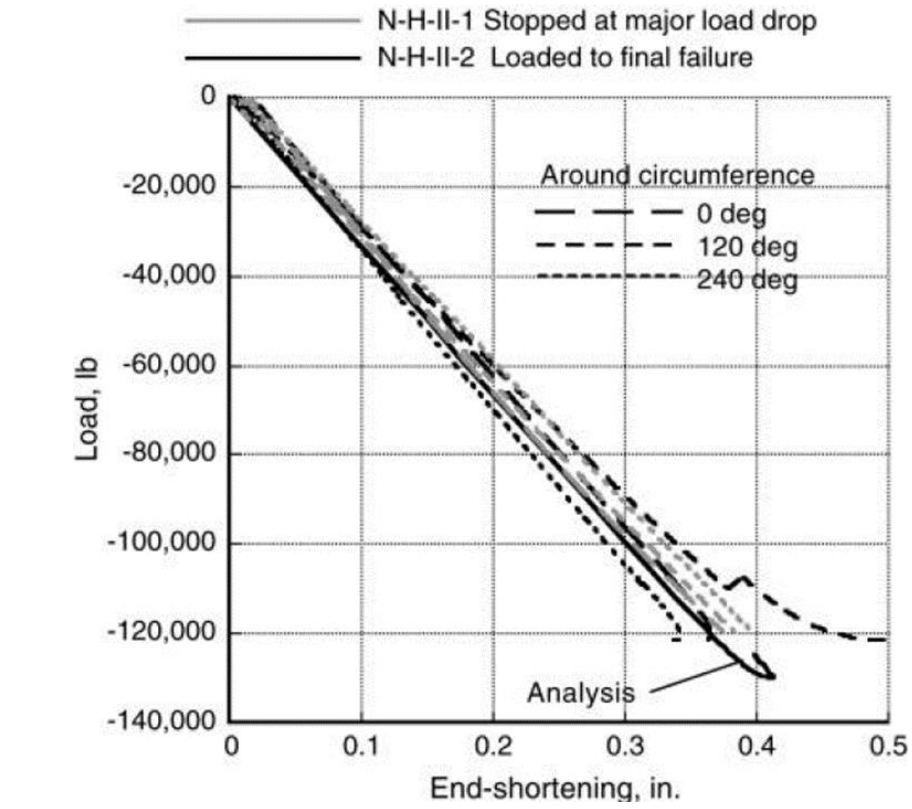

(a)

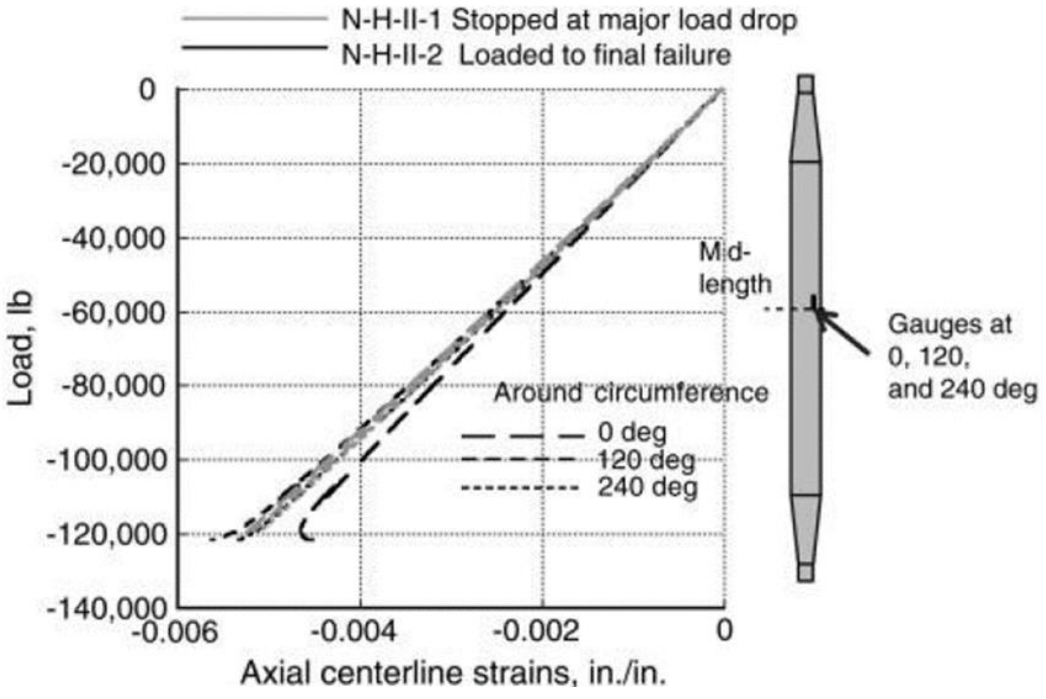

(b)

Figure 2.14 Optimal stacking sequence results regarding (a) load vs end-shortening, and (b) load vs axial strains

J. Humberto[61] reported the behavior of cylindrical carbon/epoxy filament wound tubes under axial compression. The effects of different stacking sequences on buckling behavior under two headings, thin-walled and relatively thick-walled, were compared both experimentally and with finite element models including linear, nonlinear and progressive damage model. Produced specimens and related geometric information were given in Figure 2.15.

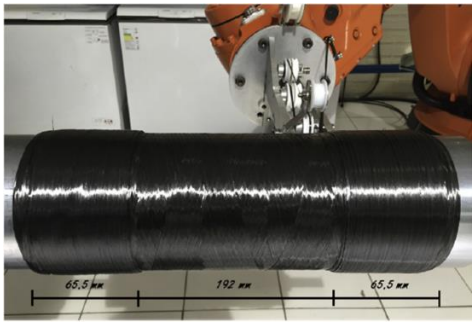

(a)

Stacking sequence	Mean thickness (mm)	Outer radius[a] (mm)	R/t ratio	Pattern number
$[\pm 55]_{FW}$	0.56	68.56	121	−4/1
$[\pm 75]_{FW}$	0.54	68.54	126	1/1
$[\pm 89.6]_{FW}$	0.46	68.46	148	1/1
$[\pm 89.6/\pm 55/\pm 75]_{FW}$	1.56	69.56	44	1/1 > −4/1 > 1/1
$[\pm 55/\pm 89.6/\pm 75]_{FW}$				−4/1 > 1/1 > 1/1
$[\pm 75/\pm 55/\pm 89.6]_{FW}$				1/1 > −4/1 > 1/1

[a] Measured in the gage section.

(b)

Figure 2.15 Properties of the produced specimen (a) winding operation, and (b) geometric parameters.(Source. Almeida et. al., 2018)

The theoretical buckling strength (bifurcation point) of a structure is produced as an output by the eigenvalue analysis used in the linear buckling FE model, which requires very little computing time and can be used in a more precise nonlinear analysis. Deflections should be small, the stress state in the finite elements should remain elastic, the internal force distribution should be constant and the resulting force effect should not be included in the differential stiffness in the linear buckling analysis. The finite element model and boundary conditions established with ABAQUS are shown in Figure 2.16.

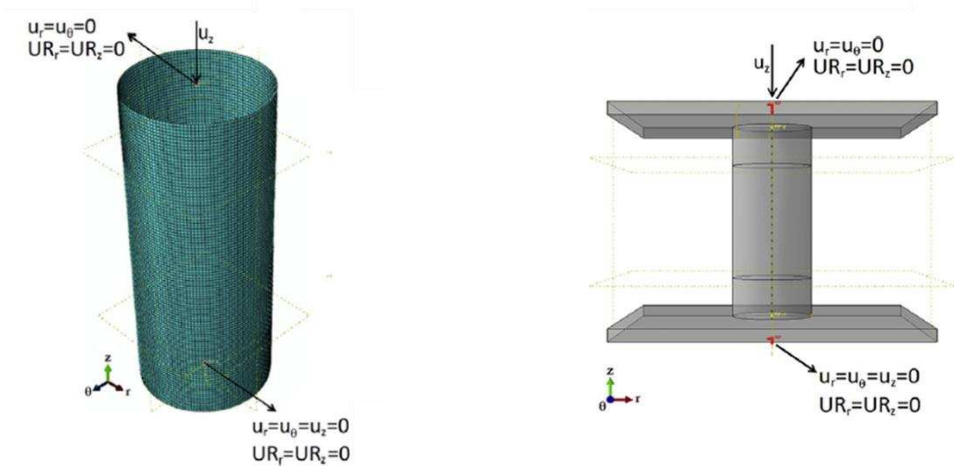

(a) (b)

Figure 2.16 (a) Eigenvalue buckling model, and (b) non-linear buckling model

Of the $[\pm\alpha]_{FW}$ laminates, the $[\pm55]_{FW}$ tube exhibited the highest buckling resistance. On the other hand, the $[\pm75/\pm55/\pm89.6]_{FW}$ tube demonstrated the most satisfactory results among the multi-angle tubes; that is, the outermost layer's hoop layer postponed the beginning of damage (See Figure 2.17).

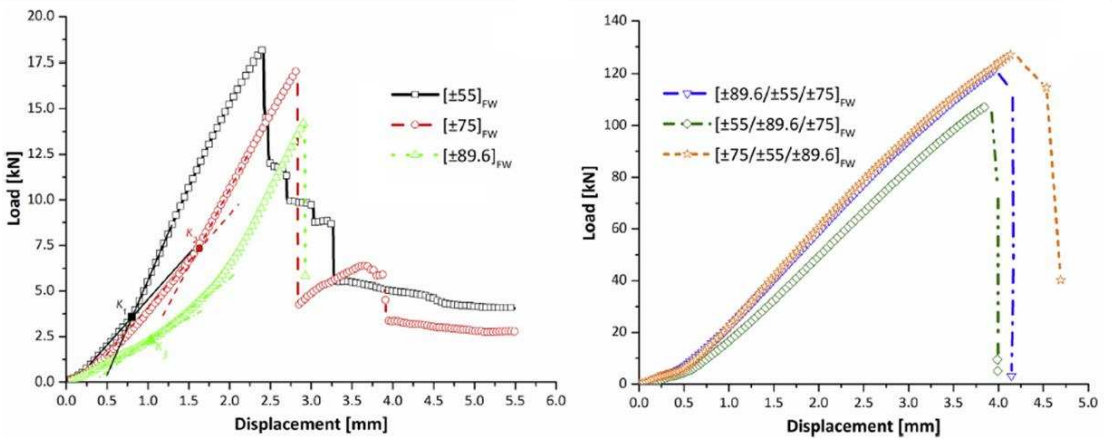

(a) (b)

Figure 2.17 Load-Displacement results of (a) $[\pm\alpha]_{FW}$ and (b) multi-layer tubes

According to the results, for $[\pm\alpha]_{FW}$ tubes, the analytical formulation and the linear FE model produced relatively reliable results. As show in Figure 2.18, Both $[\pm\alpha]_{FW}$ and multi-layered tubes showed good predictions from the nonlinear FE model. Following the peak load, the $[\pm55]_{FW}$, $[\pm75]_{FW}$, and $[\pm89.6/55/\pm75]_{FW}$ tubes demonstrated a snap-

through route with softening and load stabilization in between. The only FE model that could predict this behavior was the nonlinear buckling model, and it was linked to kinking band formations.

Overall, buckling induced thinner $[\pm\alpha]_{FW}$ tubes to fail, while material failure caused thicker tubes to fail. That was consistently found based on measurements of the load versus displacement curve form, failure mechanism (transverse compression and in-plane shear), and stress condition before final failure. Kinking bands and through-the-thickness transverse cracks were confirmed by experimental post-mortem analyses.

In 2011, a detailed study was published on the torsional stiffness, natural frequency, buckling strength, fatigue life, and failure modes of composite tubes. The study also analyzed the effect of fiber orientation angles and stacking order on these properties.[58] According to the study, when the fiber orientation angle approaches zero degrees, the natural frequency of the composite driveshaft increases. This increase is most noticeable when the carbon fibers are oriented at 0°, which can be explained by the particularly high modulus value in the axial direction. When the orientation is modified from 0° to 90°, a significant decrease of 54.3% in frequency is observed. Concerning buckling strength, the critical buckling torque is lowest for angles between 20° and 40° and reaches its maximum at a 90° orientation. In tests, tubes with fiber orientations at an angle of around 45° showed exceptional capacity to support loads and torsional stiffness. The article's finite element method (FEM) technique comprised building several models with specific boundary conditions in order accurately evaluate the composite drive shaft's several mechanical properties. For the natural frequency analysis, both ends of the drive shaft were simply supported to imitate real-world situations in which the shaft can freely rotate, with the focus on global displacements.

The critical buckling torque were determined in the buckling analysis since one end of the structure was totally confined and the other was free to rotate but constrained in the axial, radial, and hoop directions. One end was totally fixed for the torsional stiffness investigation, while the other end was subjected to a torsional load in order to examine the torque-angle of twist behavior. These characteristics also affected the failure modes, often resulting in severe failures in these configurations. The study also demonstrated how crucial the stacking sequence is to fatigue life, showing that configurations with glass fibers at 0/90° on the outer surface and carbon fibers at ±45° on the inner surface provided better buckling strength and fatigue resistance.

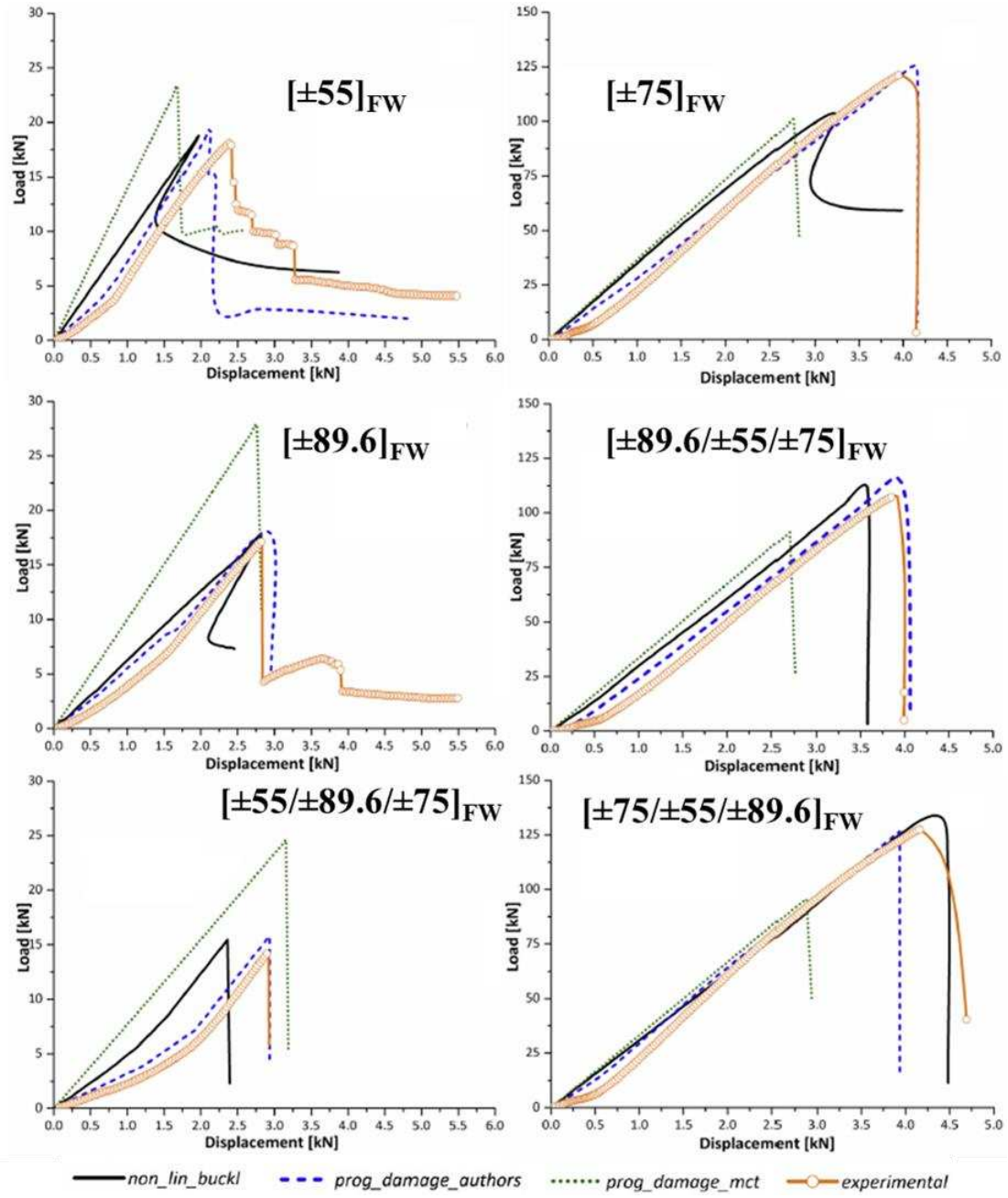

Figure 2.18 FE model and experimental results comparison of each stacking sequence

In the experiments, three different failure types were found: progressive failure for 0/90° configurations, mixed failure modes for hybrid designs, and catastrophic failure for ±45° configurations. These results highlight the promise of hybrid composites for use in automotive drive shaft applications, where they offer a careful selection of fiber orientations and stacking sequences that balance weight reduction, greater strength, and improved durability.

As reported in the literature, the thicknesses, diameters, lengths, ply angles and stacking sequences of CFRP or hybrid structures are parameterized according to the applications in which they are to be used, and optimum results are tried to be obtained according to the desired boundary conditions.

CHAPTER 3

EXPERIMNENTAL METHODOLOGIES

In this section, experimental methods regarding mechanical and physical characterization are presented and expressed sequentially.

3.1. Material

In this thesis, carbon fiber-reinforced polymer matrix composites were utilized for mechanical characterization and rod production.

The carbon fiber reinforcement used in this research consisted of 800 tex T700SC-12K filaments provided by Toray Industries, Inc. (Japan). The mechanical and physical properties of TORAY T700SC demonstrate that it is widely used in the production of lightweight and robust components for high-performance aerospace, automotive, sports goods, and as well as industrial applications including pipes and tubes.

For the epoxy matrix, a high-temperature curing system from Huntsman Inc. was selected, comprising Araldite MY740 epoxy resin (100 pbw), Aradur MY918 curing agent (85 pbw), and DY062 accelerator (0.2 pbw). The mentioned resin system was chosen due to its low viscosity, enhanced fiber wetting and long lag time at room temperature, allowing for long-term bath operation. In the following subheadings, the required physical and mechanical characterization steps are explained in detail.

3.1.1. Mechanical Characterization

In order to determine material properties and establish design limits for filament-wound composite structures, it's essential to choose an appropriate test specimen configuration and testing method. The selected specimen should represent the characteristics of the filament-wound structure as it would be processed for actual use, ensuring that the resulting data is reliable for designing or assessing products.

Figure 3.1 shows that it is possible to produce samples in panel, ring and tube form with filament winding method and mechanical characterization tests are performed in accordance with the standards.[20,23]

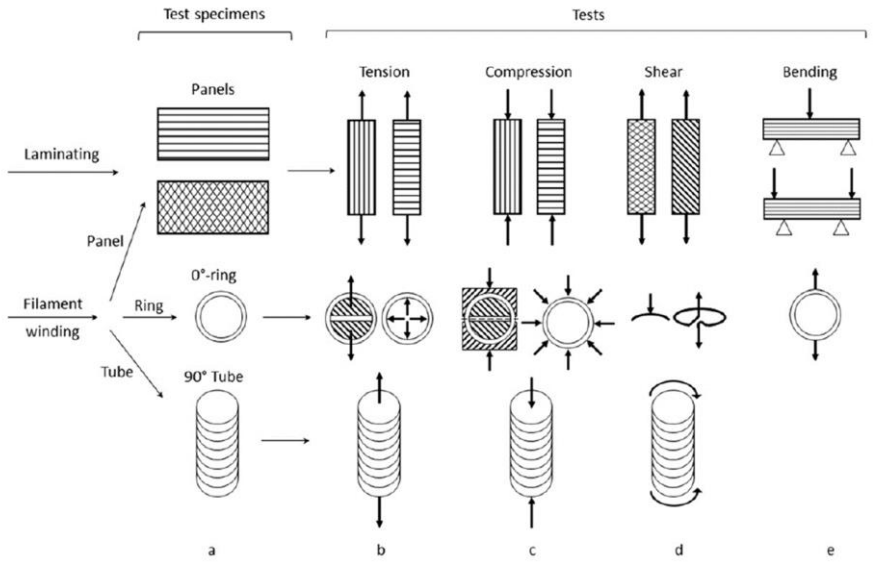

Figure 3.1 Fiber reinforced composite specimen configurations produced by filament winding method

Except for flat samples, obtaining samples in the specified standard sizes is not accessible due to the diameter, length, and curved surface of cylindrical samples. On the other hand, although filament-wound structures are generally not designed to be flat, panels can be produced by winding continuously rotating fibers around a flat plate. Thus, tensile, compression, shear, and bending test coupons that comply with the standards can be obtained, as shown in Figure 3.1.

In this thesis, flat composite samples were produced by filament winding, and the following standards and tests were used for characterization.

- Tensile Properties of Polymer Matrix Composite Materials[62]
- Compressive Properties of Polymer Matrix Composite Materials Using a Combined Loading Compression[63]
- Shear Properties of Composite Materials by the V-Notched Beam Method[64]

3.1.1.1. Composite Panel Manufacturing by FW Method

As described in 0, TORAY T700-12 K-50C carbon fiber and Hunstmann MY 740 resin system was used to fabricate panels to characterize the mechanical properties of CFRP push-pull rods. As depicted in Figure 3.2, the hoop winding G-code was generated through CADWIND, and a teflon film coated stainless steel square mandrel (360 x 360 x 10 mm^3) was used to deposit the hoop wound fibers impregnated in a resin bath. Hoop winding codes were shared in APPENDIX A.

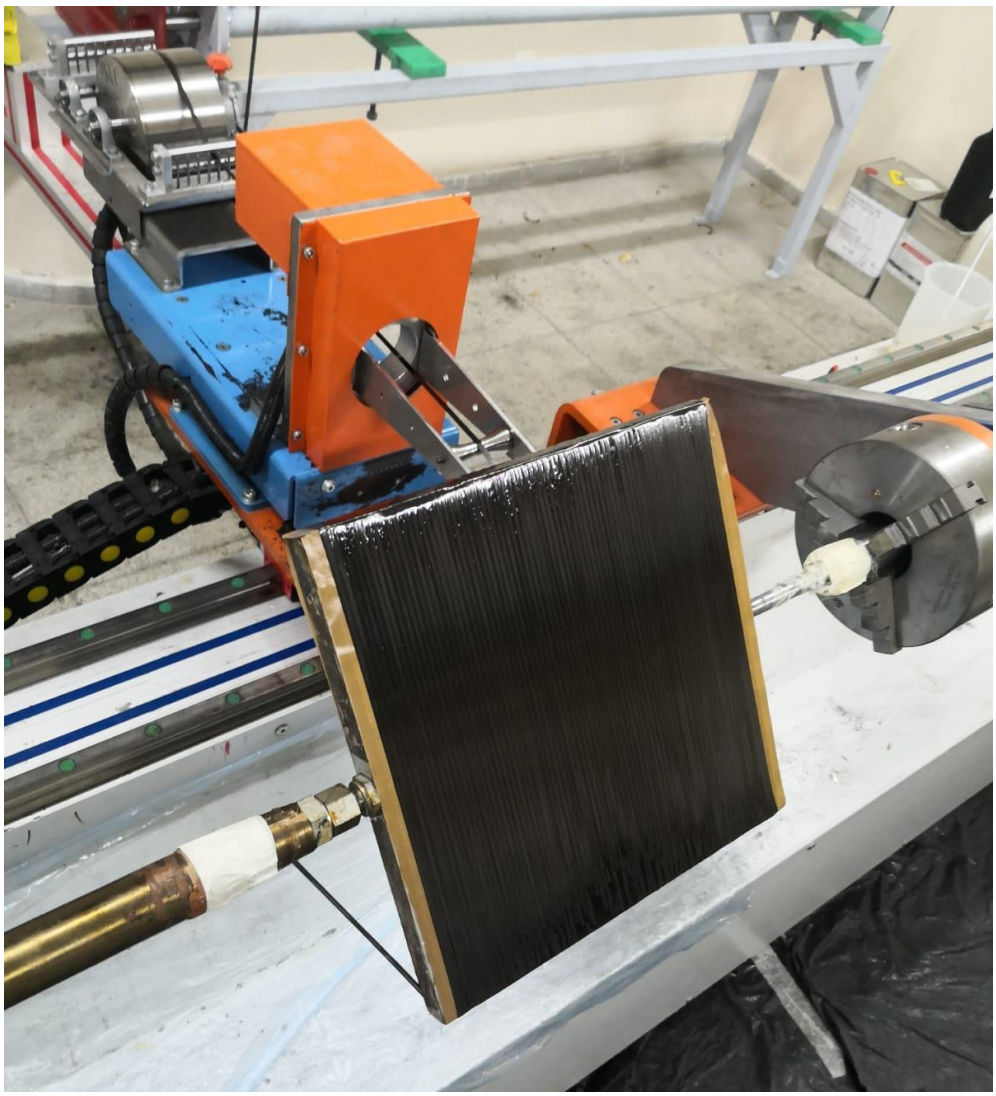

Figure 3.2 Fabrication process of hoop wound panel laminates

The ambient temperature was set to 23±2 °C to acquire desired wetting behavior of fibers. During the curing phase, the panel laminates were subjected to a rotational oven environment (see Figure 3.3), initially held at 80°C for 2 hours, followed by a subsequent treatment at 120°C for an equivalent time span, followed by cooling to ambient temperature.

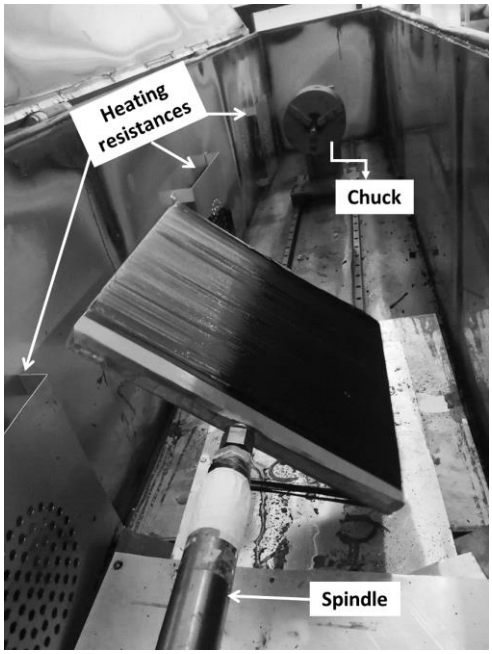

Figure 3.3 Rotary curing oven with hoop wound panels

After the curing process, the laminates were cut with a diamond saw and removed from the steel mandrel. Plates were obtained from both sides of the steel mandrel due to the winding nature and trimming operations were carried out in accordance with the standards of tensile, compression, and v-notch shear tests.

3.1.1.1.1 Standard Tensile Tests

Tensile tests were performed in compliance with ASTM 3039.[62] A Universal Instron hydraulic unit testing machine (300 kN) was employed to characterize the mechanical behavior of laminated panels. Five coupon specimens were cut in longitudinal (0°) and transverse (90°) directions to tensile strengths (X_t, Y_t), elastic moduli (E_x, E_y) and Poisson's ratio(υ_{12}). Instead of using end tabs, an emery cloth was inserted at the surface interface between the tensile specimens and the test grip. Tests were carried out at a cross-head speed of 2 mm/min, and the extensometer was placed at center of each

specimen. Extensometer markers were placed on tensile samples by considering the selected gage length. 5 specimens were tested in each orientation and tensile strength for both longitudinal and transverse directions were calculated using the following equation.

$$F^{tu} = P^{max}/A \tag{3.1}$$

F^{tu} = ultimate tensile strength, MPa

P^{max} = maximum force before failure, N

A = average cross-sectional area, mm^2

Tensile test setup can be seen in accompanying Figure 3.4.

Test results were shared in the relevant subheading, along with sample images. More information on the test procedure and calculations can be found in the related test standard.

3.1.1.1.2 Standard Compression Tests

Longitudinal and transverse compressive strength properties are also needed in the process of characterization of mechanical properties.

Standard compression tests (Figure 3.5) were conducted on specimens in the longitudinal and transverse directions according to ASTM 6641.[63] Five compression test coupons without end tabs were tested for each direction. A strain gauge was inserted into the coupons to calculate the secant compression modulus, although it was not necessary to use it during characterization, while the strengths were obtained from the load and geometrical parameters of each specimen by using Equation (3.2.

$$F^{cu} = \frac{P_f}{wh} \tag{3.2}$$

F^{cu} = laminate compressive strength, MPa

P_f = maximum load to failure, N

w = specimen gage width, mm

h = specimen gage thickness, mm

Figure 3.4 Tensile test

As shown in Figure 3.5, The fixture, which exposes the specimen to combined end -and shear- loading, is loaded by compression between flat plates in a universal testing machine. The compression test of the coupons was conducted at a cross-head speed of 1 mm/min until failure was achieved.

Test results were shared in the relevant subheading, along with sample images. More information on the test procedure and calculations can be found in the related test standard.

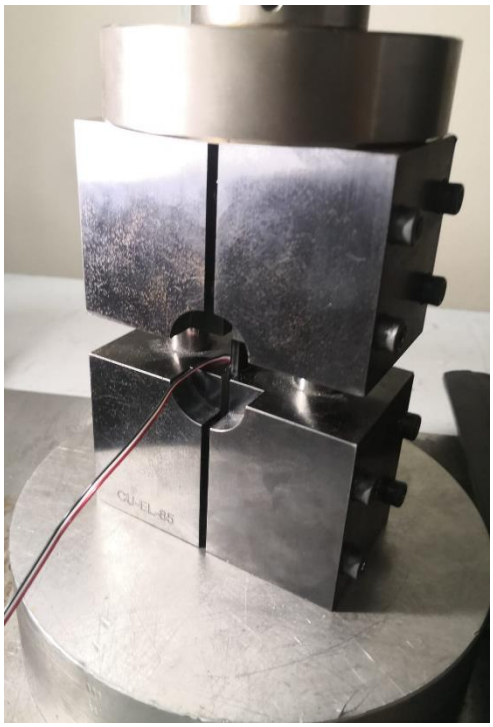

Figure 3.5 Compression test

3.1.1.1.3 V-Notched Beam Test Method

The interlaminar shear modulus (G_{12}) and ultimate strength (τ_{12}) of the carbon composite was determined by the v-notched beam method in accordance with ASTM.[64] Test equipment and v-notched beam composite coupon can be shown in Figure 3.6. The test fixture used in this experiment consists of two identical parts: one is fixed, and the other is movable. The fixed part stabilizes the composite beam, restricting both translational and rotational movement, while the movable part slides along a bearing post. As the moving part is compressed, the force is transmitted to the composite beam, thereby inducing a shear load. This configuration results in pure shear stress in the region between

the notch roots of the composite beam, effectively creating a zone with zero bending moment.

Following the testing standard, the crosshead velocity for this test was set to 2 mm/min. Additionally, two strain gauges were installed on the composite beam in a ±45° orientation relative to the axis between the notch roots. These strain gauges are used to measure shear strain, which allows for the calculation of the shear modulus. This setup provides a reliable method for studying the shear characteristics of composite materials in a controlled manner.

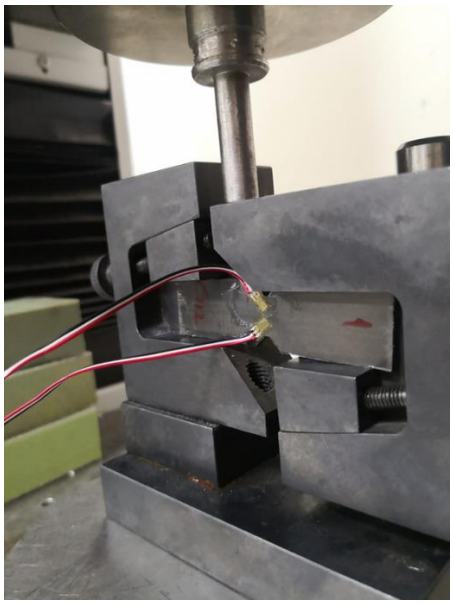

Figure 3.6 V-notched beam test setup

Shear stress τ_{12} and shear strain γ_{12} were calculated using the following equations. Shear moduli G_{12} were determined from these shear stress strain curves generated.

$$\tau = \frac{P}{A} \quad , \quad A = bw \tag{3.3}$$

τ = shear strength, MPa

P = maximum load, N

A = cross-sectional area, mm^2

w =coupon width (between notch roots), mm

h =coupon thickness, mm

$$\gamma = |\varepsilon_{+45}| + |\varepsilon_{-45}| \quad (3.4)$$

γ = engineering shear strain, mm/mm

ε_{+45} = + 45° normal strain, mm/mm

ε_{-45} = −45° normal strain, mm/mm

Test results were shared in the relevant subheading, along with sample images. More information on the test procedure and calculations can be found in the related test standard.

3.2. Thermomechanical Properties of Produced Composites

Dynamic mechanical analysis (DMA) was conducted using TA™ Q800 equipment to examine the thermomechanical properties of composite materials. The test employed a three-point bending mode with a dynamic force applied at a frequency of 1 Hz. The temperature range was programmed to increase at a rate of 3ºC per minute, spanning from 20 to 200ºC. The dimensions of the specimens were 3 mm by 13 mm by 60 mm. A dual cantilever mode was utilized for DMA testing, where the specimen is clamped at both ends and bent at the midpoint. The glass transition temperature (T_g) of the carbon/epoxy specimen was identified using the tangent delta (tanδ) peak. Figure 3.7 illustrates the DMA test apparatus.

Figure 3.7 TA™ Q800 DMA test equipment.

3.3. Rod Manufacturing by Filament Winding Method

Prior to the optimization process, symmetrical and balanced reference push-pull rods with $[\pm 30]_6$ and $[\pm 45]_6$ winding angles were produced to be used in comparison.

First of all, the filament winding process is simulated through CADWIND[65] software. Thus, potential operational difficulties can be seen by simulating the winding operations. Further, the production parameters such as diameter, number of roving, length, winding angle, pattern number, degree of coverage, fiber width, resin density, friction factor etc., of composite pressure vessels, rod structures, and plates to be produced can be controlled with CADWIND.

In order to simulate filament winding, the mandrel must first be designed. The mandrel used in this study is made of stainless steel and has a diameter of 20 mm and a length of 1.5 meters.

In addition to other production parameters, the degree of coverage and pattern number are significant parameters for comparison. If a relatively thin structure is produced, the winding pattern may affect the buckling behavior under loading. On the other hand, it is essential to choose the same value of the degree of coverage for each rod to ensure uniform thickness and number of layers.

Taking possible errors into consideration, the degree of coverage value was kept between 110 and 113%. The control screen for these parameters is shared in Figure 3.8.

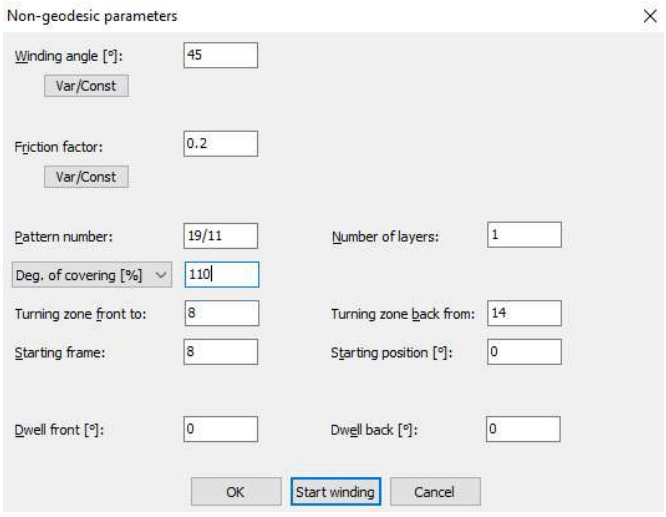

Figure 3.8 Control screen of related winding parameters

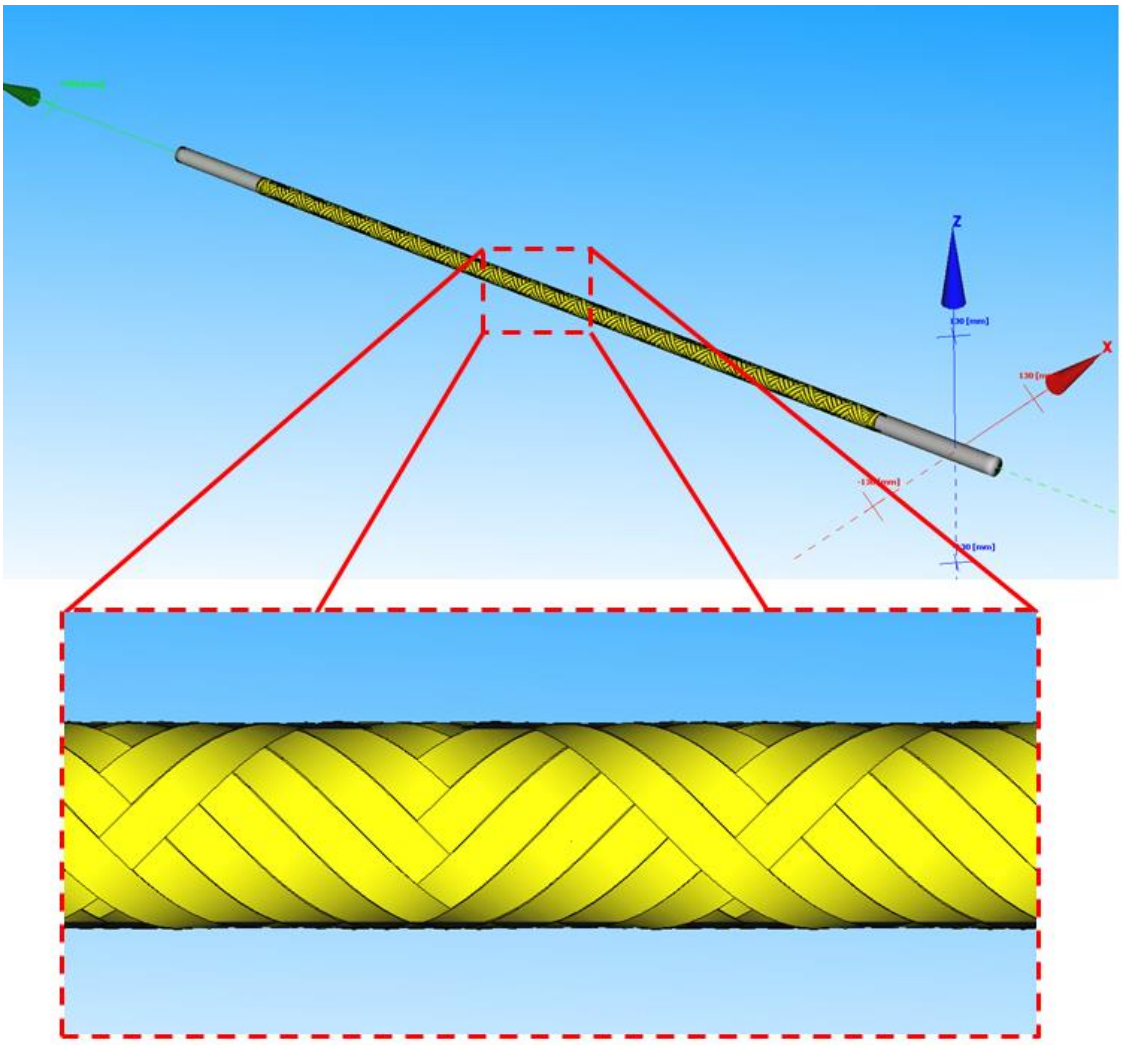

Figure 3.9 Filament winding simulation of $[\pm 45]_6$ reference rod by means of CADWIND

Upon simulation of the production process, the delineated distances from the tip to the end points on the mandrel, in conjunction with the winding pattern, are visualized as depicted in Figure 3.9. Following a satisfactory simulation outcome, G-code is generated and transferred to the filament winding machine.

The rods were produced with a CNC-controlled 4-axis filament winding machine manufactured by Fibermak Composites Inc. within IZTECH. The general view of the machine was displayed in Figure 3.10.

Figure 3.10 General view of 4-axis filament winding machine

The filament winding machine rotates at a maximum of 150 rpm and is capable of winding sizes of 2000 mm in length and 250 mm in diameter. The production image of the reference sample is shared in Figure 3.11 below.

Figure 3.11 Production of $[\pm 45]_6$ lay-up composite rod

Further, it is used together with a tensioning machine and resin bath during production. The tensioning machine applies between 10 and 40 N of tension on dry fibers and dynamically transmits the desired load during production through servo-controls. 4-row tensioning machine is shared in Figure 3.12.

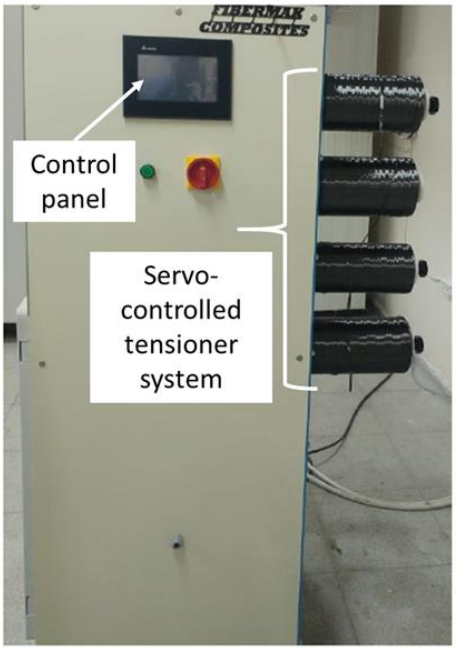

Figure 3.12 Tensioner system

Another crucial component of filament winding equipment is the resin bath. Dry fibers are directed through the resin bath, where they are impregnated with epoxy resin. The control of epoxy resin quantity is facilitated by the resin bath, a vital factor in determining the fiber mass fraction in composite materials. Figure 3.13 provides a visual representation of the resin bath utilized for filament winding applications.

Figure 3.13 Resin bath

The final stage of the filament winding process involves the curing of composite parts within an oven. Subsequent to the winding process, composites were subjected to a rotational oven environment, initially held at 80°C for 2 hours, followed by a post-curing treatment at 120°C for an equivalent time span, followed by cooling to ambient temperature. The rotational motion employed during the curing process ensures uniformity across all regions of the composite. Utilized rotating oven can be seen in Figure 3.14.

Figure 3.14 Rotating curing oven

Once the curing process is complete, the rod needs to be removed from the mandrel. Even though mold-release chemical agents are used, the windings in the tip and end sections relatively fix the composite to the mandrel. The hydraulic extraction machine was designed within the scope of this thesis to perform the separation process. Figure 3.15 displays the extraction machine in the lab's inventory. An example of the g-code generated for rod production is available in APPENDIX B.

Figure 3.15 Extraction machine

3.3.1. Buckling Test

Using a hydraulic MTS universal testing machine model with a 3000 kN load cell together with platens, the developed rods were subjected to axial compression. The displacement-controlled tests were conducted at a rate of 1 mm/min. In order to reduce stress concentrations near the end closures and the tip-end problem, CFRP rods were fixed with housings made of stainless-steel material to eliminate the possibility of local failures during the tests. The biaxial gauge was placed in the middle of the CFRP rod (400 mm) to monitor both axial and radial strains during the Mode 1 buckling phenomenon. Three samples, 30, 45, and the optimized sample, from each sample layup orientation were produced in order to conduct buckling test. The test setup including the equipment used can be seen in Figure 3.16.

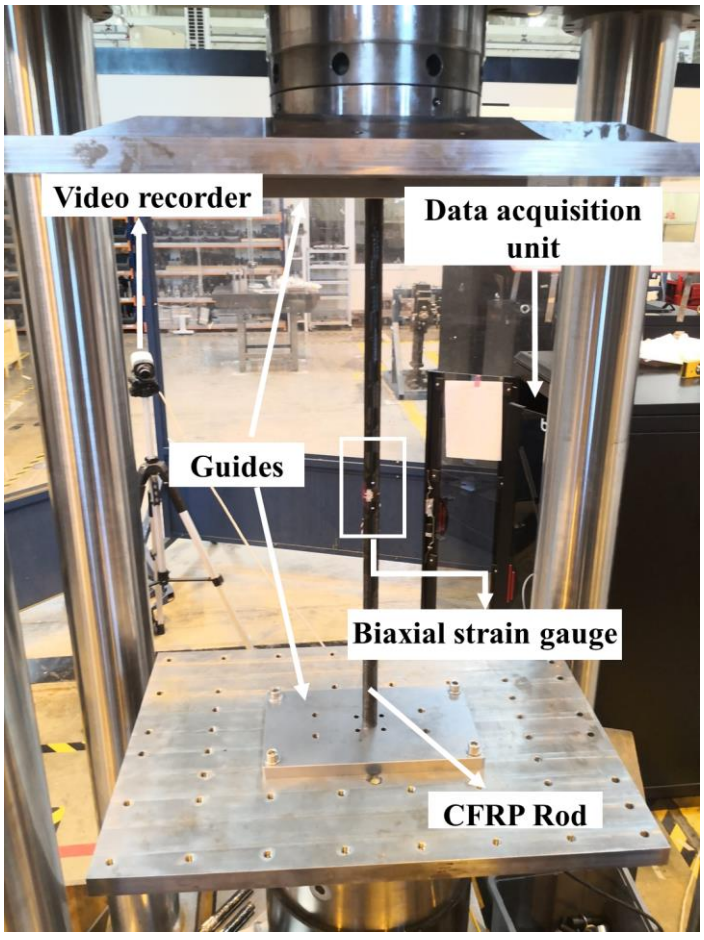

Figure 3.16 Buckling test setup with video recorder and strain gauge attachment

3.3.2. Physical Characterization

In this chapter, the physical characterization processes, including acid digestion and microstructural investigation (optical and scanning electron microscopies) carried out within the scope of the thesis, are explained in detail.

3.3.2.1. Fiber Volume Fraction Calculations

Fiber volume fraction of the composite were investigated in accordance with ASTM Test Methods. The volume fraction of carbon CFRP rods was determined by the acid digestion method according to ASTM D3171-15 (PROCEDURE-B).[66] Three samples ranging from 2 to 2.5 grams for each group were cut with a diamond saw for fiber volume fraction calculation. Then, according to Procedure B, each sample was placed in a sulfuric acid bath in a crucible on a hot plate. They were heated by a hot plate heater for at least 2 hours. After adding 35 ml hydrogen peroxide, as the fibers float to the surface of the solution, the solution itself takes on a clear appearance or experiences a significant reduction in color intensity. After the matrix was fully digested, all samples were washed with distilled water to remove solution, and then dried in an oven. The summary of the process can be seen in Figure 3.17.

(a)

Figure 3.17 Acid digestion of CFRP, (a) Digestion samples, (b) During the digestion ,and (c) dried and weight fibers

(cont. on next page)

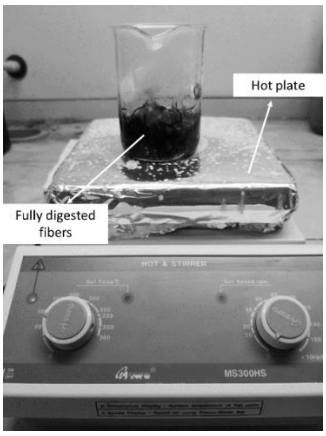

(b)

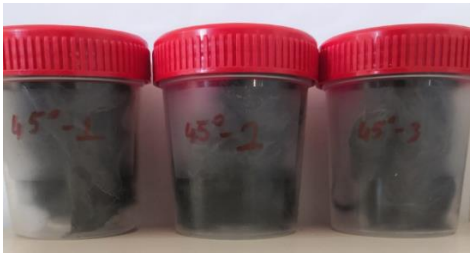

(c)

Figure 3.17 **(cont.)**

After weighing and recording, all samples were subjected to calculations using the following formulas to determine the weight and volume percentages of carbon fiber reinforcement material.

$$W_r(\%) = \frac{m_{initial}}{m_{fiber}} 100 \tag{3.5}$$

$m_{initial}$ = initial mass of the sample

m_{fiber} = final mass of the sample after digestion

$$V_r\ (\%) = W_r(\%) \frac{\rho_c}{\rho_r} \tag{3.6}$$

ρ_r = density of the reinforcement, (1.7 g/cm^3)

ρ_c = density of the specimen, g/cm^3

3.3.2.2. Optical Microscopy

Optical microscopy, as it is known, employs visible light to investigate a specimen, allowing magnification and visualization of its details. Within the scope of this study, an optical microscope was used to detect possible voids and resin-rich zones in the microstructure of the produced rods. During the sample preparation process, a sample in ring geometry is first cut from the composite rod using a diamond saw. Grinding and polishing steps are carried out to examine the microstructure. Finally, the sample surface, cleaned from the polishing solution, is dried in an oven at 50 degrees for 2 hours and made ready for examination.

LEICA DM 2500[67] optical microscope(see Figure 3.18) was used for microstructural examination.

Figure 3.18 Optical microscope - LEICA DM 2500

3.3.2.3. Scanning Electron Microscopy

Scanning electron microscopy (SEM) uses a focused electron beam to create high-resolution images of a sample's surface. Electrons emitted from a filament are accelerated through a column, focused onto the sample, and generate signals upon interaction. These signals reveal the sample's topography, composition, and crystal structure. In this study, the samples used in the optical microscope were also used in SEM analyses. It is aimed to examine the fiber orientations adjusted during winding and the microstructural defects detected by the optical microscope through SEM.

Microstructure examinations were carried out using the Quanta 250 SEM device within IZTECH MAM. The image of the device used was shared on Figure 3.19.

Figure 3.19 FEI Quanta 250 SEM

CHAPTER 4

MECHANICS OF COMPOSTE MATERIALS

In the context of engineering structures exposed to mechanical and thermal loads, the field of mechanics of materials deals with stresses, strains, and deformations. The mechanics of traditional materials, such as steel and aluminum, are based on the assumption that they are homogeneous and isotropic. This means that the properties of these materials are independent of orientation and location. In metallic materials, grain orientation is typically random, unless heavily cold-worked, which supports the idea of isotropy. On the other hand, fiber-reinforced composites are nonisotropic (orthotropic) and microscopically inhomogeneous. This means that the mechanics of fiber-reinforced composites are much more complex than those of traditional materials.[18]

Two levels of study are conducted on the mechanics of fiber-reinforced composite materials:

- Micromechanics which studies the microscopic interactions between the component materials. Micromechanics formulas are typically the basis for equations defining a lamina's elastic and thermal properties. Determining the failure mechanisms of a fiber-reinforced composite material also requires an understanding of the interactions between different constituents.
- Macromechanics, in which the response of a fiber-reinforced composite material to mechanical and thermal loads is examined on a macroscopic scale. The material is assumed to be homogeneous. Equations of orthotropic elasticity are used to calculate stresses, strains, and deflections.

In this study, the calculation of the desired properties (Buckling, natural frequency, torsional stiffness) was calculated using classical lamination theory. The details of the CLT are detailed in the following section.

4.1. Classical Lamination Theory

Lamination theory is utilized to determine the overall elastic constants, stresses, strains and curvature in each ply of a thin laminate under loading.

It is based on several main assumptions that form the basis of classical lamination theory (CLT).

- Perfectly Bonding / Laminae are perfectly bonded, there is no slipping between the lamina interfaces.
- Plane Stress Assumption / The plate's thickness is substantially smaller than the in-plane direction.
- Mid-Plane Strains and Curvatures / line straight and perpendicular to the middle surface remains straight and perpendicular to the middle surface during deformation
- Each lamina is homogeneous and act in a linearly manner.
- Stress normal to the plate is negligible.

The cartesian coordinate system x, y, and z define the layered material's global coordinates (See Figure 4.1 (a)). A layer-wise principal material coordinate system is designated by 1 and 2 with fiber direction orientated at angle θ to the x axis. Further, Figure 4.1 (b) and (c) illustrates the in-plane, bending, and twisting loads that a laminate can withstand.

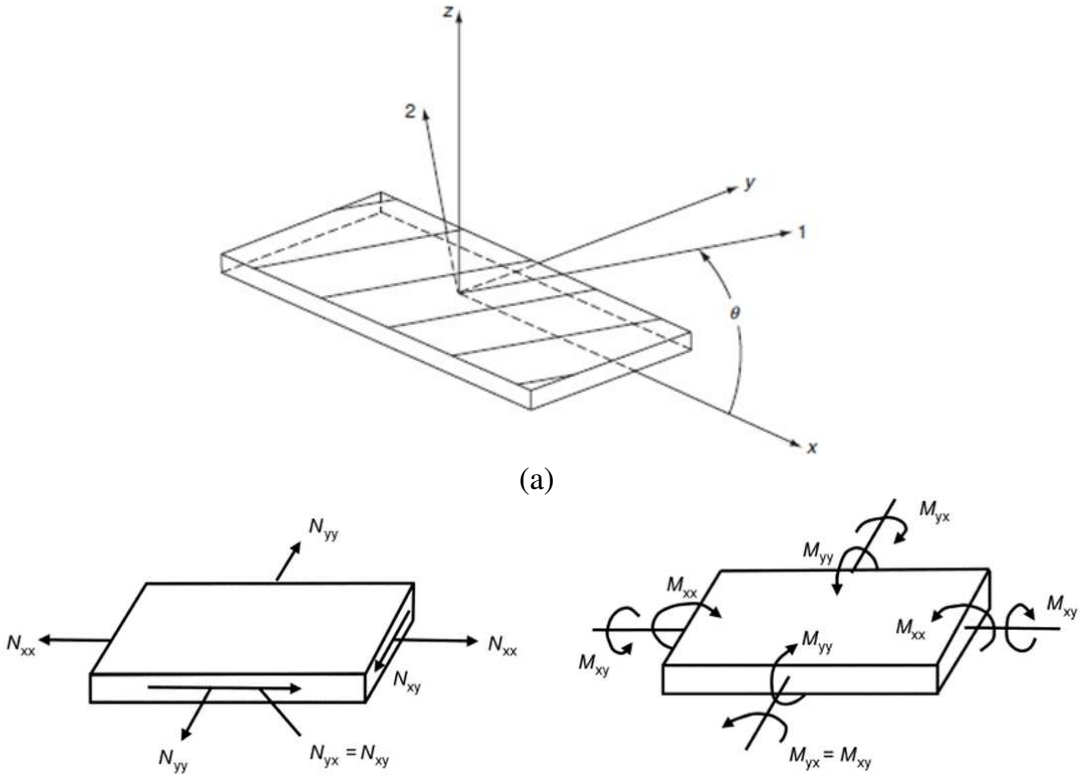

Figure 4.1 (a) Description of principal material and loading axes, (b)force resultants, and (c) moment resultants

where:

N_{xx}, N_{yy} = normal force resultants in the x- and y- directions per unit width

N_{xy} = shear force resultant per unit width

M_{xx}, M_{yy} = bending moment resultant in the yz and xz planes per unit width

M_{xy} = twisting moment resultant per unit width

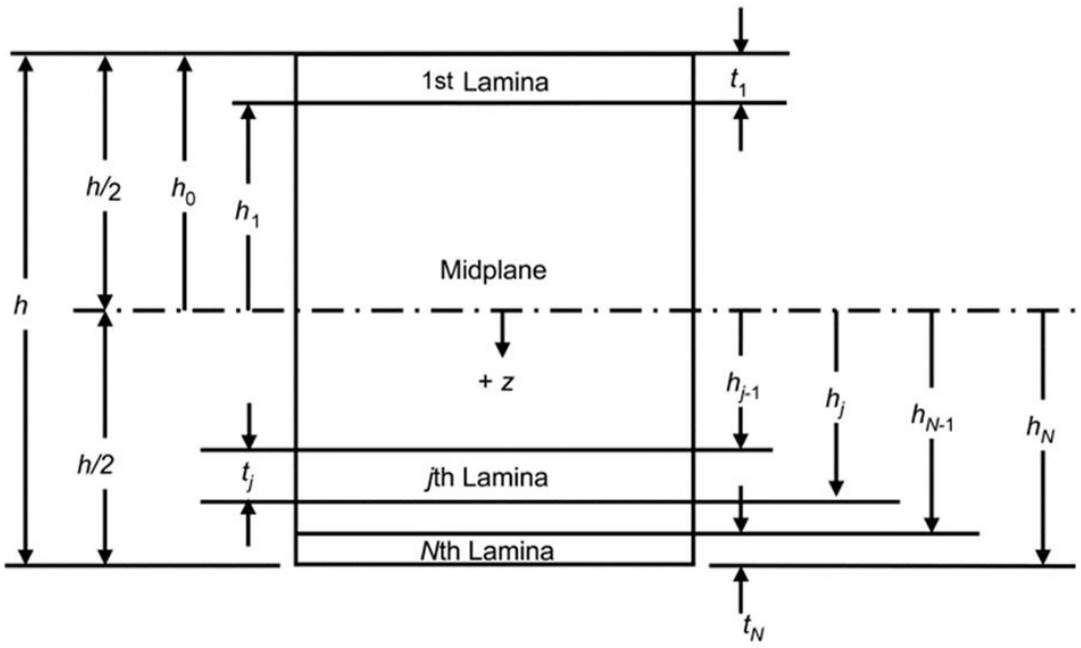

Figure 4.2 Laminate stacking sequence notation

Based on the given assumptions, it is possible to show that the in-plane displacements, thermal and hygral elongations are ignored, consist of a mid-surface displacement (superscript 0) and a linear displacement through the thickness, as presented below.

$$\varepsilon_{xx} = \varepsilon_{xx}^{0} + zk_{xx} \tag{4.1}$$

$$\varepsilon_{yy} = \varepsilon_{yy}^{0} + zk_{yy} \tag{4.2}$$

$$\gamma_{zz} = \varepsilon_{zz}^{0} + zk_{zz} \tag{4.3}$$

For a general orthotropic lamina, the stress-strain relations can be expressed as:

$$\begin{bmatrix}\sigma_{xx}\\ \sigma_{yy}\\ \tau_{xy}\end{bmatrix} = \begin{bmatrix}\bar{Q}_{11} & \bar{Q}_{12} & \bar{Q}_{16}\\ \bar{Q}_{12} & \bar{Q}_{22} & \bar{Q}_{26}\\ \bar{Q}_{16} & \bar{Q}_{26} & \bar{Q}_{66}\end{bmatrix}\begin{bmatrix}\varepsilon_{xx}\\ \varepsilon_{yy}\\ \gamma_{xy}\end{bmatrix} = [\bar{Q}]\begin{bmatrix}\sigma_{xx}\\ \sigma_{yy}\\ \tau_{xy}\end{bmatrix} \tag{4.4}$$

where the stiffness matrix for the lamina is denoted by $[\bar{Q}]$. Different elements within the $[\bar{Q}]$ matrix are represented in terms of each [Q] as follows:

$$\bar{Q}_{11} = Q_{11}c^4 + Q_{22}s^4 + 2(Q_{12} + 2Q_{66})s^2c^2 \tag{4.5}$$

$$\bar{Q}_{12} = (Q_{11} + Q_{22} - 4Q_{66})s^2c^2 + Q_{12}(c^4 + s^4) \tag{4.6}$$

$$\bar{Q}_{22} = Q_{11}s^4 + Q_{22}c^4 + 2(Q_{12} + 2Q_{66})s^2c^2 \tag{4.7}$$

$$\bar{Q}_{16} = (Q_{11} - Q_{12} - 2Q_{66})sc^3 - (Q_{22} - Q_{12} - 2Q_{66})cs^3 \tag{4.8}$$

$$\bar{Q}_{26} = (Q_{11} - Q_{12} - 2Q_{66})cs^3 - (Q_{22} - Q_{12} - 2Q_{66})sc^3 \tag{4.9}$$

$$\bar{Q}_{66} = (Q_{11} + Q_{22} - 2Q_{12} - 2Q_{66})c^2s^2 + (c^4 + s^4) \tag{4.10}$$

where

$$Q_{11} = \frac{E_1}{1-\upsilon_{21}\upsilon_{12}} \tag{4.11}$$

$$Q_{12} = \frac{\upsilon_{12}E_2}{1-\upsilon_{21}\upsilon_{12}} \tag{4.12}$$

$$Q_{22} = \frac{E_2}{1-\upsilon_{21}\upsilon_{12}} \tag{4.13}$$

$$Q_{66} = G_{12} \tag{4.14}$$

The resultant forces per unit length in the x-y plane through the laminate thickness are obtained by integrating the global stresses in each lamina as:

$$\begin{bmatrix} N_{xx} \\ N_{yy} \\ N_{xy} \end{bmatrix} = \int_{-\frac{h}{2}}^{\frac{h}{2}} \begin{bmatrix} \sigma_{xx} \\ \sigma_{yy} \\ \tau_{xy} \end{bmatrix} dz \tag{4.15}$$

in which h/2 is the laminate's half-thickness as described in Figure 4.2.

Likewise, the moments per unit length in the x-y plane through the laminate thickness can be obtained by integrating the global stresses in each lamina.

$$\begin{bmatrix} M_{xx} \\ N_{yy} \\ M_{xy} \end{bmatrix} = \int_{-\frac{h}{2}}^{\frac{h}{2}} \begin{bmatrix} \sigma_{xx} \\ \sigma_{yy} \\ \tau_{xy} \end{bmatrix} z dz \tag{4.16}$$

Force resultants equation can be written as follows:

$$\begin{bmatrix} N_{xx} \\ N_{yy} \\ N_{xy} \end{bmatrix} = [A] \begin{bmatrix} \overset{\circ}{\varepsilon_{xx}} \\ \overset{\circ}{\varepsilon_{yy}} \\ \overset{\circ}{\gamma_{xy}} \end{bmatrix} + [B] \begin{bmatrix} k_{xx} \\ k_{yy} \\ k_{xy} \end{bmatrix} \tag{4.17}$$

The equation for moment resultants can be expressed as follows:

$$\begin{bmatrix} M_{xx} \\ M_{yy} \\ M_{xy} \end{bmatrix} = [B] \begin{bmatrix} \overset{\circ}{\varepsilon_{xx}} \\ \overset{\circ}{\varepsilon_{yy}} \\ \overset{\circ}{\gamma_{xy}} \end{bmatrix} + [D] \begin{bmatrix} k_{xx} \\ k_{yy} \\ k_{xy} \end{bmatrix} \tag{4.18}$$

For the laminate, the extensional stiffness matrix [A] is:

$$[A] = \begin{bmatrix} A_{11} & A_{12} & A_{16} \\ A_{12} & A_{22} & A_{26} \\ A_{16} & A_{26} & A_{66} \end{bmatrix} N/m \tag{4.19}$$

Coupling stiffness matrix [B] is:

$$[B] = \begin{bmatrix} B_{11} & B_{12} & B_{16} \\ B_{12} & B_{22} & B_{26} \\ B_{16} & B_{26} & B_{66} \end{bmatrix} \text{N} \tag{4.20}$$

Lastly, bending stiffness matrix [D] is:

$$[D] = \begin{bmatrix} D_{11} & D_{12} & D_{16} \\ D_{12} & D_{22} & D_{26} \\ D_{16} & D_{26} & D_{66} \end{bmatrix} \text{N m} \tag{4.21}$$

Overall, the outcomes from (4.15) to (4.21) can be concisely expressed as follows:

$$\begin{bmatrix} N_x \\ N_y \\ N_{xy} \\ M_x \\ M_y \\ M_{xy} \end{bmatrix} = \begin{bmatrix} A_{11} & A_{12} & A_{16} & B_{11} & B_{12} & B_{16} \\ A_{12} & A_{22} & A_{26} & B_{12} & B_{22} & B_{26} \\ A_{16} & A_{26} & A_{66} & B_{16} & B_{26} & B_{66} \\ B_{11} & B_{12} & B_{16} & D_{11} & D_{12} & D_{16} \\ B_{12} & B_{22} & B_{26} & D_{12} & D_{22} & D_{26} \\ B_{16} & B_{26} & B_{66} & D_{16} & D_{26} & D_{66} \end{bmatrix} \begin{bmatrix} \varepsilon_x \\ \varepsilon_y \\ \varepsilon_{xy} \\ \kappa_x \\ \kappa_y \\ \kappa_{xy} \end{bmatrix} \tag{4.22}$$

It is observed that when A_{16} and A_{26} are nonzero, stretching-shearing coupling takes place. When the B_{16} and B_{26} terms are non-zero, there is both twisting-stretching and bending-shearing coupling; bending-twisting coupling is caused by the non-zero values of the D_{16} and D_{26} terms. Proper stacking sequences typically prevent the $(\ )_{16}$ and $(\ )_{26}$ terms, although in some structural applications—like aeroelastic tailoring—these effects might be advantageous.[68–71]

The most affected matrix by stacking order is the [D] matrix. For any plies with a 0° or 90° orientation, the terms D_{16} and D_{26} are zero. If there is an identical ply oriented at –θ at the same distance below the midplane for every ply oriented at +θ at a particular distance above the midplane, then the terms D_{16} and D_{26} will also be zero.

At the design stage of CFRP rods, it was decided to calculate and use the smear properties with the CLT, even though the radius/thickness ratio was around 7. The typical approach for assessing cross-sectional stiffness involves utilizing the CLT with smear property, whereby the moduli of the curved shell were computed under the assumption that it behaves as a flat laminate. This data is then integrated with the shell's geometry to determine the comprehensive stiffness characteristics of the structure. The modified stiffness matrix proposed by Fan et al.[72] which includes added curvature terms, closely approximates finite element results; however, the solution with the smeared property also provides consistent results with less than a 5% deviation. In another study[73], smear property, finite element method and unique analytical approaches were compared to predict the behavior of 1 meter long elliptical cross-section composite tubes made out of graphite/epoxy with balanced and symmetrical stacking sequence $[\pm 45_2/0_2/\pm 45]_s$ under

bending loads. The diameter range from 7.5 mm to 66 mm was investigated and the results of the comparison are presented in the Table 4.1.

Table 4.1 Evaluation of bending stiffness of composite tubes

Major Radius, (in)	FEM Result (lb-in$^{4)}$	Smear Property Approach, (lb-in$^{4)}$	Present Method (lb-in$^{4)}$
2.6	1.9677E+7	2.0964E+7(6.54%)	1.9726E+7(0.25%)
2.2	1.2011E+7	1.2702E+7(5.75%)	1.1951E+7(-0.50%)
1.8	6.6285E+6	6.9592E+6(4.99%)	6.5465E+6(-1.24%)
1.4	3.1419E+6	3.2761E+6(4.27%)	3.0808E+6(-1.94%)
1.0	1.1522E+6	1.1955E+6(3.76%)	1.1233E+6(-2.51%)
0.8	5.9139E+5	6.1300E+5(3.65%)	5.7548E+5(-2.69%)
0.6	2.5000E+5	2.5944E+5(3.78%)	2.4309E+5(-2.76%)
0.5	1.4486E+5	1.5063E+5(3.98%)	1.4086E+5(-2.76%)
0.4	7.3559E+4	7.7578E+4(5.47%)	7.2290E+4(-1.72%)
0.3	3.1249E+4	3.3146E+4(6.07%)	3.0652E+4(-1.91%)

When the results were analyzed, it was found that there was a maximum difference of 6.54% between the smear property approach and the finite element model, although a deviation of 3% was detected between their original approach and the finite element model.

Considering the results reported in the literature, it is found that the smear property approach converges to the results of the finite element method with a deviation of less than 7%. Despite the fact that the radius/thickness ratio was roughly 7, it was chosen to compute and apply the smear qualities with the CLT. Thus, equations utilized in optimization procedures targeting improving buckling damage have been formulated employing the smeared property approach.

The reduced stiffness matrix $[\bar{Q}]$ is calculated by determining the E (Elastic modulus), G (Shear modulus) and Poisson's ratio (υ) values obtained through mechanical characterization (see Table 7.1). Thus, equivalent stiffness matrix in the axial direction (E_x) and equivalent shear modulus (G_{xy}) are calculated as depicted in Equation 4.23 and 4.24.

$$E_x = 1/t \left[A_{11} - \frac{A_{12}^2}{A_{22}}\right] \tag{4.23}$$

$$G_{xy} = A_{66}/t \tag{4.24}$$

4.1.1. Axial Buckling

Buckling occurs when stability is lost due to geometric factors rather than material failure. It's crucial to control resulting deformations to prevent material failure and collapse. Structures typically have a linear elastic operating range, where they return to their original form when the load is removed. However, if this range is exceeded, as seen with matrix cracking in composites, permanent deformations occur. Understanding and managing buckling is key to ensuring the long-term safety and stability of structures. A representative graph of the buckling test is shown in Figure 4.3.

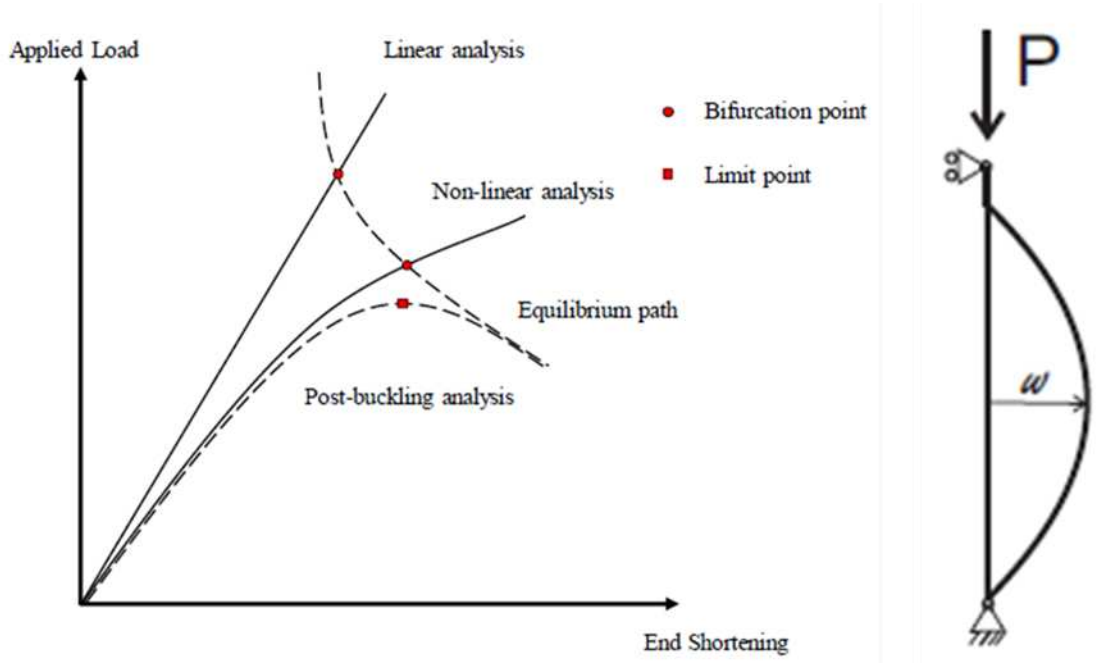

Figure 4.3 Equilibrium paths for the perfect column.

As demonstrated on the right-hand side of Figure 4.3, a slender column subjected to axial compression buckles with a lateral deflection similar to the bending of a beam, known as Euler buckling. When a column buckles due to lateral deflection, the shape of the section remains unchanged. The critical load of a long column, also known as the buckling load, depends on the bending stiffness (EI) of the section, the length of the column and the type of support at its ends.[10] Coefficients(μ) regarding boundary conditions can be seen in Table 4.2.

Table 4.2 Boundary conditions for long column buckling.(Source: Smith,1998)

End-Restraint	Theory	Steel	Wood
Pinned-pinned	1.0	1.0	1.0
Clamped-Clamped	0.5	0.65	0.65
Pinned-clamped	0.7	0.8	0.8
Clamped-free	2.0	2.1	2.4

Overall, relatively long and thick rods may exhibit column buckling behavior under axial loading. The critical load can be calculated using the modified Euler buckling formula as:

$$P_{cr} = n^2 \frac{\pi^2 E_x I}{\mu L^2} \tag{4.25}$$

Where P_{cr} is the critical buckling load, N; n is buckling mode shape; E_x is the smeared axial stiffness, MPa (see 4.23); I is the moment of inertia, mm^4; μ is a constant for specifying the boundary conditions of the rod ends; L is the length of rod, mm. Thus, the critical buckling load of rods can be tailored by optimizing E_x using the ply angles and stacking sequence parameters.

Since natural vibration or buckling is an eigenvalue problem, it only occurs at specific values. Therefore, the natural frequencies and the buckling load represent the eigenvalues, while the vibrational mode and the buckling mode correspond to the eigenfunctions. When calculating natural frequency, multiple n values are significant, but in buckling, only the n value that produces the lowest P_{cr} matters, which is n=1. This is because the structure fails entirely and experiences permanent deformation once the critical buckling load is surpassed.[69]

When examining the given equations, it becomes evident that the boundary conditions and material properties are idealized. Additionally, to simplify the calculations, the transverse shear deformation (TSD) effect was disregarded. For precise analysis of composite material shells, it's important to consider transverse shear deformation due to the fiber-dependent property of the modulus of elasticity in the fiber direction. On the other hand, the transverse shear modulus is dominated by the matrix. However, during initial design stages, it's often acceptable to disregard transverse shear deformation, which simplifies the governing equations.

Experimental results (naturally including all imperfections and phenomena) and the mesh element chosen in the finite element model (shell 181) take into account the TSD. In this way, the suitability of the simplified approach in the analytical solution will be compared with other results and reported.

4.1.2. Natural frequency

Depending on application area of CFRP rods, natural frequency is of crucial importance as it is strongly related to structural integrity and performance. In order to evaluate the worst case scenario during the design process, the boundary conditions of the rod are evaluated as simply supported. However, it should be noted that in real cases, factors such as the stiffness, density, and other boundary conditions of the joints will naturally increase the natural frequency. The expression for the lowest fundamental frequency is as follows:

$$f_n = \frac{\pi}{2}\sqrt{\frac{E_x I}{mL^4}} \tag{4.26}$$

in which m is the mass per length. The remaining parameters are highly similar to the critical buckling load equation (see equation 4.25). This indicates that the natural frequency will also be improved in the optimization to improve the buckling load.

4.1.3. Torsional stiffness

The expression of torsional stiffness of CFRP rods is given as:

$$K = \frac{T}{\Phi} = \frac{G_{xy} I_p}{L} \tag{4.27}$$

where K refers to torsional stiffness, I_p is polar moment of inertia, and L is the length of the shaft. Moreover, T is applied torque and Φ is the angle of twist. In this fashion, the equation is rewritten and Φ is used as a design constraint during the optimization process.

CHAPTER 5

ANALYTICAL AND FINITE ELEMENT MODELING

The design and analysis of composite structures in engineering requires careful consideration of detail and a thorough understanding of material behavior. Composite materials are increasingly used in vital applications in the aerospace industries due to their outstanding strength-to-weight ratios and tailorability. During the design and analysis phases, engineers must take into account a number of key factors to ensure that these structures operate safely under a variety of conditions. The process of evaluating composite structures is described in the following sections, paying particular attention to deflections, buckling loads, natural frequencies and the location and magnitude of the maximum stress. When it comes to practical applications, each of these factors is essential in determining the structural integrity, safety and functionality of composite materials. The design challenge is to obtain the ideal tube diameter to wall thickness ratio that will produce the highest operating stress and consequently the lowest tube weight. As an additional design option, the shape of the composite tubes is affected by extra design options such as fiber orientation and stacking sequence that need to be decided. By optimizing fiber orientation and layer alignment depending on loading and boundary conditions, CFRP can be used instead of traditional materials in challenging environmental conditions without compromising mechanical properties.[74]

CFRP tubular compression-tension members are commonly utilized in aerospace structures such as flight control (pull-push) rods, support struts, rocket hull, and satellite trusses. The main goal in designing these compression members, which are primarily composed of thin or relatively thin tubes, is to prevent both local and overall column buckling.

5.1. Analytical Modeling

During the period between the 1900s and 1960s, methods were developed to predict the buckling load of shell structures. However, studies on thin-walled cylinders during this time revealed buckling loads much lower than those predicted by analysis. To

address this, conservative empirical correlation factors (referred to as buckling knockdown factors or KDFs) were developed to modify analytical predictions. These KDFs were derived from the lower bounds of the experimental data. NASA published these KDFs and related design guidelines in a series of spacecraft design monographs in the late 1960s and early 1970s.[75–79] Numerous in-depth research studies have investigated the behavior of CFRP cylindrical shells when subjected to axial compression, with a specific focus on buckling in composite cylindrical shapes. The accompanying Figure 5.1 provides a comprehensive overview of the buckling behavior of various CFRP shells in relation to KDF and the radius-to-thickness ratio (R/t) of the cylinder. This insightful figure encapsulates findings from research spanning from 1975 to the present day.[80,81]

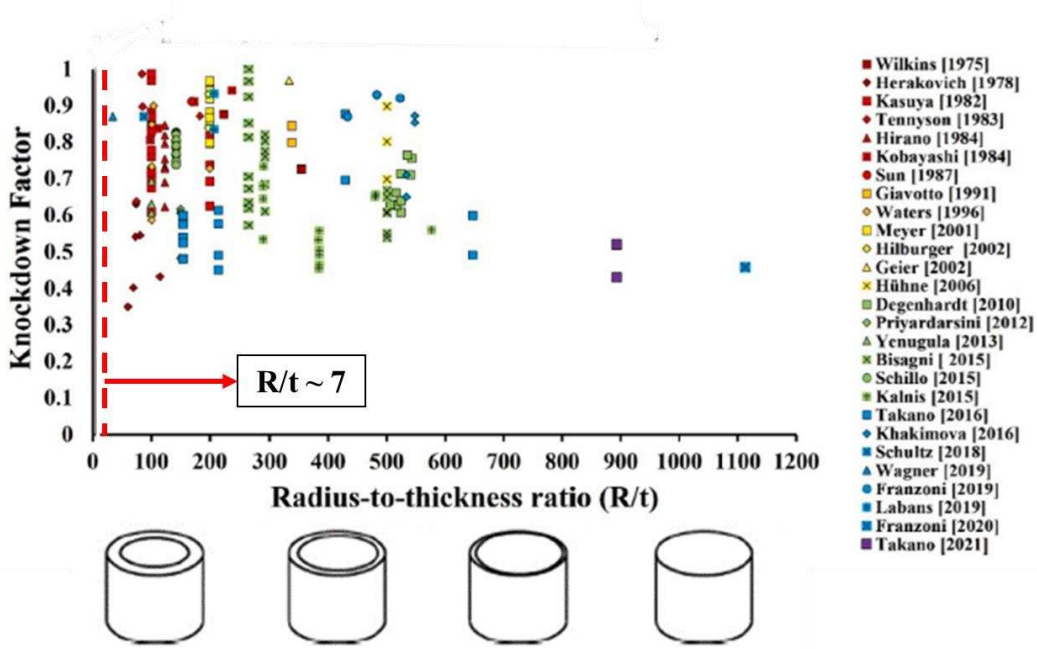

Figure 5.1 Axial compressed cylindrical shells' experimental data distribution for various R/t ratios

As can be seen in Figure 5.1, there is a significant decrease in the trend of the RDF as it approaches to the right (as the R/t ratio increases). Thin shell structures, despite their attractiveness, require careful consideration of imperfections. Factors such as shell wall thickness variations, manufacturing flaws, resin distribution, ply angle deviation, boundary conditions, and other elements can reduce buckling loads compared to theoretical expectations.[82–91]

In this study, in a range where there are almost very few studies in the literature R/t ~ 7.16, the critical buckling load, natural frequency and torsion angle of a CFRP rod with an R/t ratio of ~ 7.16 and a length of 800 mm were calculated using smeared properties without considering TSD.

The transverse shear modulus is influenced by the matrix material, while the elasticity modulus is influenced by the fibers. When examining relatively thick composite shells, it's crucial to account for transverse shear deformation to ensure precise characterization. Nevertheless, for preliminary design, the impact of transverse shear deformation can frequently be overlooked, simplifying the governing equations. By understanding these factors, we can confidently navigate the complexities of composite materials with precision and efficiency.[69]

A, B, and D matrices were calculated with the CLT explained in detail in Chapter 4 and critical buckling load, natural frequency and torsion angle were calculated analytically with Equation (4.25), (4.26) and (4.27) by in-house written MATLAB[92] code (see Appendix C). Overall, the result of the smeared properties calculated by neglecting TSD will be compared with the experimental and finite element method results.

5.2. Finite Element Modeling

In the world of engineering and scientific exploration, finite element modeling (FEM) plays a pivotal role in understanding and foreseeing the behavior of intricate structures under various circumstances. This powerful technique facilitates a thorough examination of material stress, strain, and deformation, empowering the optimized designs and solutions that align with performance and safety requirements.[93–95]

FEM has a lot of advantages over conventional analytical techniques, especially when working with complicated materials and geometries. The complexities of real-world systems, particularly those with heterogeneous and anisotropic features, are frequently too complex for analytical solutions to capture fully and, hence, tend to idealize the environment or boundary conditions. FEM, on the other hand, may reduce a structure into smaller, more manageable pieces, resulting in accurate and dependable conclusions that analytical techniques cannot match. Throughout the preliminary and final design stages of a project, modifications are often made between the analytical solution and the

finite element solution. In some cases, solution processes are concurrently managed, considering factors such as time and cost.

In this study, the composite lay-up of the CFRP rod was completed using the ACP module in the ANSYS[96] finite element package program, and the buckling, natural frequency, and torsion angle analyses were performed using the static structural modules.

Constructed project schematic can be seen in Figure 5.1.

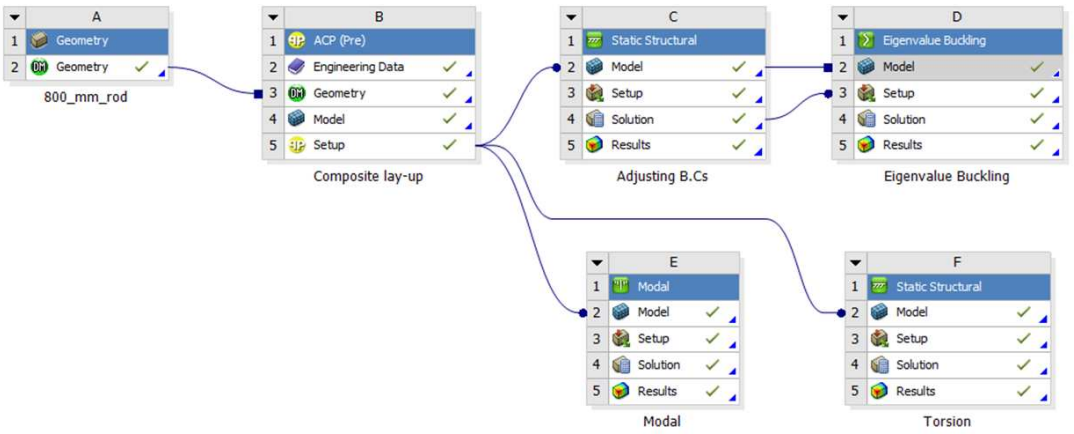

Figure 5.2 Project schematic of CFRP rod regarding composite lay-up, buckling, modal, and torsional analysis

Meshing plays a vital role in finite element analysis by allowing us to break down intricate geometries into smaller elements, which is key for achieving accurate simulations. A thoughtfully constructed mesh enhances the precision of results and optimizes computing efficiency. Conversely, an inadequately designed mesh can result in inaccuracies and increased processing costs. Thus, prioritizing proper meshing is fundamental for obtaining dependable FEA outcomes. Apart from solid elements, shell elements are a valuable tool for addressing structural challenges using the finite element method. Utilizing shell elements can lead to reduced computation time by necessitating fewer mesh elements and nodes in the model, thereby reducing calculation errors. Overall, the application of shell elements signifies a significant advancement in structural analysis.

The analysis of thin to moderately thick shell structures is suitable for SHELL181. In particular, since first-order shear deformation is important for the accuracy of the model in relatively thick layered structures, it is beneficial to design layered structures such as relatively thick and thin rods such as the CFRP rod in this study with this element (accuracy is governed by Midlin-Reissner Theory).[96] This element consists of four nodes,

each with six degrees of freedom: rotation around the x, y, and z axes, as well as translation along those axes. If the membrane option is chosen, the element's degrees of freedom will be limited to translation. The Shell181 element can be shown in Figure 5.3.

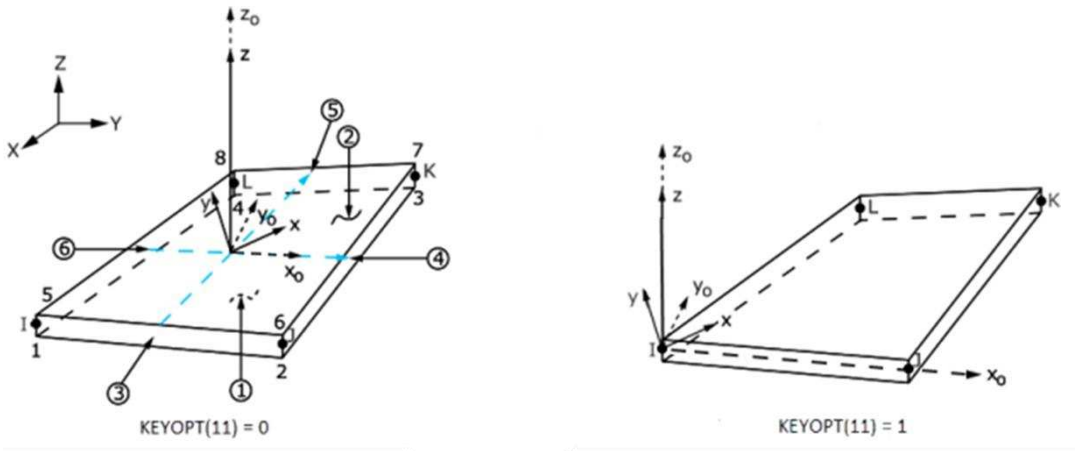

Figure 5.3 Geometry of Shell181 element

5.2.1. Eigenvalue Buckling Modeling

As mentioned in previous section, the length of CFRP rod was 800 mm, and its inner and outer diameters were 20 mm and 23 mm, respectively. As a reference model, stacking sequence was set $[\pm 45]_{6.}$ 27268 nodes and 13860 elements were employed to generate mesh, and boundary conditions of the rod for buckling are illustrated in Figure 5.4.

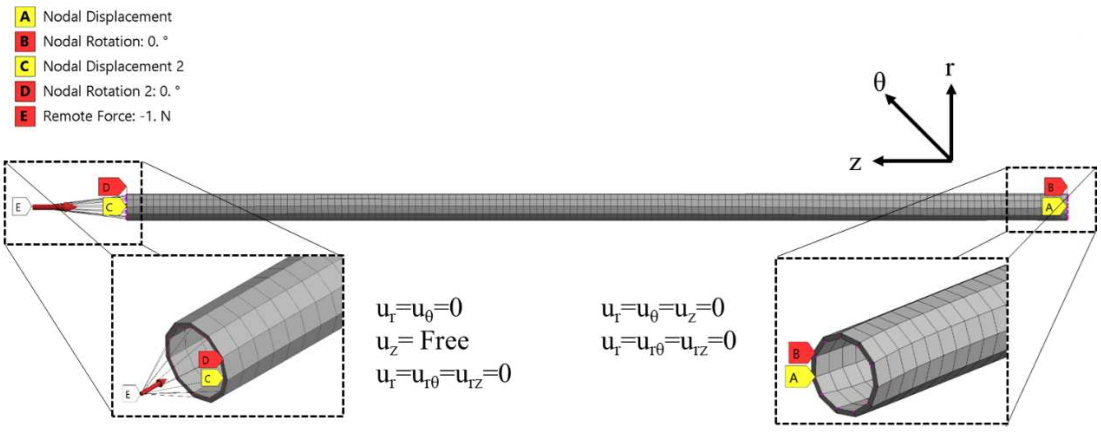

Figure 5.4 Boundary conditions of linear buckling model

5.2.2. Natural Frequency Modeling

Although there will be an improvement in natural frequency due to end fittings in real application areas, both ends of the CFRP rod were simply supported in order to evaluate the worst-case scenario. Boundary conditions can be seen in Figure 5.5.

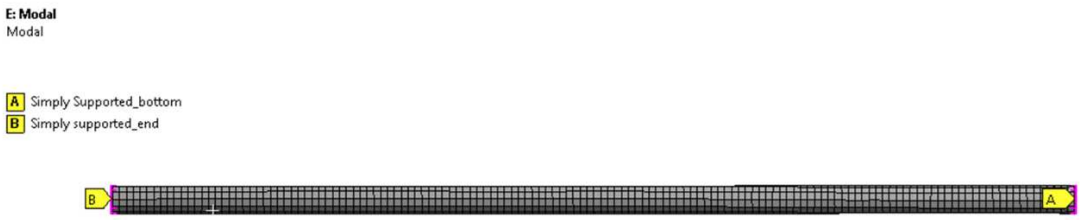

Figure 5.5 Boundary conditions of natural frequency model

5.2.3. Torsional Stiffness Modeling

For the angle of twist, one end is modeled as fully constrained and the other end is modeled as free. 2000 N mm moment was applied to investigate angle of twist at free end. Since the angle of twist could not be measured directly, the effect of 2000 N mm moment was analyzed by typing APDL command. Boundary conditions is illustrated in Figure 5.6.

Figure 5.6 Boundary conditions of torsional stiffness model

The buckling, natural frequency and angle of twist results of CFRP modeled as reference are shared in the results section to be compared with other results.

CHAPTER 6

OPTIMIZATION

To achieve a specific goal while working within specific constraints, optimization is necessary. Many instances of optimization can be observed in nature: for instance, droplets in zero gravity take on a spherical shape to minimize surface area, atoms in metals arrange themselves into efficient unit cells, and trees and honeycombs are optimized for both structural strength and space utilization. Similarly, companies and organizations strive to find the best solutions, driven by market demands and competition. Effective optimization can lead to significant cost savings and efficiencies, such as reduced expenses in mass production, improved vehicle fuel economy, and maximizing profits through resource efficiency. Furthermore, businesses can save time and money by organizing their design processes.[97]

Optimization involves finding the best conditions that lead to either the highest or lowest value of a function based on certain factors in a real-world scenario. In Figure 6.1, it is shown that when a point x* represents the minimum value of the function f(x), it also represents the maximum value of the negative function, -f(x). Therefore, without loss of generality, optimization can be defined as minimization since the maximum value of a function can be found by locating the minimum of its negative.[98]

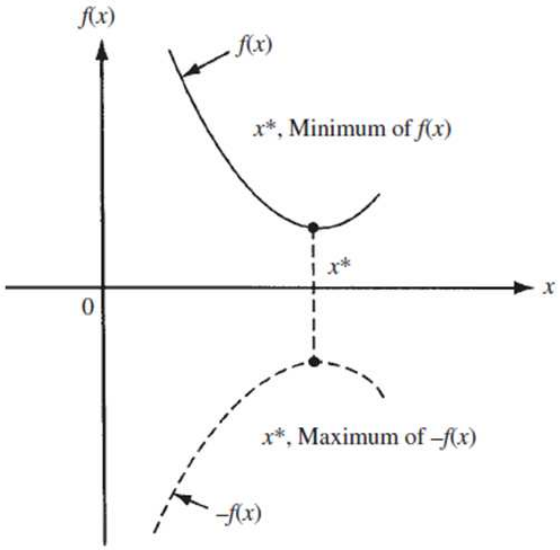

Figure 6.1 Minimum and maximum of an objective function

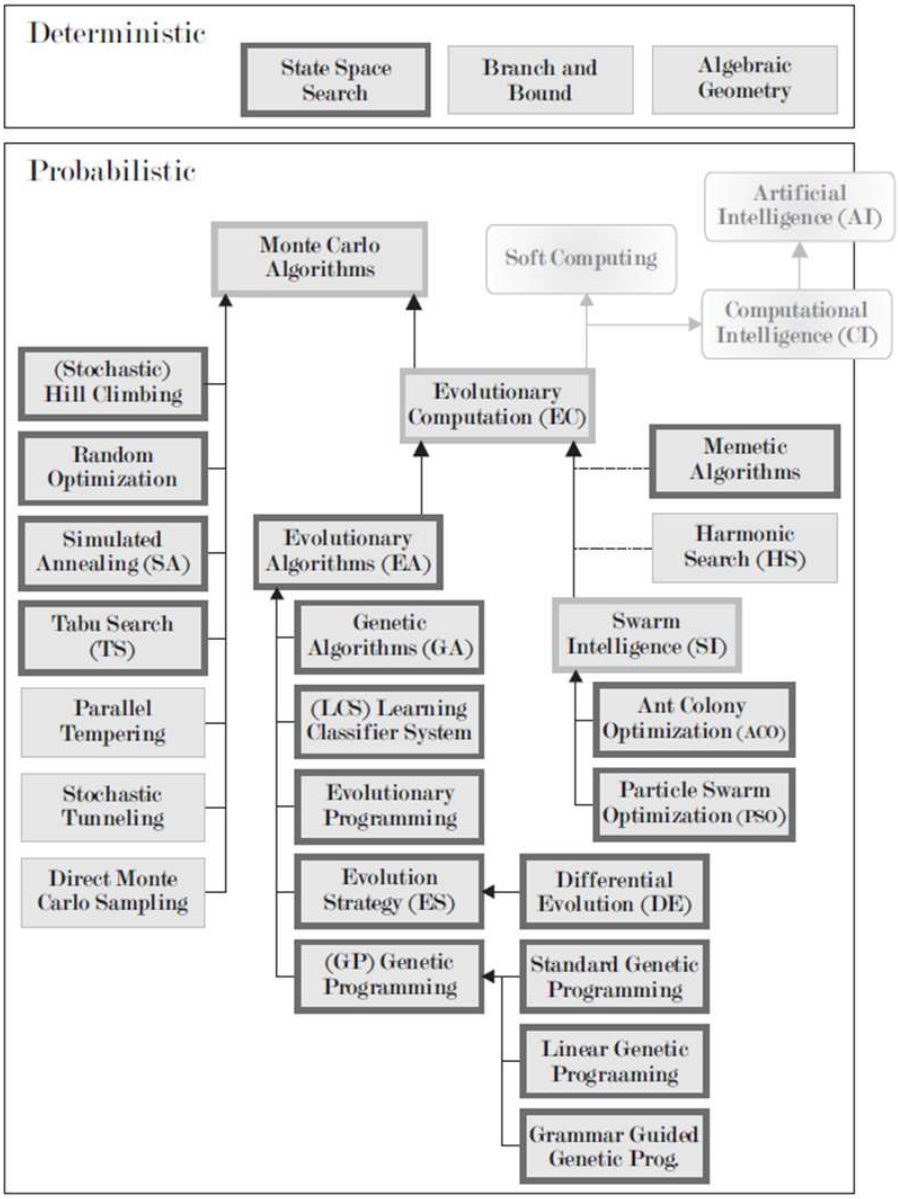

Figure 6.2 Classification of optimization algorithms

As shown in Figure 6.2, global optimization techniques are typically classified as deterministic or probabilistic. When there is a clear relationship between the characteristics of possible solutions and their usefulness for a given problem, deterministic algorithms are frequently employed. In such cases, the search space can be efficiently explored using methods like divide and conquer. Probabilistic algorithms are used, which compromise the assured correctness of the answer for a shorter runtime. The outcomes you get from using them might not be the global optima, but that doesn't mean they're entirely wrong. However, a solution that is only marginally better than the best available one is still preferable than one that takes centuries to find.[99]

In the literature, many deterministic[100–106] and probabilistic[27,49,107–112] (especially genetic algorithms) studies are used to optimize composite structures.

In this thesis, optimization processes were conducted for CFRP rods with fixed geometric dimensions (diameter, thickness, and length) to withstand buckling damage under a specific load. The objective function, design criteria, and variables will be explained in detail in the upcoming sections.

6.1. Generic Definition of Optimization Problem

Depending on the topic and requirements, optimizations can be performed with single or multiple objective functions. In this thesis , as in structural optimization, the design problem in the given equation typically consists of the minimization of a selected objective function $f_0(x)$ subject to a particular set of constraints $g_j(x)$ and $k_j(x)$:

$$\begin{aligned} &\min f_0(x) && \\ &g_j(x) \leq 0 && j = 1 \dots m \\ &k_j(x) = 0 && j = 1 \dots n \\ &x_i^L \leq x_i \leq x_i^U && i = 1 \dots p \end{aligned} \tag{6.1}$$

where $f_0(x)$ represents the objective function, which generally describing mass, cost, buckling load, stiffness, and natural frequency of composite structures. $g_j(x)$ and $k_j(x)$ are known as inequality and equality constraints. Depending on the composite structures and operating environment, they could represent the number of layers, angle of

twist, natural frequency, etc. Finally, x_i as design variable(s) can correspond to the thickness, diameter, length, fiber angles of the composite structure.

Compared to other optimization techniques, genetic algorithms (GAs) provide a number of benefits, most notably the capacity to address complicated, nonlinear, and multimodal problem spaces. GAs employ a population-based search strategy that simultaneously searches numerous regions of the solution space, improving the possibility of finding global optima, in contrast to traditional methods that require gradient information or are prone to being caught in local optima. They are quite flexible and can be used to solve a variety of issues without requiring major adjustments. Because GAs use probabilistic transition rules instead of deterministic ones, they can sustain population variety and navigate dynamic situations with ease, making them resilient to changes in the problem domain. In the optimization of structural polymer matrix composites, where many design variables and material parameters interact to form an extremely complicated optimization environment, GAs are essential. GAs are adept at navigating this complexity and can find the best configurations to increase durability, decrease weight, and improve mechanical performance. This feature is especially crucial in sectors like aerospace and automotive, where the use of complex composite materials is growing to attain higher performance and efficiency.

In this study GA optimization method, which has proven itself in this design field with many examples in the literature, is used. Detailed information about GA is explained in the following section.

6.2. Genetic Algorithm

Genetic algorithms are based on the principles of natural genetics and natural selection. They use the basic elements of natural genetics – the selection, crossover, and mutation – in the genetic search procedure.[113] Schematic presentation can be seen in Figure 6.3.

The selection of individuals for reproduction involves using random methods and assigning fitness values. A rank-based fitness assignment is used to overcome scaling issues. This reduces the probability of selecting a design with low fitness, though it's still possible, allowing even weaker designs to be used for generating offspring.

The crossover operator, two parent individuals recombinate to produce two offspring by transferring information across their chromosomes. The objective is to maintain population diversity (exploration) while producing individuals with superior features (exploitation). Crossover is regarded as genetic algorithms' principal search operator.

The mutation results in random variation in the genes of the offspring chromosome. Each gene is given a specific probability or mutation rate for selection. The normal distribution function of each gene, with its mean value as the base, forms the basis for real-valued mutation. Mutation is the main search operator for evolutionary strategies (ES) and may also be used after recombination. The control parameters for mutation are the mutation rate and the standard deviation, which are determined in relation to the variable range. These values may remain constant or change as the algorithm runs. Figure X shows the schematic presentation of GA steps.

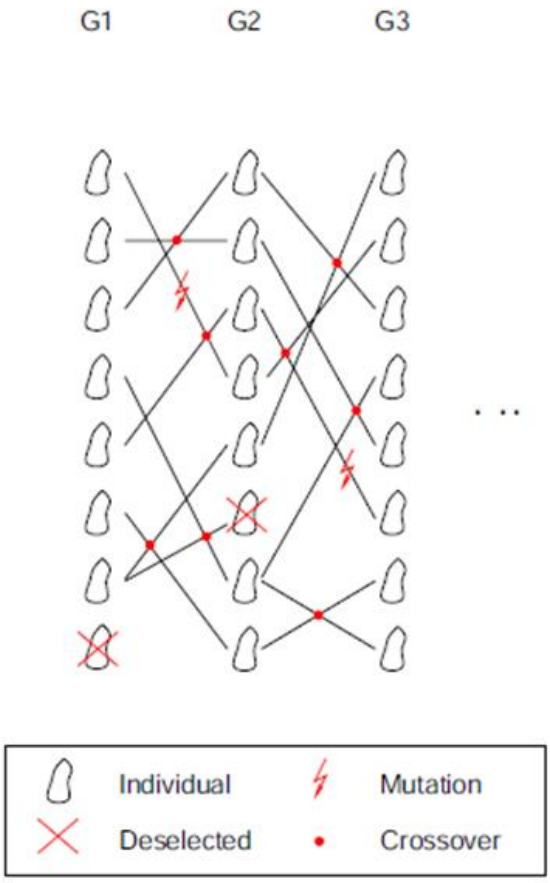

Figure 6.3 An illustration of the genetic algorithm flow.(Source: Dynardo, 2020)

In this thesis, a single objective optimization process is conducted with MATLAB®[92] using the GA optimization method. The optimization process was proceeded with the default parameter set provided by MATLAB®[92] for the GA. The parameter set employed is listed in Table 6.1.

Table 6.1 Default parameter set of GA

POPULATION TYPE	DOUBLE VECTOR
POPULATION SIZE	200
CREATION FUNCTION	
INITIAL POPULATION	[ ]
INITIAL SCORES	[ ]
INITIAL RANGE	[-300;-100]
SELECTION FUNCTION	Tournament, Tournament size=4
ELITE COUNT	PopulationSize*0.05
CROSSOVER FRACTION	0.8
MUTATION FUNCTION	Use constraint dependent
CROSSOVER FUNCTION	Scattered
MIGRATION DIRECTION	Both Fraction=0.2, Interval=20
INITIAL PENALTY	10
PENALTY FACTOR	100
HYBRID FUNCTION	None
STOPPING CRITERIA	Generation=600, Stall generation=50 Function tolerance=10^-6

6.3. Optimization Problem Definition

In this thesis, since the thickness, diameter and length values of the CFRP rod are kept constant, only the ply angle orientations (discrete variables) are used as design variables to optimize the buckling, natural frequency and torsional stiffness. Mathematical representation of the single-objective optimization problem with design constraints and variables is:

$$Objective\ function:\ max\ \lambda_{cr}\ (mode\ 1) \tag{6.2}$$

$$Design\ constraints:\ f_n \geq 150\ Hz,\ \phi_z \leq 0.65° \tag{6.3}$$

$$20° \leq \pm\theta_i \leq 87°,\ \ i = 1,2 \ldots 6 \tag{6.4}$$

$$Design\ variables:\ [\pm\theta_1/\pm\theta_2/\pm\theta_3/\pm\theta_4/\ \pm\theta_5\ /\pm\theta_6] \tag{6.5}$$

where

λ_{cr} is eigenvalue buckling of CFRP rod (mode 1)

f_n is the fundamental natural frequency of CFRP rod,

ϕ_z is the angle of twist of CFRP rod, and

$\pm\theta_i$ is angle of each layer of the CFRP rod.

As shown in Figure 6.4, the angle-ply layer is composed of an even number of alternating plies with angles of $\pm\theta_i$.Nominal thickness of CFRP rod is 1.5 mm and each ply consist of balanced laminates, $\pm\theta_i$ orientation.

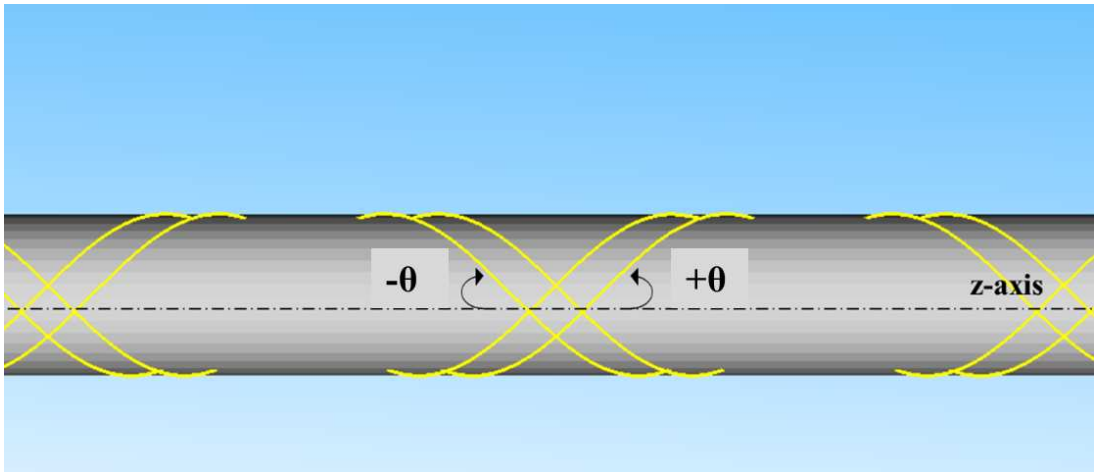

Figure 6.4 Angle orientation during filament winding

CHAPTER 7

EXPERIMENTAL AND NUMERICAL RESULTS

7.1. Mechanical Characterization Results

The following section presents the results of the mechanical characterization studies described in Chapter 3, focusing on tensile evaluations along both the 0° and 90° directions, compressive analyses in the respective directions, and v-notch examinations performed systematically to clarify the structural properties of the specimens.

Through the empirical knowledge acquired from the mechanical characterization, this research aims to validate the quality and integrity of the filament winding manufacturing process and identify opportunities to optimize material selection and process parameters. Eventually, the findings from this mechanical characterization study are poised to inform more robust design and manufacturing practices and contribute to the continued advancement of lightweight, high-performance composite structures.

7.1.1. Tensile Test Results

5 specimens were tested to evaluate the mechanical properties related to the tensile test and a photo of the specimen after testing is provided in Figure 7.1.

Figure 7.1 0° oriented specimens after tensile test

The results of elastic modulus, longitudinal tensile strength and Poisson's ratio of 0° oriented specimens are presented in Figure 7.2. The average elastic modulus was determined from extensometer strain as 106.37±3.41 GPa. Further, the average tensile strength in the longitudinal direction was computed as 1621.31±42.64. Finally, ignoring instances 2 and 3 where considerable deviation occurred, the average Poisson's ratio was found to be 0.033±0.026.

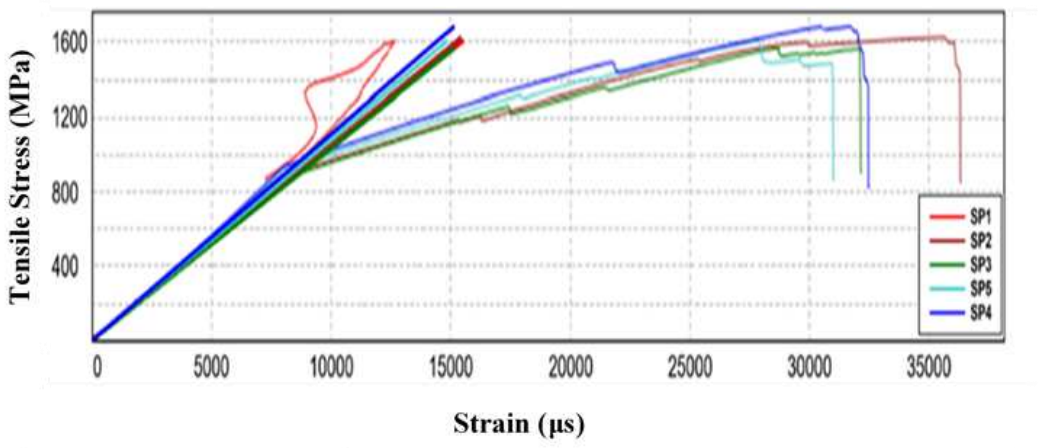

	Specimen ID	Width [mm]	Thickness [mm]	Maximum Load [kN]	Modulus [GPa]	Tensile Strength [MPa]	Poisson's ratio (Chord)
1	SP1	24.85	3.05	122.11	103.40	1611.08	0.31
2	SP2	25.71	3.07	128.53	105.35	1628.45	0.07
3	SP3	26.00	2.99	122.05	103.49	1569.93	0.01
4	SP5	24.53	3.03	119.66	108.26	1609.87	0.32
5	SP4	24.70	2.93	121.98	111.35	1687.24	0.37
Mean		25.16	3.01	122.86	106.37	1621.31	0.22
Standard deviation		0.65	0.06	3.33	3.41	42.64	0.17
Maximum		26.00	3.07	128.53	111.35	1687.24	0.37
Minimum		24.53	2.93	119.66	103.40	1569.93	0.01
Coefficient of variation		2.60	1.88	2.71	3.21	2.63	76.67

Figure 7.2 Tensile test results (0° direction)

On the other hand, the test results of the 90° oriented specimens are also presented in Figure 7.3. The elastic modulus value was measured by means of a mechanical extensometer, as was done for the 0° specimens. The average elastic modulus was determined as 8.03±0.61 GPa from the extensometer strain. Furthermore, the average tensile strength in the transverse direction was calculated as 33.3±4.365. Finally, since E1, E2 and υ_{12} are known, υ_{21} was calculated empirically.

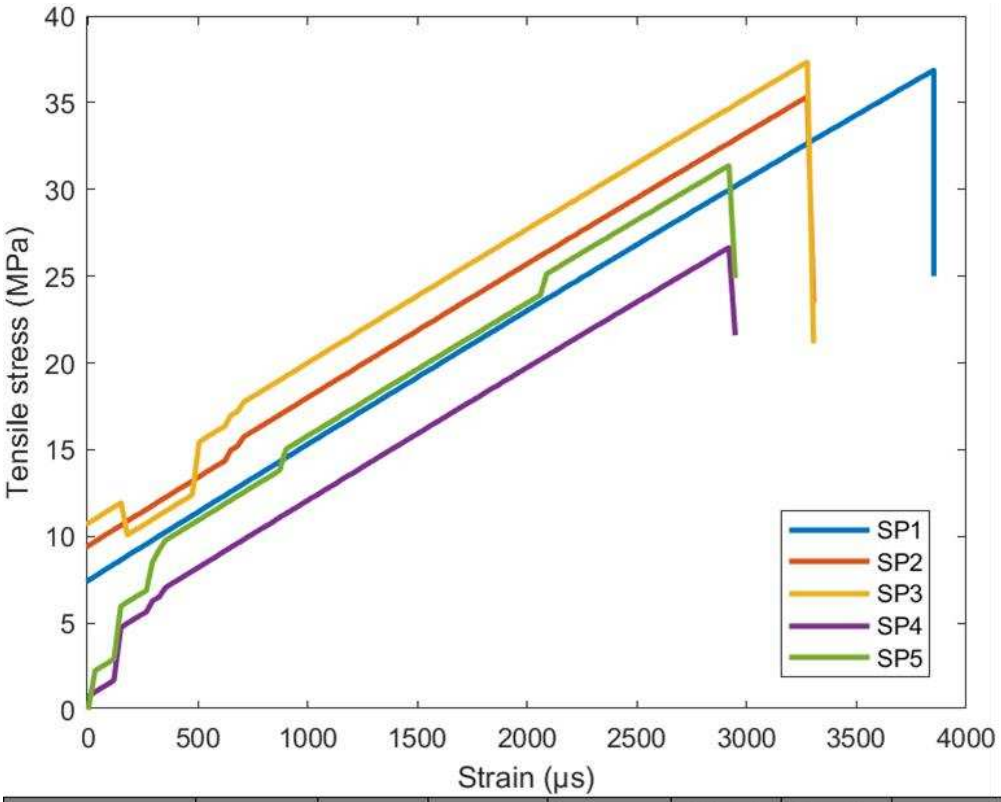

	Specimen ID	Width (mm)	Thickness (mm)	Maximum Load (kN)	Chord Modulus (GPa)	Tensile Strength (MPa)	Poisson's Ratio
1	SP1	24.98	2.55	2.35	7.64	36.87	0.022*
2	SP2	25.23	2.94	2.42	7.72	35.33	0.022*
3	SP3	25.12	2.63	3.01	8.30	37.30	0.022*
4	SP4	24.6	2.58	2.22	7.41	25.64	0.022*
5	SP5	25.1	2.7	3.45	9.10	31.37	0.022*
Mean		25.006	2.68	2.69	8.03	33.30	0.022*
Std.		0.21795	0.140	0.467	0.610	4.365	0
Maximum		25.23	2.94	3.45	9.102	37.3	0.022*
Minimum		24.6	2.55	2.22	7.405	25.64	0.022*
Coefficient of variation (%)		0.9%	5.2%	17.4%	7.6%	13.1%	

Figure 7.3 Tensile test results (90° direction)

7.1.2. Compression Test Results

In order to evaluate the mechanical properties related to the compression test, 5 specimens were tested and the post-test images of the specimens were provided in Figure 7.4. When Figure 7.4 was reviewed, CIT (end crushing-inside tab-tip), which was the unacceptable failure mode shown in ASTM D6641 standard, was detected for specimen No. 1 and hence its results were not included calculation.

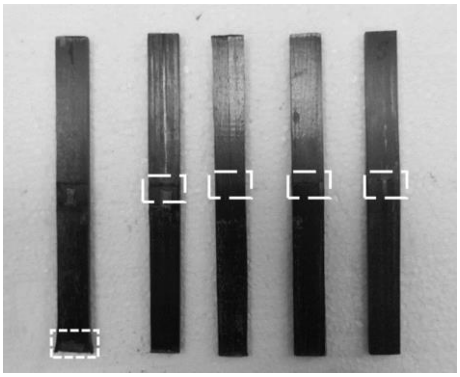

Figure 7.4 0° oriented specimens after compression test

The average longitudinal compressive strength (X_c) was calculated as 396.54±23.6 MPa considering the maximum load and material dimensions. The load-displacement graph and related parameters were given in Figure 7.6. On the other hand, 90° oriented five specimens were also tested and the post-test images of the specimens were provided in Figure 7.5. the average longitudinal compressive strength (Y_c) was calculated as 88.36±16.707 MPa. The load-displacement graph and related parameters were given in Figure 7.7.

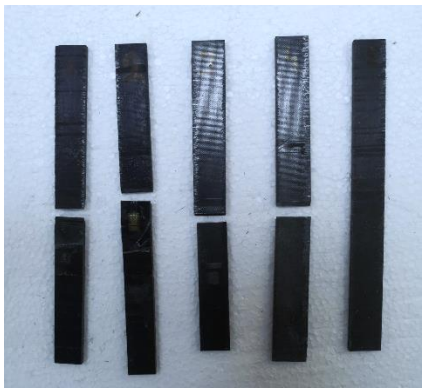

Figure 7.5 90° oriented specimens after compression test

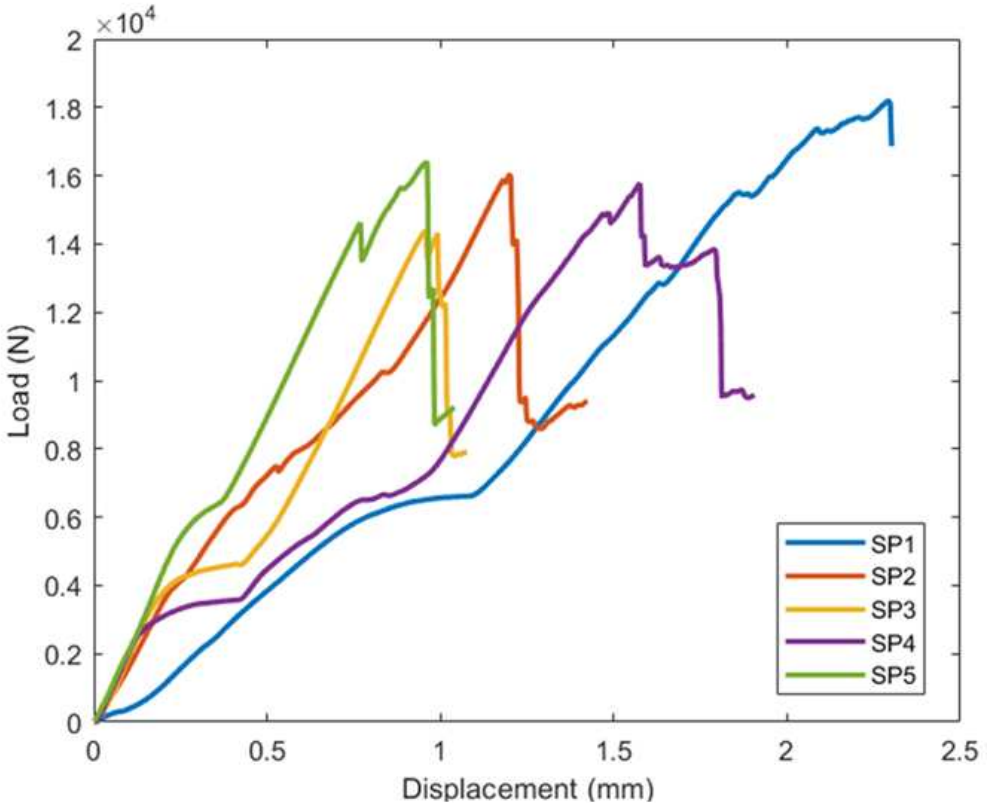

	Specimen ID	Width (mm)	Thickness (mm)	Maximum Load (N)	Compressive Strength (MPa)
1	SP1	14	2.82	18188.75	460.71
2	SP2	13.33	2.87	16019.38	418.73
3	SP3	13.27	3.04	14403.75	357.05
4	SP4	12.73	3.03	15771.88	408.90
5	SP5	13.14	3.11	16407.5	401.50
Mean		13.294	2.974	16158.252	396.54
Std.		0.410394932	0.110	1219.171	23.606
Maximum		14	3.11	18188.75	418.73
Minimum		12.73	2.82	14403.75	357.05
Coefficient of variation (%)		3.1%	3.7%	7.5%	6.0%

Figure 7.6 Compression test results (0° direction)

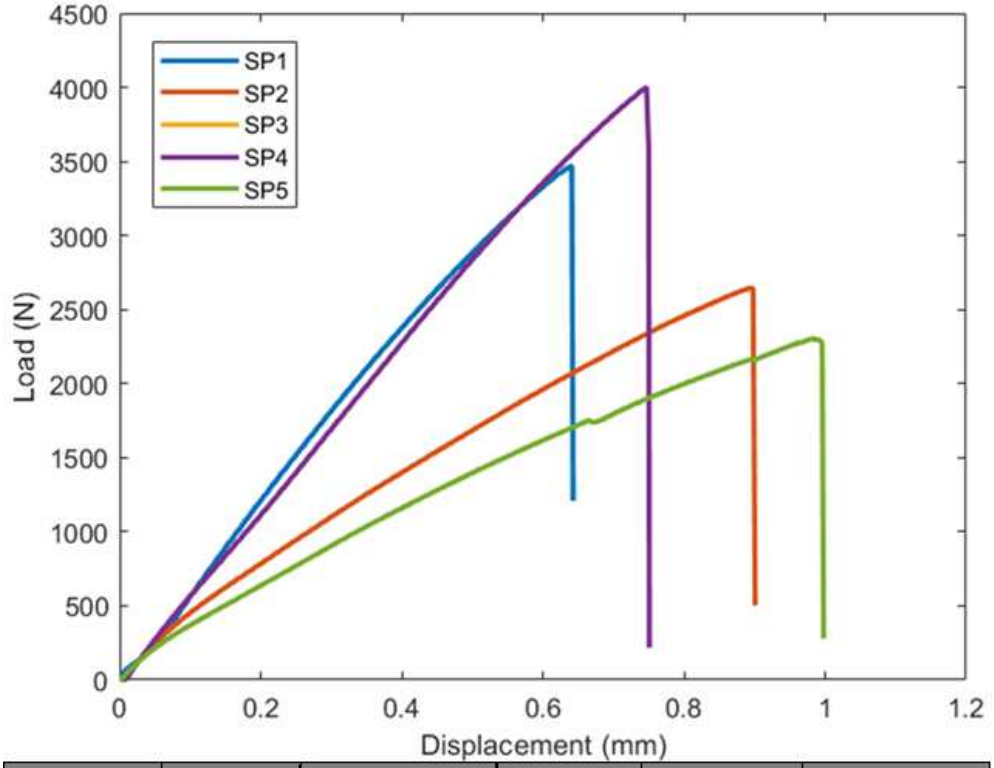

	Specimen ID	Width (mm)	Thickness (mm)	Maximum Load (N)	Compressive Strength (MPa)
1	SP1	13.21	2.55	3467.813	102.95
2	SP2	13.35	2.37	2645.781	83.62
3	SP3	14.6	2.5	2305	63.15
4	SP4	15.5	2.34	4000.938	110.31
5	SP5	14.32	2.52	2951.563	81.79
Mean		14.196	2.456	3074.219	88.36
Std.		0.844620625	0.085	600.671	16.707
Maximum		15.5	2.55	4000.938	110.31
Minimum		13.21	2.34	2305	63.15
Coefficient of variation (%)		5.9%	3.4%	19.5%	18.9%

Figure 7.7 Compression test results (90° direction)

7.1.3. V-notched Shear Test Results

0° oriented five specimens were tested to evaluate the mechanical properties such as shear modulus (G_{12}) for the v-notch shear test and shear strength in the 1-2 plane (S_L). The test setup and pre-test specimen images are shared in the following Figure 7.8.

The results of shear modulus (G_{12}), shear strength in plane 1-2 were shown in Figure 7.9. The average shear modulus was obtained from strain gauges as 3.98±0.07 GPa (Relatively low it can be attributed to fact that notch operation). Further, the average tensile strength in plane 1-2 was computed as 34.39±1.593 MPa.

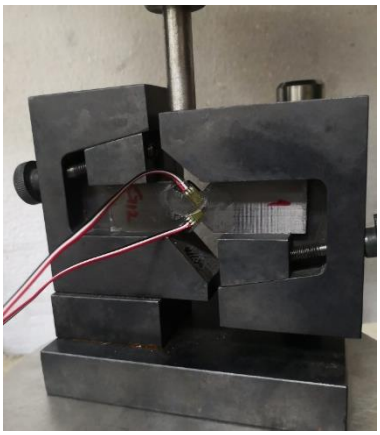

(a)

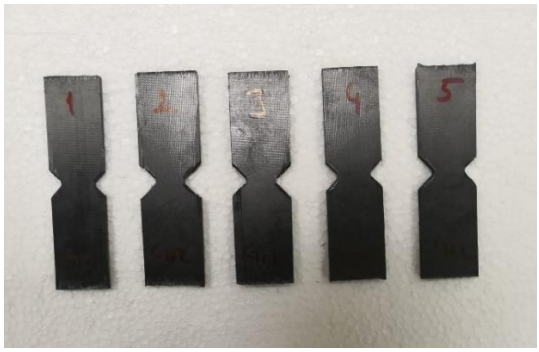

(b)

Figure 7.8 V-notched beam method to find G_{12} and S_L (a) test setup and (b)before the tests

In summary, the results obtained from the mechanical characterization (based on related standards), which will provide input to the finite element model, are presented in the Table 7.1.

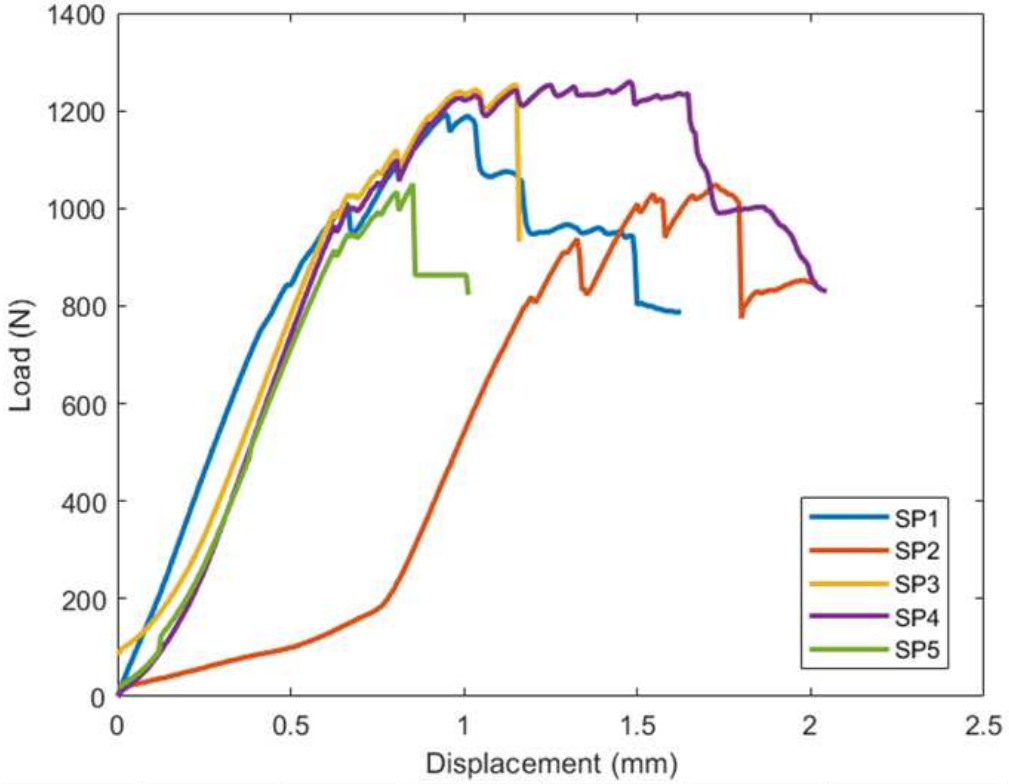

	Specimen ID	Width (mm)	Thickness (mm)	Maximum Load (N)	Shear Modulus (G_{12})	Compressive Strength (MPa)
1	SP1	11.97	2.77	1200	4.1	36.19
2	SP2	10.22	2.84	1050	4.02	36.18
3	SP3	12	3.06	1260	3.88	34.31
4	SP4	11.2	3.15	1150	3.92	32.60
5	SP5	11	2.84	1020	3.98	32.65
Mean		11.278	2.932	1136	3.98	34.39
Std.		0.66376	0.146	90.022	0.070	1.593
Maximum		12	3.15	1260	4.1	36.19
Minimum		10.22	2.77	1020	3.88	32.60
Coefficient of variation (%)		5.9%	5.0%	7.9%	1.8%	4.6%

Figure 7.9 V-notched beam method test results (0° direction)

Table 7.1 Mechanical characterization results

Standards	Description	Value
Tensile Test (ASTM D3039-14)	E_1	106 GPa
	E_2	8 GPa
	X_T	1621 MPa
	Y_T	33.5 MPa
	v_{12}	0.32
Compression Test (ASTM D6641-09)	X_C	410 MPa
	Y_C	94 MPa
V-notched Shear Test (ASTM D7078-12)	$G_{12} = G_{13}$	4 GPa
	G_{23}	1.8 GPa
	S_L	63 MPa
	S_T	41 MPa

7.1.4. Thermomechanical Characterization Results

The temperature ranges at which a material changes from a rigid, glassy state to a more flexible, rubbery state is known as Tg, and it is an essential parameter for composite materials. It is crucial to understand Tg to predict how composites will behave in different thermal environments and ensure they retain the necessary mechanical qualities and structural integrity.

In the test, a dynamic force applied at a frequency of 1 Hz was conducted using a three-point bending mode. The temperature range, which extends from 20 to 200ºC, was intended to increase at 3ºC per minute. The test result is shown in Figure 7.10 and the Glass transition temperature was determined as 147.1ºC.

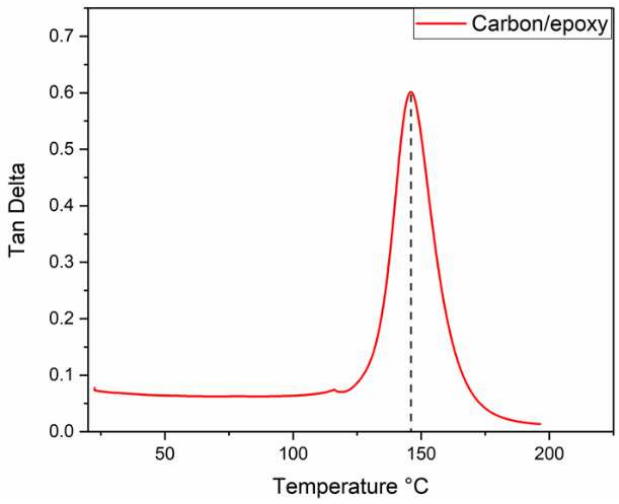

Figure 7.10 Tan delta of carbon/epoxy specimen

7.2. FEM Results

While establishing the finite element model based on Eigenvalue analysis, CFRP rod was considered as a thin-walled composite, and a linear buckling model was prepared. The composite rod was modeled in ANSYS ACP Pre module by employing Shell181 element. The length of CFRP rod was 800 mm, and its inner and outer diameters were 20 mm and 23 mm, respectively. As a reference model, stacking sequence was set $[\pm 45]_6$. 1551 nodes and 1540 elements were employed to generate mesh, and The boundary conditions of the bar for buckling are also shown in Figure 5.4 as described in Chapter 5.

In order to evaluate relatively the most demanding design scenarios including natural frequency and torsional stiffness comprehensively, both ends of rod were simply supported when setting the natural frequency model. Regarding the angle of twist, one end was designated as fully constrained while the other end was modeled as free.

5000 N load along z-direction was applied to investigate the linear buckling behavior of shell model. Other boundary conditions were also assigned to meet other design constraints such as angle of twist and modal analysis apart from buckling boundary conditions. One end fixed and other end was set free and 2000 N mm moment was applied to investigate angle of twist at free end. Lastly, ends were simply supported to characterize modal analysis. Overall results of the reference model were shared in Table 7.2.

Table 7.2 Reference model results

Stacking sequence	**λ_{cr} (Mode 1)**	**Φ_z**	**f_n (Mode 1)**
$\pm[45]_6$	0.967	0.47°	114.35 Hz

As evident from the findings, CFRP reference $\pm[45]_6$ rod exhibited buckling behavior under the applied load ($\lambda_{cr} < 1$). Despite initial considerations favoring the 45-degree lay-up for optimal twist angle, it proved vulnerable to buckling-induced damage. Additionally, first 4 buckling modes are shown in APPENDIX D. Therefore, stacking sequence and ply angles should be optimized to improve the critical buckling load while satisfying natural frequency and angle of twist constraints.

7.3. Optimization Results

As seen in reference model results in Table 7.2, it fails under given loading conditions. Additionally, natural frequency results do not satisfy design constraints. In order to provide a better stacking sequence solution, single-objective buckling damage optimization was performed using the GA optimization parameters specified in Table 6.1.

92 different versatile designs were generated during the process and the relationship between the design constraints and the objective function is illustrated in Figure 7.11.

Based on the optimization results, it was observed that λ_{cr} exceeded 3 in some stacking sequences, suggesting potential viability. However, a thorough evaluation of these instances was impeded due to their inability to meet all prescribed design constraints. Consequently, Table 7.3 presents the three most favorable designs that optimize critical buckling performance while concurrently adhering to all prescribed design criteria.

Table 7.3 Optimization results

		Obj. Func. Max. λ_{cr}	**Design criteria $f_n \geq 150$ Hz, $\phi_z \leq 0.65$**		**Axial and bending stiffness ratio**	
Designs	**Stacking sequence**	**λ_{cr}**	**f_n (Hz)**	**ϕ_z (°)**	**A_{11}/A_{22}**	**D_{11}/D_{22}**
REFERENCE	$[\pm 45]_6$	1	114.35	0.47	1	1
DESIGN-1	$[\pm 30_3/\pm 20_3]$	3.27	197.9	0.57	5.16	5.16
DESIGN-2	$[\pm 30/\pm 50/\pm 30/\pm 20_3]$	3.04	188	0.58	3.6	3.88
DESIGN-3	$[\pm 30/\pm 20_2/\pm 50/\pm 20_2]$	3.29	199.8	0.62	3.96	5.35

Further, axial stiffness ratio (A11/A22) and bending stiffness ratio (D11/D22) were also used to determine axial and circumferential stiffness. If the A11/A22 ratio is greater than unity, this means that the proposed stacking sequence is more rigid in the axial direction.[79,114] MATLAB code (see APPENDIX C) were written to calculate A and D matrices and results were also shared in Table 7.3.

Based on these results and also considering the ease of manufacturing, since other possible best designs change stacking sequence more often than DESIGN-1, it could lead to angle deviation and could decrease in mechanical properties. it is concluded that

DESIGN-1 (will be called optimum design) is relatively the best among other suitable GA optimization results.

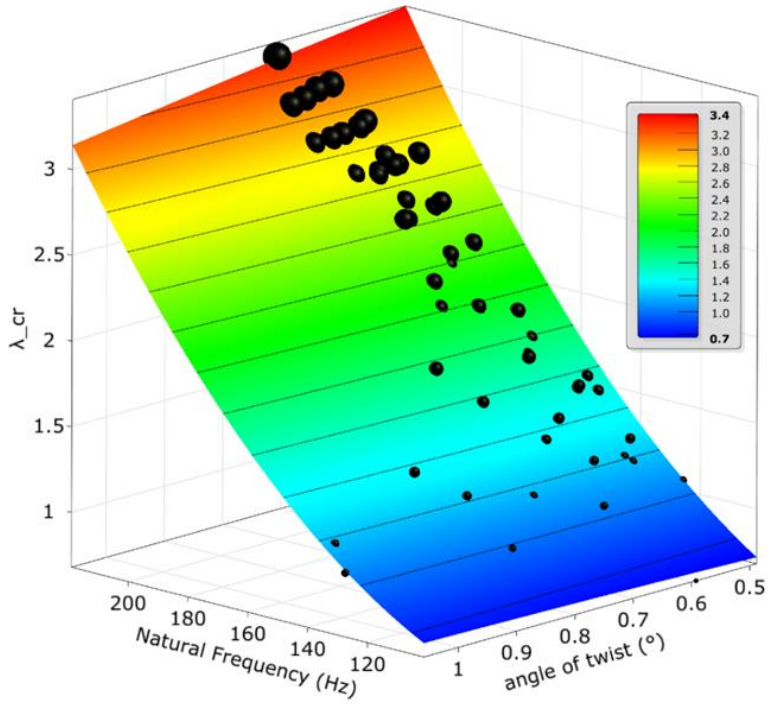

Figure 7.11 Optimization results with respect to design constraints

7.4. Buckling Test

As described in 3.3.1, A hydraulic MTS universal testing machine, featuring a 3000 kN load cell and platens, was used to subject the developed rods to axial compression at a displacement-controlled rate of 1 mm/min. In addition, axial and radial changes were also recorded by means of T-rosette strain gauges attached to the center point of the rods. In order to compare the results with the FEM, first the load-displacement results and then the strain gauge results are of $[\pm 45]_6$, $[\pm 30]_6$, and the optimized design are shared in the following.

7.4.1. Buckling Results of $[\pm 45]_6$ CFRP Rods

Figure 7.12 illustrates the buckling behavior of $[\pm 45]_6$ CFRP rods, comparing experimental data for three samples (45-1, 45-2, 45-3) with the finite element model (FEM) predictions. The maximum buckling forces recorded were 5.182 kN, 4.923 kN,

4.744 kN and the finite element estimate was 5 kN. The average buckling force from experiments was 4.94 kN with a standard deviation of 0.155 kN. The FEM result is close to the experimental average with 5 kN, demonstrating that the buckling behavior is reasonably predicted. Further, The CFRP rods' displacement-force curves demonstrate that their maximal forces were reached at about 3 mm of displacement. A reliable anticipating of buckling behavior was indicated by the finite element model's close alignment with the experimental data, both in load and displacement.

7.4.2. Buckling Results of $[\pm 30]_6$ CFRP Rods

The buckling behavior of $[\pm 30]_6$ CFRP rods is shown in Figure 7.13, which compares the predictions of FEM with experimental data for three samples (30-1, 30-2, and 30-3). The finite element estimate was 12.035 kN, while the maximum buckling forces reported were 13.37 kN, 12.048 kN, and 11.82 kN. The studies yielded an average buckling force of 12.41 kN with a standard deviation of 0.683 kN. With 12.48 kN, the FEM result is near the experimental average, showing that the buckling behavior is conveniently anticipated. Although the trends of FEM and experimental results sufficiently converge with each other, there is a 3% deviation in the displacement results. This can be attributed to the fitting of noisy data obtained during the testing process.

7.4.3. Buckling Test Results of Optimum CFRP Rods

The graph including buckling test performance of the optimum bars and their comparison with the finite element results are presented in Figure 7.14.

By comparing experimental findings from three samples (opt-1, opt-2, and opt-3) with predictions from FEM, Figure 7.14 depicts the buckling behavior of optimum CFRP rods. The FEM estimated 16.60 kN, however the maximum buckling forces that were recorded were 17.56 kN, 15.77 kN, and 14.84 kN, in that order. With the standard variation of 0.128 kN, the experimental mean buckling force is 16.05 kN, which is considerably similar to the FEM estimation. These results lead to the interpretation that the FEM can effectively predict the buckling load. The difference between the displacement values is found to be 8%. This is due to the fact that the first specimen is more displaced than the other two specimens.

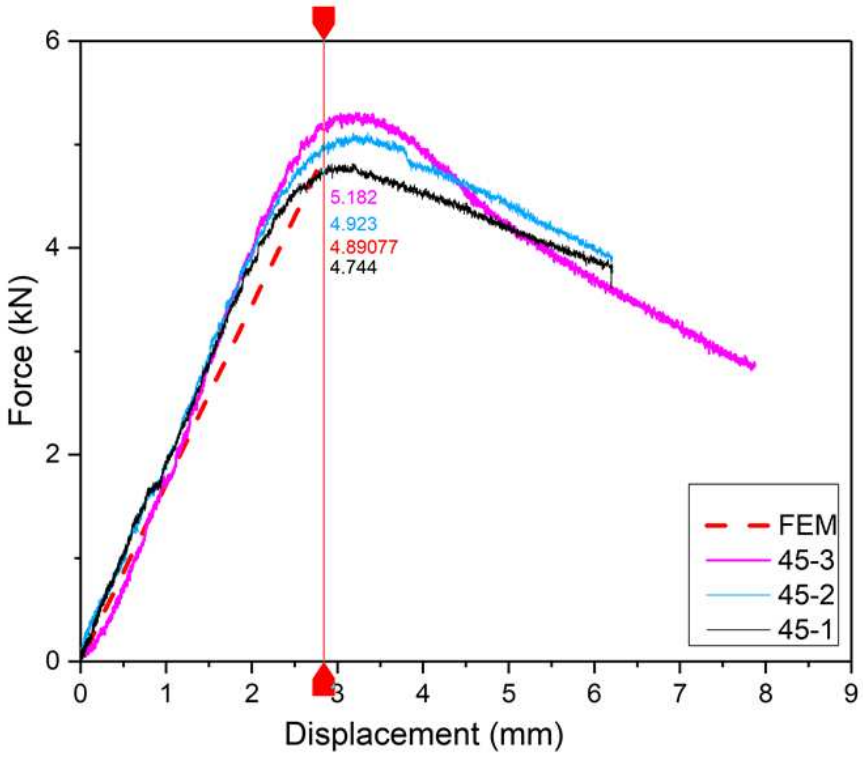

(a)

(b)

(c)

Figure 7.12 a) Force-displacement graph of $[\pm 45]_6$ wound rods, b) Before the test, and c) after the test.

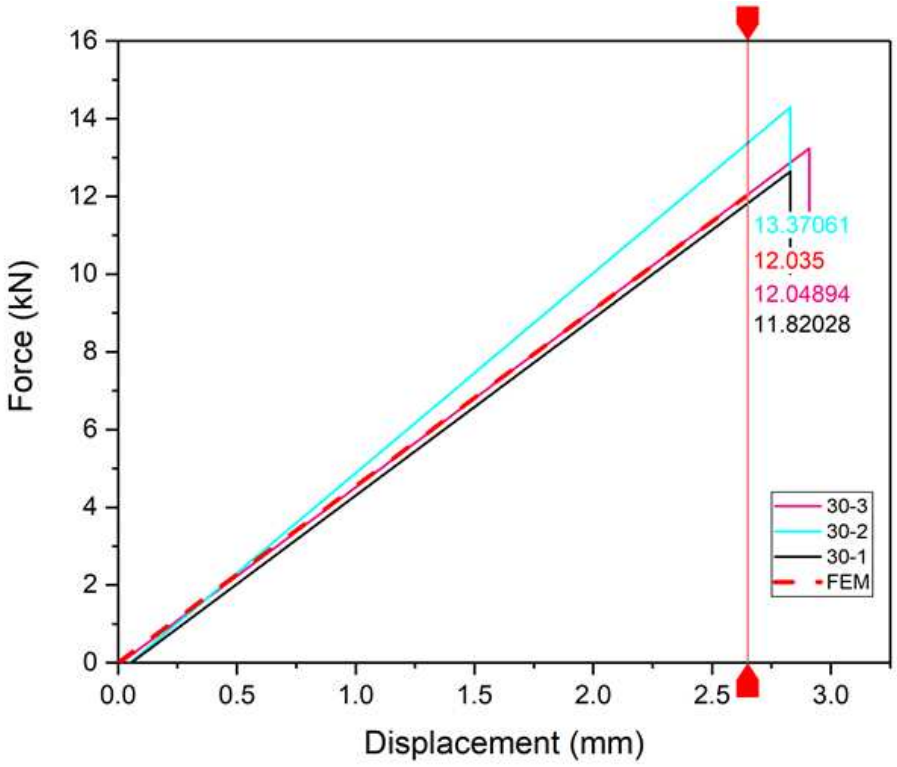

(a)

(b)

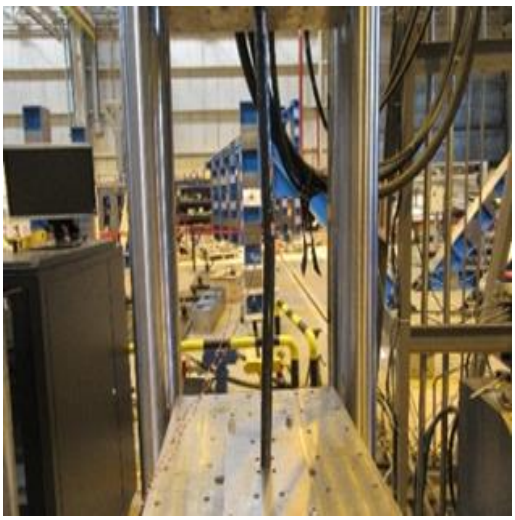

(c)

Figure 7.13 a) Force-displacement graph of $[\pm 30]_6$ wound rods, b) Before the test, and c) after the test.

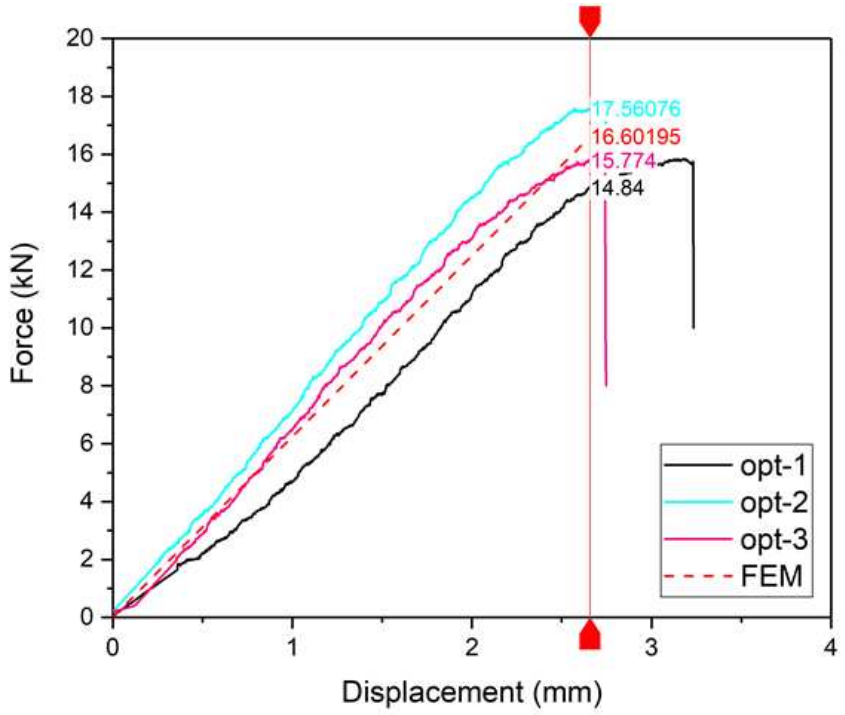

(a)

(b)

(c)

Figure 7.14 a) Force-displacement graph of optimum wound rods, b) Before the test, and c) after the test.

This relative anomaly observed in the 1st specimen was due to the fact that the type and end of the fixing plate and the rods were not fully aligned at the beginning of the test and therefore the loading and displacement profile changed relatively. In conclusion, the convincing agreement between FEM and experimental data confirms the accuracy of the model in predicting the buckling behavior.

In conclusion, the average buckling loads for $[\pm45]_6$, $[\pm30]_6$ and optimum design CFRP rods were 4.94 kN, 12.41 kN and 16.058 kN, respectively. The $[\pm45]_6$ specimens, characterized by their relatively low axial stiffness, showed lower axial load carrying capacity as expected. This relatively low performance is attributed to the stacking sequence which, while offering enhanced circumferential stiffness, resulted in a higher displacement capacity prior to failure rather than experiencing an abrupt failure. In contrast, optimum design rods designed to meet the various calculation criteria summarized in Table 7.3 showed superior buckling performance. In particular, optimum design rods exhibited a buckling load capacity 3.25 times greater than that of $[\pm45]_6$ rods and 1.3 times greater than that of $[\pm30]_6$ rods. Moreover, the linear buckling finite element model (Eigenvalue buckling analysis) results were consistent with the experimental data with a margin of error less than 4% for all three specimen groups. This reasonably good agreement highlights the reliability and accuracy of the finite element model in predicting the buckling behavior of these composite rods. Buckling values calculated with smeared property showed a deviation of 6.25%, 3.91% and 9.66% respectively. The results, which are in parallel with the reports shared in the literature[72,73], have provided meaningful results for the preliminary design input.

Additionally, in order to compare results of experimental, FEM and analytical solutions results are listed as shown in Table 7.4 and Knock-down Factors (KDF) are also calculated.

Table 7.4 Knock-down Factor calculation

Stack. Seq.	**Exp.**	**FEM**	**ANALY.**	**% Diff. FEM**	**% Diff. ANALY.**	**% Analy. Diff. w.r.t FEM**
$[\pm45_6]_{FW}$	4.94	5.00	5.25	1.21%	6.25%	4.98%
$[\pm30_6]_{FW}$	12.41	12.48	12.89	0.56%	3.91%	3.32%
Optimum Design	16.05	16.60	17.60	3.43%	9.66%	6.03%

As mentioned in Chapter 7.2, axial shortening and circumferential displacement were measured using a T-rosette strain gauge positioned at the center point of the CFRP rods. The results are illustrated in Figure 7.15.

As shown in Figure 7.15, balanced but nonsymmetrical stacking sequences, such as $[\pm45]_6$ and $[\pm30]_6$ (B_{ij}=0, except B_{16} and B_{26} tension-twisting coupling), exhibited identical behavior in terms of shortening and radial displacement.

On the other hand, laminates like the optimum design are balanced but nonsymmetric and tend to bend, twist, and/or warp under applied loads and moments (B_{ij} ≠0). Thus, results of optimum design rods showed nonlinear behavior. A noticeable change in slope occurs when the load surpasses the 14 kN threshold. The inner wall of a rod is pressured when it buckles under uniaxial compressive stresses because the wall of the rod bends. The outer wall, on the other hand, is subjected to tension.[115] Therefore, the non-linearity can be explained by the fact that the fibers layup at 20 and 30 degrees through 6 plies due to load type and carrying capacity differences.

Additionally, as an example mode 1 linear buckling failure at the center point where the gauge was applied can be seen in Figure 7.16.

7.5. Acid Digestion Results

As mentioned in 3.3.2.1, ASTM 3171 was utilized to determine the constituents of composite materials according to the given standard. After the epoxy was completely removed, the fibers were dried and the volumetric fiber ratio was computed using equations (3.5) and (3.6). A bar graph of the results is shown in Figure 7.17.

The average fiber volume fractions of non-optimized samples, $[\pm30]_6$ and $[\pm45]_6$ were calculated as %67.95±1.12, and %66.67±0.66 respectively. The volumetric fiber content of the non-optimized rods was calculated to be about 70%, which can be ascribed to the absence of pattern variation and the presence of tension during winding.[116] Conversely, the fiber volume fraction in the optimum design is slightly less than that of the non-optimized samples, and the average fiber volume fraction of optimized samples was computed as %63.01±0.95. The fact that different ply angle orientations can yield resin-rich regions between fibers can be attributed to different winding patterns (see Table 7.3).

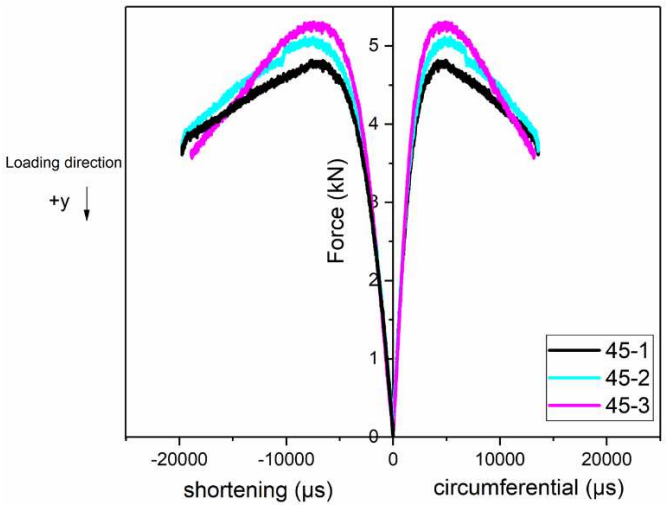

(a)

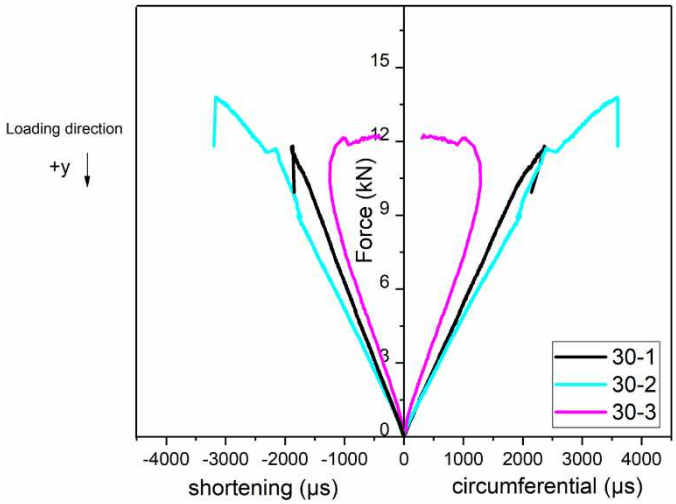

(b)

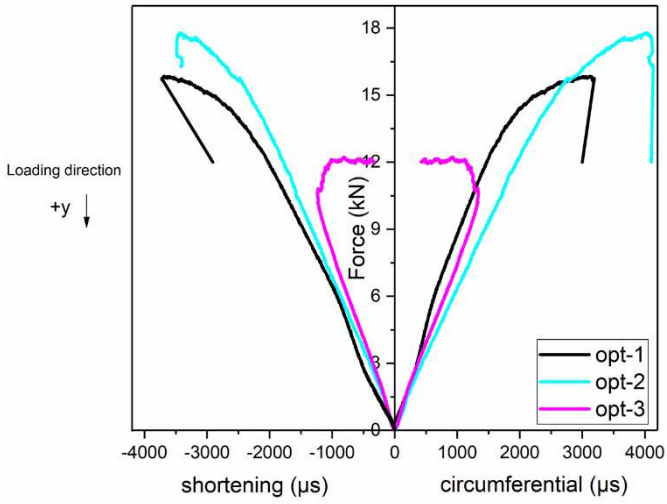

(c)

Figure 7.15 Axial and circumferential displacement obtained by means of strain gauge a) $[\pm 45]_6$, b)$[\pm 30]_6$, and c)DESIGN-1

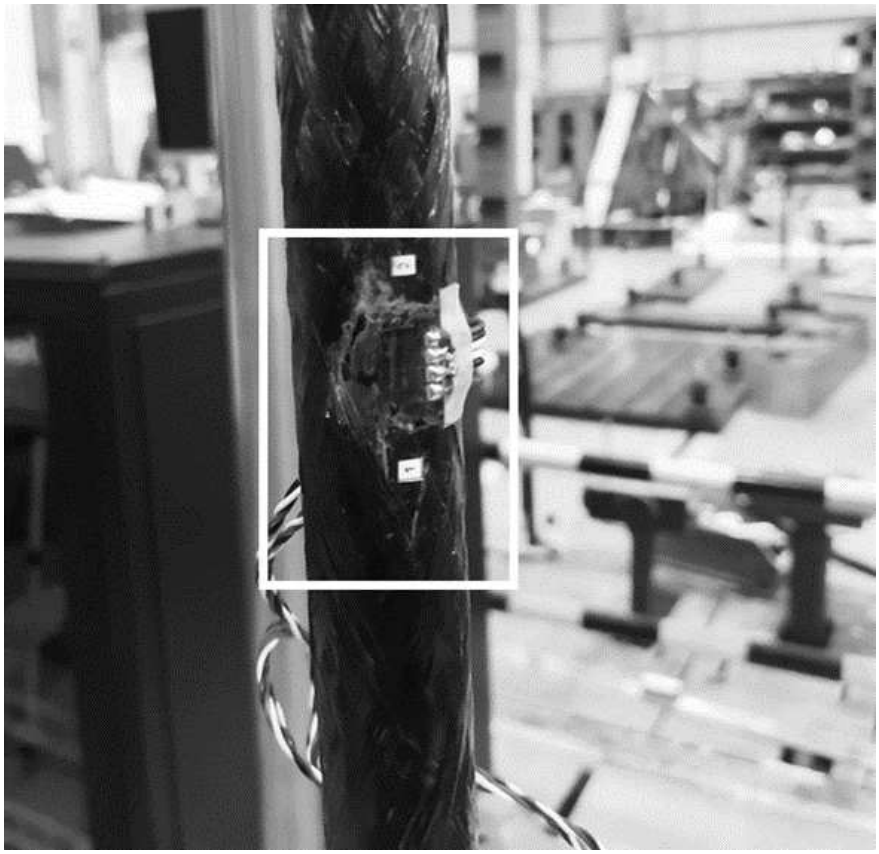

(a)

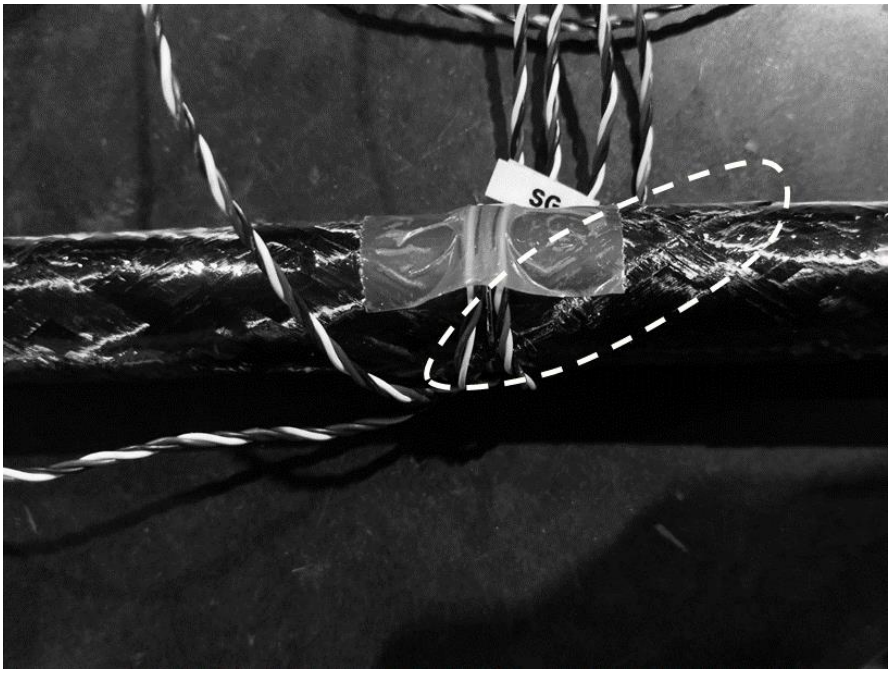

(b)

Figure 7.16 An example mode 1 linear buckling failure of the CFRP rod under the axial loading a) after the test b) detailed photo regarding fiber failure

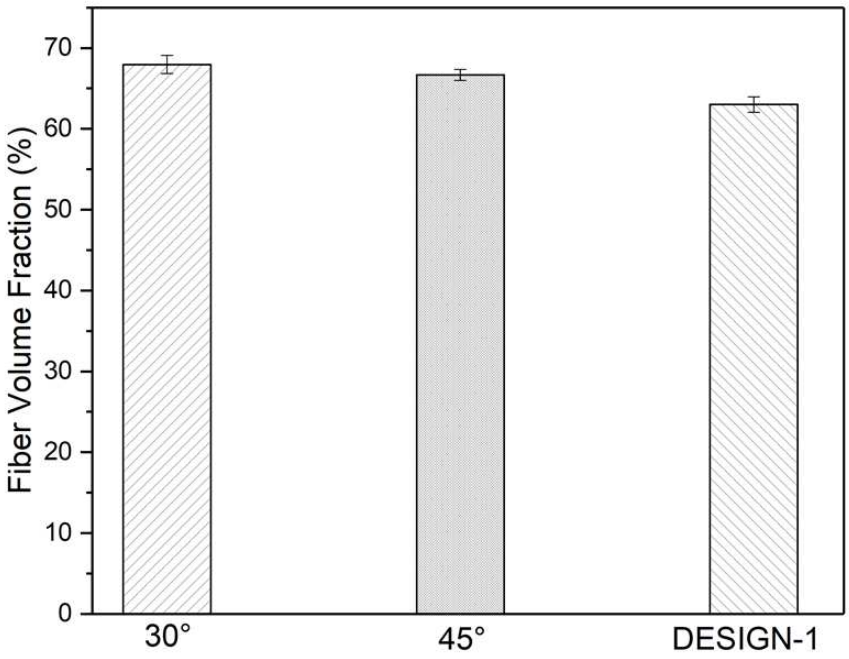

Figure 7.17 Fiber volume fraction of reference and optimum design samples.

7.6. Microstructural Investigation

In this chapter, optical (7.6.1) and SEM (7.6.2) findings of the produced non-optimized and optimized CFRP rods are presented.

7.6.1. Optical Microscopy Results

Cutting, grinding, and polishing operations were meticulously applied to the cross-section of the specimens to investigate the microstructure of both optimized and non-optimized CFRP rods. These preliminary steps ensured adequately flat surfaces suitable for in-depth microscopic examination. Figure 7.18 shows the optical microstructure images of the 30, 45 and optimum samples, respectively, obtained as a result of this analysis.

The microstructure images show that the specimens oriented at 30° and 45° have no significant defects or voids when examined at the same magnification. This indicates that the reinforcing fibers are evenly distributed and the matrix quality is unchanged in the non-optimized designs. However, the microstructure of the optimized CFRP rod revealed a significant resin-rich region.

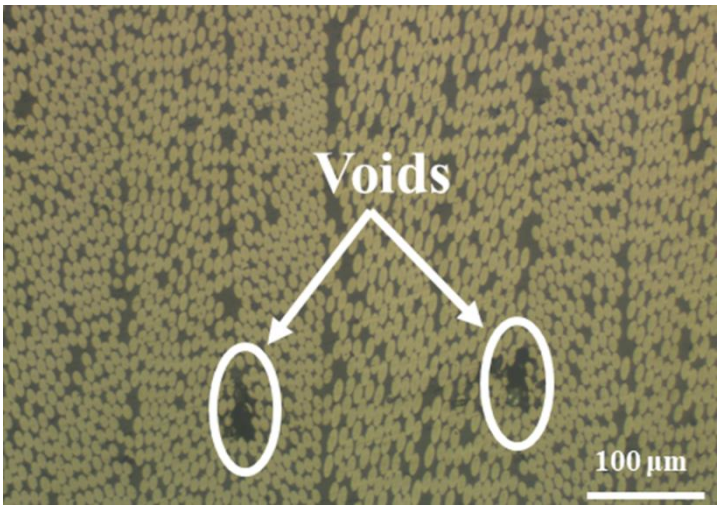

(a)

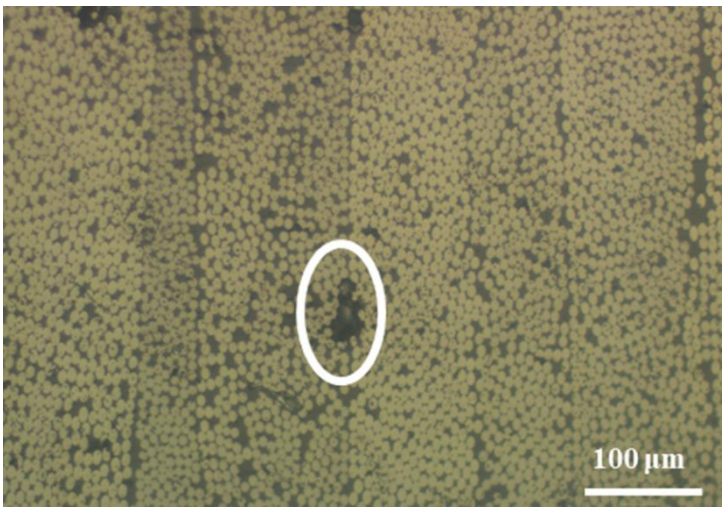

(b)

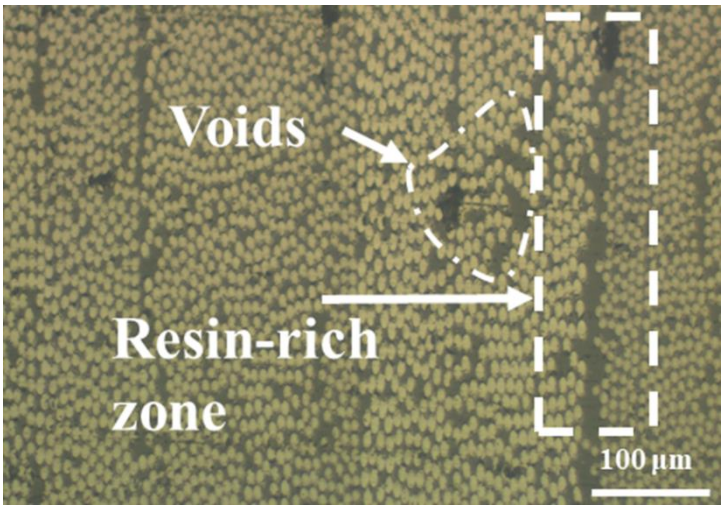

(c)

Figure 7.18 Microstructural investigation of a) 30°, b) 45°, and c) optimum design rod by means of optical microscopy

The part where the resin concentration in the studied cross section is higher than the fiber concentration is thought to be due to the variation of the winding pattern between the layers created by the optimization procedure, resulting in the formation of resin-rich voids.

The findings are in agreement with the results of the acid digestion process discussed earlier. It is shown in the acid digestion plot (see Figure 7.17) that compared to the non-optimized samples, the optimized design contains relatively less reinforcing material by volume. This is confirmed by the presence of resin-rich regions, indicating that areas of the composite with significantly higher resin content may result from the optimization process. Understanding the impact of design changes on the microstructural integrity and overall performance of CFRP rods is the crucial finding.

7.6.2. Scanning Electron Microscopy Results

The samples prepared to be examined under an optical microscope were also examined under a scanning electron microscope. As mentioned in section 0, the microstructure was investigated in backscatter mode with the Quanta 250 SEM device within IZTECH.

During CFRP rod production with filament winding, repetitive patterns are formed on the surface depending on the winding pattern. As shown in Figure 7.19 (a) the fiber, during winding, passes over the previous fiber to form undulation. Depending on where the specimen is cut, this phenomenon can also be observed in the microstructure examination. In Figure 7.19 (b), the yellow and gray colored areas show the undulation detected.

On the other hand, due to the nature of filament winding, there are + - theta angle changes between the passages. The reflection of this in the microstructure is also shown in Figure 7.20.

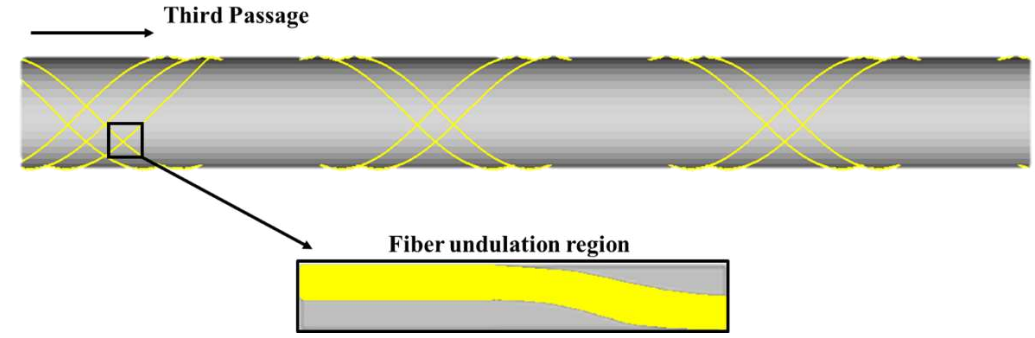

(a)

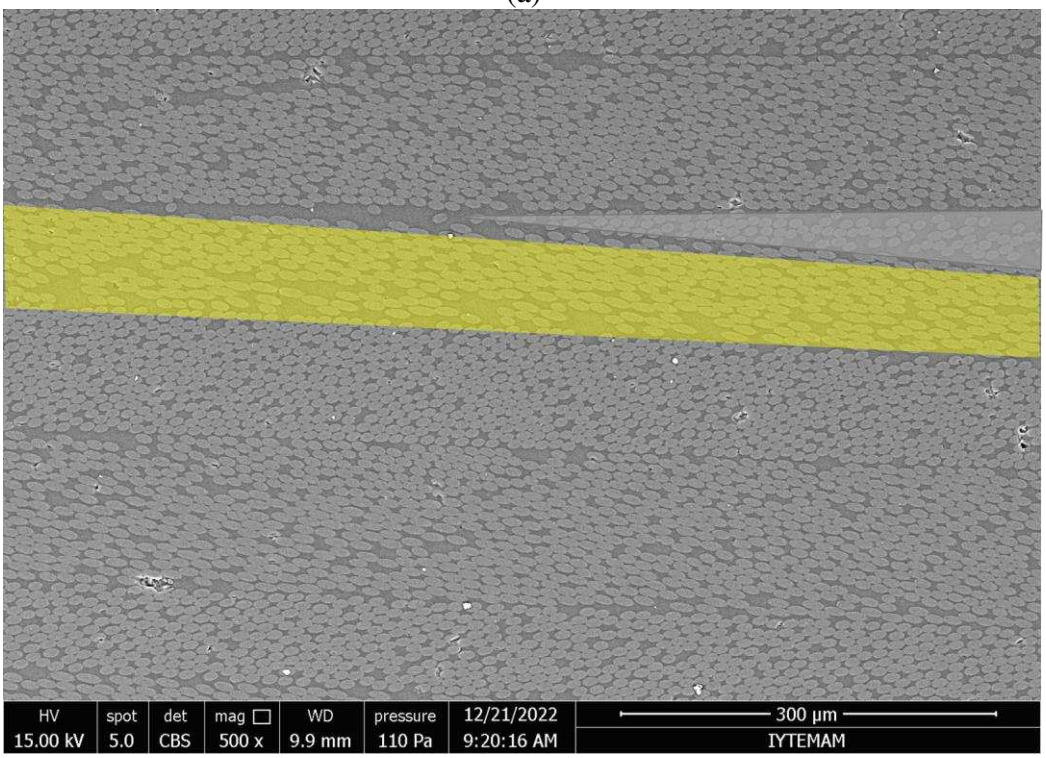

(b)

Figure 7.19 Fiber undulation representation (a) schematic drawing, and (b) SEM images of fiber undulation at the start

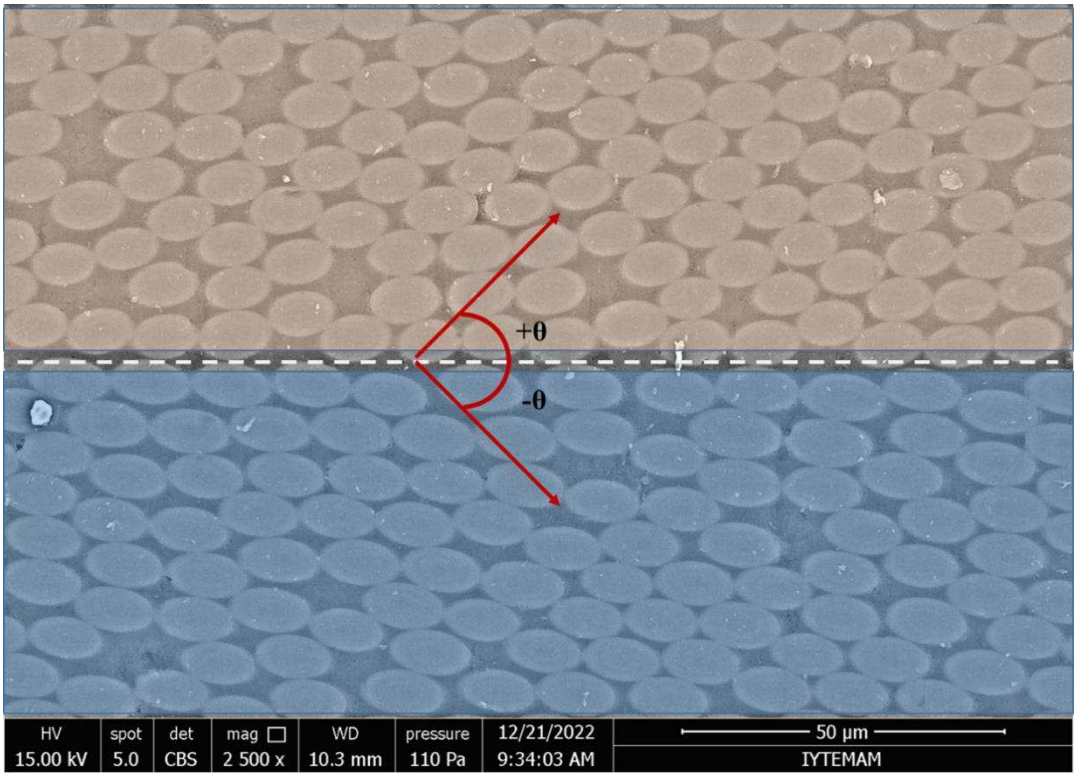

Figure 7.20 Illustration of angle variation between passages

CHAPTER 8

CONCLUSIONS

This thesis presents a comprehensive investigation that covers the design, finite element modeling, optimization, fabrication, and experimental testing of carbon fiber reinforced polymers (CFRP) characterized by considerable thickness (with a ratio of radius to thickness approximately 7). The study was specifically focused on addressing the vulnerability of these CFRP rods to buckling damage when subjected to axial loading. Through filament winding techniques, the manufacturing process was detailed, aiming to increase structural integrity and reduce buckling risks in CFRP components by using GA optimization.

According to the optimization results, among other possible stacking sequences, $[\pm 30_3/\pm 20_3]$ provided relatively the best stiffness and manufacturability results. Apart from the optimization results, axial and bending stiffness were calculated by using MATLAB, and $[\pm 30_3/\pm 20_3]$ was a promising candidate for delivering the desired stiffness behavior ($(A_{11}/A_{22} >> 1\ D_{11}/D_{22} >> 1)$. The produced rods were subjected to component-level buckling tests, and the rods with $[\pm 30_3/\pm 20_3]$ stacking sequence exhibited 1.3 times better buckling performance than $[\pm 30]_6$ and 3.25 times better buckling performance than $[\pm 45]_6$. Further, The FEM provided consistent results in determining the buckling loads with a margin of error of less than 4% for each group of specimens. For a conservative approach, the critical buckling load can be determined with 0.95 KDF based on the finite element result.

When compared with the analytical solution approach test results, a maximum deviation of 9.7% was detected. the smeared property approach converges to the experimental and finite element method with a KDF of 0.9, and it suits the referenced table in the literature (see Figure 5.1). The difference can be attributed to the fact that not consider the B matrix during the smeared property approach.

In addition to the monitoring of the load-displacement controlled buckling test, axial shortening and radial displacement strain values were monitored by T-rosette strain gauge. It was found that while non-optimized specimens exhibited relatively symmetrical behavior in axial and radial directions, optimum design specimens exhibited non-linear

behavior after exceeding the threshold value of 14 kN. It can be interpreted that this situation is due to coupling effects as it does not have a symmetrical lay-up ($B_{ij}\neq0$).

Based on acid digestion, fiber volume fraction (%) of 30°, 45°, and optimum design CFRP rod results were calculated as 67.9, 66.5, and 63 respectively. Considering the results of the optical microscope examination, the presence of slightly resin-rich regions observed in the microstructural analysis of optimum design specimens, and hence it supports the fact that it contains relatively fewer fibers than the non-optimized samples.

Overall, considering that conventional rods are typically made of aluminum (density: ~ 2.7 g/cm^3) or steel (density: ~ 7.8 g/cm^3), CFRP rods (~1.7 g/cm^3) optimized for specific applications can potentially achieve a significant reduction in structural mass of 50% without compromising stiffness or other critical design parameters.

8.1. Future Studies

In this study, CFRP rods resistant to buckling damage were produced by filament winding method in accordance with the desired design criteria. Both finite element model and analytical model of the produced rods were established and compared with the experimental data, it was seen that it can provide inputs for preliminary design and final design and contribute to the literature. In addition, for future studies:

- Design criteria (natural frequency and angular torsion) can be tested and compared with the finite element and analytical model.
- To determine the material allowable of the carbon and polymer matrix used, A-basis, B-basis allowable must be created by subjecting the missing dry focus temperature (RTD), cold temperature dry (CTD) and elevated temperature wet (ETW) conditions.
- In this study, the diameter and thickness were not changed, but thinner and lighter rods of different diameters can be obtained to meet the desired criteria.
- Conducting fatigue tests to test its performance under repetitive loads for use in aircraft
- For use as a push-pull rod, it can be converted into a final product by designing the connecting elements of the rod and performing other tests including adhesive modeling between connecting element and CFRP rods.

REFERENCES

1. Valery V. Vasiliev, E. V. M. *Advanced Mechanics of Composite Materials and Structures*, 4th ed.; Matthew Deans, 2018. https://doi.org/DOI: https://doi.org/10.1016/B978-0-08-102209-2.00001-3.

2. Kaw, A. K. *Mechanics of Composite Materials*, 2nd ed.; Taylor & Francis Group, 2005. https://doi.org/https://doi.org/10.1201/9781420058291.

3. Harris, C. E.; Starnes, J. H.; Shuart, M. J. Design and Manufacturing of Aerospace Composite Structures, State-of-the-Art Assessment. *J. Aircr.* **2002**, *39* (4), 545–560. https://doi.org/10.2514/2.2992.

4. Krishan K. Chawla. *Composite Materials*; 2019. https://doi.org/doi.org/10.1007/978-3-030-28983-6.

5. *Composite Materials Handbook Volume 3*; SAE International, 2012; Vol. 3.

6. Werfelman, L. The Composite Evolution. **2007**, No. March, 17–21.

7. Smith, F. The Use of Composites in Aerospace: Past, Present and Future Challenges. *Avalon Consult. Serv. LTD* **2013**, 1–40.

8. Messinger, R. Design of Structurally Efficient Tapered Struts. **2010**, No. May.

9. No Title https://www.avio.com/ (accessed 2024 -05 -31).

10. E., B. *Introduction to Composite Materials Design by Ever J. Barbero*; 2017.

11. CLYNE, T. W.; Hull D. *An Introduction to Composite Materials*, 3rd ed.; Cambridge University Press, 2019. https://doi.org/10.1017/9781139050586.

12. Campbell, F. C. *Structural Composite Materials*; 2010. https://doi.org/10.31399/asm.tb.scm.9781627083140.

13. Chung, D. D. L. *Composite Materials*, 2nd ed.; Springer London, 2010. https://doi.org/10.1007/978-1-84882-831-5.

14. Martin, S.; Kandemir, S.; Antonov, M. Investigation of the High Temperature Dry Sliding Wear Behavior of Graphene Nanoplatelets Reinforced Aluminum Matrix Composites. *J. Compos. Mater.* **2021**, *55* (13), 1769–1782. https://doi.org/10.1177/0021998320979037.

15. Pemberton, S. R.; Oberg, E. K.; Dean, J.; Tsarouchas, D.; Markaki, A. E.; Marston, L.; Clyne, T. W. The Fracture Energy of Metal Fibre Reinforced Ceramic Composites (MFCs). *Compos. Sci. Technol.* **2011**, *71* (3), 266–275. https://doi.org/10.1016/j.compscitech.2010.10.011.

16. Krenkel, W.; Reichert, F. *Design Objectives and Design Philosophies, Interphases and Interfaces in Fiber-Reinforced CMCs*; Elsevier Ltd., 2017; Vol. 5. https://doi.org/10.1016/B978-0-12-803581-8.09986-0.

17. Cherrington, R.; Goodship, V.; Liang, J.; Middleton, B.; Wood, B. M. *Design and Manufacture of Plastic Components for Multifunctionality*; 2018. https://doi.org/10.1016/c2014-0-00223-7.

18. Mallick, P. K. *Fiber-Reinforced Composites*; 3, Ed.; CRC Press, 2007. https://doi.org/10.1201/9781420005981.

19. Long, A. C. *Design and Manufacture of Textile Composites*, 1st ed.; Wood Head Publishing Limited, 2005.

20. Peters, S. T. *Composite Filament Winding*; Peters, S. T., Ed.; ASM International, 2011.

21. Dow, N. F.; Rosen, B. W. Structural Efficiency of Orthotropic Cylindrical Shells Subjected to Axial Compression. *AIAA J.* **1966**, *4* (3), 481–485. https://doi.org/10.2514/3.3461.

22. Gürdal, Z.; Olmedo, R. In-Plane Response of Laminates with Spatially Varying Fiber Orientations: Variable Stiffness Concept. *AIAA J.* **1993**, *31* (4), 751–758. https://doi.org/10.2514/3.11613.

23. Henriquez, R. G.; Mertiny, P. *Filament Winding Applications*; Elsevier Ltd., 2017; Vol. 3. https://doi.org/10.1016/B978-0-12-803581-8.10313-3.

24. Colombo, C.; Vergani, L. Optimization of Filament Winding Parameters for the Design of a Composite Pipe. *Compos. Part B Eng.* **2018**, *148* (April), 207–216. https://doi.org/10.1016/j.compositesb.2018.04.056.

25. Manoj Prabhakar, M.; Rajini, N.; Ayrilmis, N.; Mayandi, K.; Siengchin, S.; Senthilkumar, K.; Karthikeyan, S.; Ismail, S. O. An Overview of Burst, Buckling, Durability and Corrosion Analysis of Lightweight FRP Composite Pipes and Their Applicability. *Compos. Struct.* **2019**, *230* (January), 111419. https://doi.org/10.1016/j.compstruct.2019.111419.

26. Almeida, J. H. S.; St-Pierre, L.; Wang, Z.; Ribeiro, M. L.; Tita, V.; Amico, S. C.; Castro, S. G. P. Design, Modeling, Optimization, Manufacturing and Testing of Variable-Angle Filament-Wound Cylinders. *Compos. Part B Eng.* **2021**, *225* (July), 109224. https://doi.org/10.1016/j.compositesb.2021.109224.

27. Almeida, J. H. S.; St-Pierre, L.; Wang, Z.; Ribeiro, M. L.; Tita, V.; Amico, S. C.; Castro, S. G. P. Design, Modeling, Optimization, Manufacturing and Testing of Variable-Angle Filament-Wound Cylinders. *Compos. Part B Eng.* **2021**, *225* (August), 109224. https://doi.org/10.1016/j.compositesb.2021.109224.

28. Cui, Z.; Liu, Q.; Sun, Y.; Li, Q. On Crushing Responses of Filament Winding CFRP/Aluminum and GFRP/CFRP/Aluminum Hybrid Structures. *Compos. Part B Eng.* **2020**, *200* (August), 108341. https://doi.org/10.1016/j.compositesb.2020.108341.

29. Perillo, G.; Grytten, F.; Sørbø, S.; Delhaye, V. Numerical/Experimental Impact Events on Filament Wound Composite Pressure Vessel. *Compos. Part B Eng.* **2015**, *69*, 406–417. https://doi.org/10.1016/j.compositesb.2014.10.030.

30. Huang, Z.; Qian, X.; Su, Z.; Pham, D. C.; Sridhar, N. Experimental Investigation and Damage Simulation of Large-Scaled Filament Wound Composite Pipes. *Compos. Part B Eng.* **2020**, *184* (December 2019), 107639. https://doi.org/10.1016/j.compositesb.2019.107639.

31. Wang, Q.; Li, T.; Wang, B.; Liu, C.; Huang, Q.; Ren, M. Prediction of Void Growth and Fiber Volume Fraction Based on Filament Winding Process Mechanics. *Compos. Struct.* **2020**, *246* (April), 112432. https://doi.org/10.1016/j.compstruct.2020.112432.

32. Zu, L.; Koussios, S.; Beukers, A. Design of Filament-Wound Domes Based on Continuum Theory and Non-Geodesic Roving Trajectories. *Compos. Part A Appl. Sci. Manuf.* **2010**, *41* (9), 1312–1320. https://doi.org/10.1016/j.compositesa.2010.05.015.

33. Schultz, M. R.; Nemeth, M. P. Buckling Imperfection Sensitivity of Axially Compressed Orthotropic Cylinders. *Collect. Tech. Pap. - AIAA/ASME/ASCE/AHS/ASC Struct. Struct. Dyn. Mater. Conf.* **2010**. https://doi.org/10.2514/6.2010-2531.

34. Haim Abramovich. *Stability and Vibrations of Thin-Walled Composite Structures*, 1st ed.; Wood Head Publishing, 2017; Vol. 6.

35. Dalibor, I. H.; Lisbôa, T. V.; Marczak, R. J.; Amico, S. C. A Geometric Approach for Filament Winding Pattern Generation and Study of the Influence of the Slippage Coefficient. *J. Brazilian Soc. Mech. Sci. Eng.* **2019**, *41* (12), 1–16. https://doi.org/10.1007/s40430-019-2083-2.

36. Kubiak, T.; Kolakowski, Z.; Swiniarski, J.; Urbaniak, M.; Gliszczynski, A. Local Buckling and Post-Buckling of Composite Channel-Section Beams - Numerical and Experimental Investigations. *Compos. Part B Eng.* **2016**, *91*, 176–188. https://doi.org/10.1016/j.compositesb.2016.01.053.

37. Eggers, F.; Almeida, J. H. S.; Azevedo, C. B.; Amico, S. C. Mechanical Response of Filament Wound Composite Rings under Tension and Compression. *Polym. Test.* **2019**, *78* (June), 105951. https://doi.org/10.1016/j.polymertesting.2019.105951.

38. Zhang, Z.; Hou, S.; Liu, Q.; Han, X. Winding Orientation Optimization Design of Composite Tubes Based on Quasi-Static and Dynamic Experiments. *Thin-Walled Struct.* **2018**, *127* (June 2017), 425–433. https://doi.org/10.1016/j.tws.2017.11.052.

39. Soden, P. D.; Leadbetter, D.; Griggs, P. R.; Eckold, G. C. The Strength of a Filament Wound Composite under Biaxial Loading. *Composites* **1978**, *9* (4), 247–250. https://doi.org/10.1016/0010-4361(78)90177-5.

40. Sessa, S.; Serpieri, R.; Rosati, L. A Continuum Theory of through–the–Thickness Jacketed Shells for the Elasto-Plastic Analysis of Confined Composite Structures: Theory and Numerical Assessment. *Compos. Part B Eng.* **2017**, *113*, 225–242. https://doi.org/10.1016/j.compositesb.2017.01.011.

41. Castro, S. G. P.; Mittelstedt, C.; Monteiro, F. A. C.; Arbelo, M. A.; Ziegmann, G.; Degenhardt, R. Linear Buckling Predictions of Unstiffened Laminated Composite Cylinders and Cones under Various Loading and Boundary Conditions Using Semi-Analytical Models. *Compos. Struct.* **2014**, *118* (1), 303–315. https://doi.org/10.1016/j.compstruct.2014.07.037.

42. Degenhardt, R.; Castro, S. G. P.; Arbelo, M. A.; Zimmerman, R.; Khakimova, R.; Kling, A. Future Structural Stability Design for Composite Space and Airframe Structures. *Thin-Walled Struct.* **2014**, *81*, 29–38. https://doi.org/10.1016/j.tws.2014.02.020.

43. Haynie, W. T.; Hilburger, M. W. Comparison of Methods to Predict Lower Bound Buckling Loads of Cylinders under Axial Compression. *Collect. Tech. Pap. - AIAA/ASME/ASCE/AHS/ASC Struct. Struct. Dyn. Mater. Conf.* **2010**, No. April. https://doi.org/10.2514/6.2010-2532.

44. Chauncey Wu, K.; Phelps, J. E.; McKenney, M. J.; Jegley, D. C. Highly Loaded Composite Strut Test Development. *Collect. Tech. Pap. - AIAA/ASME/ASCE/AHS/ASC Struct. Struct. Dyn. Mater. Conf.* **2011**, 1–17. https://doi.org/10.2514/6.2011-1787.

45. Jegley, D. C.; Wu, K. C.; Phelps, J. E.; McKenney, M. J.; Oremont, L.; Barnard, A. Evaluation of Long Composite Struts. **2011**, No. February.

46. White, S. C.; Weaver, P. M.; Wu, K. C. Post-Buckling Analyses of Variable-Stiffness Composite Cylinders in Axial Compression. *Compos. Struct.* **2015**, *123*, 190–203. https://doi.org/10.1016/j.compstruct.2014.12.013.

47. Xing, J.; Geng, P.; Yang, T. Stress and Deformation of Multiple Winding Angle Hybrid Filament-Wound Thick Cylinder under Axial Loading and Internal and External Pressure. *Compos. Struct.* **2015**, *131*, 868–877. https://doi.org/10.1016/j.compstruct.2015.05.036.

48. Lemanski, S.; Weaver, P. Optimisation of a 4-Layer Laminated Cylindrical Shell to Meet given Cross-Sectional Stiffness Properties. *Compos. Struct.* **2006**, *72* (2), 163–176. https://doi.org/10.1016/j.compstruct.2004.11.005.

49. Wei, R.; Pan, G.; Jiang, J.; Shen, K. Influence of Ply Angle and Length on Buckling .Behavior of Composite Shells under Hydrostatic Pressure. *J. Reinf. Plast. Compos.* **2019**, *38* (10), 478–491. https://doi.org/10.1177/0731684419828183.

50. Wagner, H. N. R.; Köke, H.; Dähne, S.; Niemann, S.; Hühne, C.; Khakimova, R. Decision Tree-Based Machine Learning to Optimize the Laminate Stacking of Composite Cylinders for Maximum Buckling Load and Minimum Imperfection Sensitivity. *Composite Structures*. Elsevier 2019, pp 45–63. https://doi.org/10.1016/j.compstruct.2019.02.103.

51. Imran, M.; Shi, D.; Tong, L.; Waqas, H. M. Design Optimization of Composite Submerged Cylindrical Pressure Hull Using Genetic Algorithm and Finite Element Analysis. *Ocean Eng.* **2019**, *190* (145), 106443. https://doi.org/10.1016/j.oceaneng.2019.106443.

52. Abu Talib, A. R.; Ali, A.; Badie, M. A.; Azida Che Lah, N.; Golestaneh, A. F. Developing a Hybrid, Carbon/Glass Fiber-Reinforced, Epoxy Composite Automotive Drive Shaft. *Mater. Des.* **2010**, *31* (1), 514–521. https://doi.org/10.1016/j.matdes.2009.06.015.

53. Wei, R.; Pan, G.; Jiang, J.; Shen, K.; Lyu, D. An Efficient Approach for Stacking Sequence Optimization of Symmetrical Laminated Composite Cylindrical Shells Based on a Genetic Algorithm. *Thin-Walled Struct.* **2019**, *142* (September 2018), 160–170. https://doi.org/10.1016/j.tws.2019.05.010.

54. Bilalis, E. P.; Keramidis, M. S.; Tsouvalis, N. G. Structural Design Optimization of Composite Materials Drive Shafts. *Mar. Struct.* **2022**, *84* (June 2021), 103194. https://doi.org/10.1016/j.marstruc.2022.103194.

55. Wang, Z.; Almeida, J. H. S.; St-Pierre, L.; Wang, Z.; Castro, S. G. P. Reliability-Based Buckling Optimization with an Accelerated Kriging Metamodel for Filament-Wound Variable Angle Tow Composite Cylinders. *Compos. Struct.* **2020**, *254* (August), 112821. https://doi.org/10.1016/j.compstruct.2020.112821.

56. Ochelski, S.; Gotowicki, P. Experimental Assessment of Energy Absorption Capability of Carbon-Epoxy and Glass-Epoxy Composites. *Compos. Struct.* **2009**, *87* (3), 215–224. https://doi.org/10.1016/j.compstruct.2008.01.010.

57. Kim, J. S.; Yoon, H. J.; Shin, K. B. A Study on Crushing Behaviors of Composite Circular Tubes with Different Reinforcing Fibers. *Int. J. Impact Eng.* **2011**, *38* (4), 198–207. https://doi.org/10.1016/j.ijimpeng.2010.11.007.

58. Badie, M. A.; Mahdi, E.; Hamouda, A. M. S. An Investigation into Hybrid Carbon/Glass Fiber Reinforced Epoxy Composite Automotive Drive Shaft. *Mater. Des.* **2011**, *32* (3), 1485–1500. https://doi.org/10.1016/j.matdes.2010.08.042.

59. Jegley, D. C.; Wu, K. C.; Phelps, J. E.; McKenney, M. J.; Oremon, L.; Supports, C. R. Y. O. G. E. N. I. C. T. Structural Efficiency of Composite Struts for Aerospace Applications. *J. Spacecr. Rockets* **2012**, *49* (5), 915–924. https://doi.org/10.2514/1.60053.

60. Modlin, C. T.; Zipay, J. J. For Aircraft & Spacecraft – History , Definition and Applications. **2014**, 1–26.

61. Almeida, J. H. S.; Tonatto, M. L. P.; Ribeiro, M. L.; Tita, V.; Amico, S. C. Buckling and Post-Buckling of Filament Wound Composite Tubes under Axial Compression: Linear, Nonlinear, Damage and Experimental Analyses. *Compos. Part B Eng.* **2018**, *149* (April), 227–239. https://doi.org/10.1016/j.compositesb.2018.05.004.

62. ASTM D3039 - Standard Test Method for Tensile Properties of Polymer Matrix Composite Materials.

63. ASTM - D6641 Standard Test Method for Compressive Properties of Polymer Matrix Composite Materials Using a Combined Loading Compression (CLC) Test Fixture.

64. D-5379-Standard Test Method for Shear Properties of Composite Materials by the V-Notched Beam Method.

65. CADWIND V9 User Manual.

66. ASTM. ASTM D3171 Standard Test Methods for Constituent Content of Composite Materials. *ASTM Standard*. 2011, pp 1–10.

67. Analysis, M. Leica DM2500 M Microscope for Material Analysis.

68. Vinson, J. R. *Plate and Panel Structures of Isotropic, Composite and Piezoelectric Materials, Including Sandwich Construction*, 1st ed.; Springer Dordrecht, 2005; Vol. 6. https://doi.org/https://doi.org/10.1007/1-4020-3111-4.

69. Vinson, J. R.; Sierakowski, R. L. *The Behavior of Structures Composed of Composite Materials SOLID MECHANICS AND ITS APPLICATIONS*; 2002; Vol. 105.

70. Nettles, A. T. Basic Mechanics of Laminated Composite Plates. *NASA Ref. pulication* **1994**, No. October, 107.

71. Reddy, J. N. *Book Mechanics of Laminated Composite Plates and Shells*, 2nd ed.; CRC Press, 2003. https://doi.org/https://doi.org/10.1201/b12409.

72. Fan SR, Geier B, Rohwer K, L. D. Stability of a Layered Anisotropic Cylindrical Shells under Combined Loading. *Z Flugweiss Weltraumforsch* **1983**, *7* (5). https://doi.org/10.1016/j.oceaneng.2021.108633.

73. Lin, C. Y.; Chan, W. S. Stiffness Evaluation of Elliptical Laminated Composite Tube under Bending. *19th AIAA Appl. Aerodyn. Conf.* **2001**, No. c, 1–6. https://doi.org/10.2514/6.2001-1336.

74. David P. Maass. Tubular Composite Compression Members - Design Considerations and Practices. *J. Reinf. Plast. Compos.* **1987**, *6* (4). https://doi.org/https://doi.org/10.1177/073168448700600403.

75. Peterson, J. P.; Weingarten, V. I.; Seide, P. NASA SP-8007 Bucking of Thin Walled .Circular Cylinders. **1968**, No. August, 60.

76. Peterson, J. P. Structural Efficiency of Ring-Stiffened Corrugated Cylinders in Axial Compression. **1967**, No. August.

77. NASA. Buckling Strength of Structural Plates (NASA-SP-8068). **1971**, No. June.

78. Hilburger, M. W. Buckling of Thin-Walled Circular Cylinders. *Nasa/Sp-8007-2020/Rev 2* **2020**, No. August 1968, 1–60.

79. Przekop, A.; Schultz, M. R.; Kosztowny, C. J. R.; Song, K.; Lindell, M. C.; Hilburger, M. W.; Rudd, M. T. Design and Analysis of Buckling-Critical Large-Scale Sandwich Composite Cylindrical Test Articles. **2020**, No. November.

80. Wagner, H. N. R.; Hühne, C.; Rohwer, K.; Niemann, S.; Wiedemann, M. Stimulating the Realistic Worst Case Buckling Scenario of Axially Compressed Unstiffened Cylindrical Composite Shells. *Compos. Struct.* **2017**, *160*, 1095–1104. https://doi.org/10.1016/j.compstruct.2016.10.108.

81. Ali, H. Q.; Wagner, H. N. R.; Akalın, C.; Tabrizi, I. E.; Hühne, C.; Yildiz, M. Buckling and Fracture Analysis of Thick and Long Composite Cylinders with Cutouts under Axial Compression: An Experimental and Numerical Campaign. *Compos. Struct.* **2023**, *324* (April), 117530. https://doi.org/10.1016/j.compstruct.2023.117530.

82. Tennyson, R. C.; Muggeridge, D. B. Buckling of Axisymmetric Imperfect Circular Cylindrical Shells Underaxial Compression. *AIAA J.* **1969**, *7* (11), 2127–2131. https://doi.org/10.2514/3.5568.

83. Arbocz, J. Imperfection Data Bank, a Mean To Obtain Realistic Buckling Loads. **1982**, 535–567. https://doi.org/10.1007/978-3-642-49334-8_19.

84. Kriegesmann, B.; Rolfes, R.; HÜhne, C.; Teßmer, J.; Arbocz, J. Probabilistic Design of Axially Compressed Composite Cylinders with Geometric and Loading Imperfections. *Int. J. Struct. Stab. Dyn.* **2010**, *10* (4), 623–644. https://doi.org/10.1142/S0219455410003658.

85. Elishakoff, I.; Van Manent, S.; Vermeulen, P. G.; Arbocz, J. First-Order Second-Moment Analysis of the Buckling of Shells with Random Imperfections. *AIAA J.* **1987**, *25* (8), 1113–1117. https://doi.org/10.2514/3.9751.

86. Deml, M.; Wunderlich, W. Direct Evaluation of the "worst" Imperfection Shape in Shell Buckling. *Comput. Methods Appl. Mech. Eng.* **1997**, *149* (1–4), 201–222. https://doi.org/10.1016/S0045-7825(97)00055-8.

87. Hilburger, M. W.; Starnes, J. H. Effects of Imperfections of the Buckling Response of Composite Shells. *Thin-Walled Struct.* **2004**, *42* (3), 369–397. https://doi.org/10.1016/j.tws.2003.09.001.

88. Kriegesmann, B.; Hilburger, M. W.; Rolfes, R. The Effects of Geometric and Loading Imperfections on the Response and Lower-Bound Buckling Load of a Compression-Loaded Cylindrical Shell. *53rd AIAA/ASME/ASCE/AHS/ASC Struct. Struct. Dyn. Mater. Conf. 2012* **2012**, No. April, 1–10. https://doi.org/10.2514/6.2012-1864.

89. Degenhardt, R.; Bethge, A.; Kling, A.; Zimmermann, R.; Rohwer, K.; Klein, H.; Tessmer, J.; Calvi, A. PROBABILISTIC APPROACH FOR IMPROVED BUCKLING KNOCK-DOWN FACTORS OF CFRP CYLINDRICAL SHELLS DLR , Institute of Composite Structures and Adaptive Systems ,. **2007**, 3009–3018.

90. Kepple, J.; Herath, M. T.; Pearce, G.; Gangadhara Prusty, B.; Thomson, R.; Degenhardt, R. Stochastic Analysis of Imperfection Sensitive Unstiffened Composite Cylinders Using Realistic Imperfection Models. *Compos. Struct.* **2015**, *126*, 159–173. https://doi.org/10.1016/j.compstruct.2015.02.063.

91. Zimmermann, R. Buckling Research for Imperfection Tolerant Fiber Composite Structures. *Spacecr. Struct. Mater. Mech. Eng. Proc. Conf. held by ESA, CNES DARA Noordwijk, 27-29 March 1996*.

92. MATLAB 9.6.0.1072779 (R2019a). The MathWorks Inc.; 2024: Natick, Massachusetts.

93. Barbero, E. J. *Finite Element Analysis of Composite Materials Using Abaqus*^{TM}; 2013. https://doi.org/10.1201/b14788.

94. Barbero, E. J. *Finite Element Analysis of Composite Materials Using ANSYS*, 2nd ed.; 2014; Vol. 3.

95. Khennane, A. *Introduction to FEA Using Matlab and ABAQUS*; 2013.

96. ANSYS® Academic Research Mechanical, Release 17.2. ANSYS Inc.

97. Belegundu, A. D.; Tirupathi R. Chandrupatla. *Optimization Concepts and Applications in Engineering*, 3rd ed.; Cambridge University Press, 2019; Vol. 34. https://doi.org/https://doi.org/10.1017/9781108347976.

98. Rao, S. S. *Engineering Optimization Theory and Practice*, 5th ed.; John Wiley & Sons, 2019. https://doi.org/10.1002/9781119454816.

99. Thomas Weise. Global Optimization Algorithms Theory and Application. **2008**.

100. Walker, M.; Adali, S.; Verijenko, V. Optimization of Symmetric Laminates for Maximum Buckling Load Including the Effects of Bending Twisting Coupling. *Comput. Struct.* **1996**, *58* (2), 313–319. https://doi.org/10.1016/0045-7949(95)00138-7.

101. Aiello, M. A.; Ombres, L. Maximum Buckling Loads for Unsymmetric Thin Hybrid Laminates under In-Plane and Shear Forces. *Compos. Struct.* **1996**, *36* (1–2), 1–11. https://doi.org/10.1016/S0263-8223(96)00047-5.

102. Adali, S.; Richter, A.; Verijenko, V. E. Optimization of Shear-Deformable Laminated Plates under Buckling and Strength Criteria. *Compos. Struct.* **1997**, *39* (3–4), 167–178. https://doi.org/10.1016/S0263-8223(97)00111-6.

103. Walker, M. Optimal Design of Symmetric Laminates with Cut-Outs for Maximum Buckling Load. *Comput. Struct.* **1999**, *70* (3), 337–343. https://doi.org/10.1016/S0045-7949(98)00167-9.

104. Weaver, P. M. Design of Laminated Composite Cylindrical Shells under Axial Compression. *Compos. Part B Eng.* **2000**, *31* (8), 669–679. https://doi.org/10.1016/S1359-8368(00)00029-9.

105. Spallino, R.; Thierauf, G. Thermal Buckling Optimization of Composite Laminates by Evolution Strategies. *Comput. Struct.* **2000**, *78* (5), 691–697. https://doi.org/10.1016/S0045-7949(00)00050-X.

106. Foldager, J. P.; Hansen, J. S.; Olhoff, N. Optimization of the Buckling Load for Composite Structures Taking Thermal Effects into Account. *Struct. Multidiscip. Optim.* **2001**, *21* (1), 14–31. https://doi.org/10.1007/s001580050164.

107. Le Riche, R.; Haftka, R. T. Optimization of Laminate Stacking Sequence for Buckling Load Maximization by Genetic Algorithm. *AIAA J.* **1993**, *31* (5), 951–956. https://doi.org/10.2514/3.11710.

108. Gantovnik, V. B.; Gürdal, Z.; Watson, L. T. A Genetic Algorithm with Memory for Optimal Design of Laminated Sandwich Composite Panels. *Compos. Struct.* **2002**, *58* (4), 513–520. https://doi.org/10.1016/S0263-8223(02)00128-9.

109. Montemurro, M.; Izzi, M. I.; El-Yagoubi, J.; Fanteria, D. Least-Weight Composite Plates with Unconventional Stacking Sequences: Design, Analysis and Experiments. *J. Compos. Mater.* **2019**, *53* (16), 2209–2227. https://doi.org/10.1177/0021998318824783.

110. Ghasemi, A. R.; Tabatabaeian, A.; Hajmohammad, M. H.; Tornabene, F. Multi-Step Buckling Optimization Analysis of Stiffened and Unstiffened Polymer Matrix Composite Shells: A New Experimentally Validated Method. *Compos. Struct.* **2021**, *273* (April), 114280. https://doi.org/10.1016/j.compstruct.2021.114280.

111. Miller, B.; Ziemiański, L. Optimization of Dynamic and Buckling Behavior of Thin-Walled Composite Cylinder, Supported by Nature-Inspired Agorithms. *Materials (Basel).* **2020**, *13* (23), 1–18. https://doi.org/10.3390/ma13235414.

112. Soremekun, G.; Gürdal, Z.; Haftka, R. T.; Watson, L. T. Composite Laminate Design Optimization by Genetic Algorithm with Generalized Elitist Selection. *Comput. Struct.* **2001**, *79* (2), 131–143. https://doi.org/10.1016/S0045-7949(00)00125-5.

113. Dynardo GmbH. Methods for Multi-Disciplinary Optimization and Robustness Analysis (Handbook). **2020**.

114. Wagner, H.; Köke, H.; Dähne, S.; Hühne, C.; Niemann, S.; Khakimova, R. Decision Tree-Based Machine Learning to Optimize the Laminate Stacking of Composite Cylinders for Maximum Buckling Load and Minimum Imperfection Sensitivity. *Compos. Struct.* **2019**, *220* (July), 45–63.

115. Almeida, J. H. S.; Tonatto, M. L. P.; Ribeiro, M. L.; Tita, V.; Amico, S. C. Buckling and Post-Buckling of Filament Wound Composite Tubes under Axial Compression: Linear, Nonlinear, Damage and Experimental Analyses. *Compos. Part B Eng.* **2018**, *149* (May), 227–239. https://doi.org/10.1016/j.compositesb.2018.05.004.

116. Almeida, J. H. S.; Ribeiro, M. L.; Tita, V.; Amico, S. C. Damage Modeling for Carbon Fiber/Epoxy Filament Wound Composite Tubes under Radial Compression. *Compos. Struct.* **2017**, *160*, 204–210. https://doi.org/10.1016/j.compstruct.2016.10.036.

APPENDIX A

PRODUCED G-CODE FOR PLATE WINDING

```
;increment the line numbers (the block numbers after 'N') by 2
;Created by CADWIND
;goto pattern start point
;G01=linear interpolation
;G90=aboslute positioning
;X0=position cross-carriage first in zero position to avoid collison
;F60=60mm/min
G01 G90 Y0 F10000
;go to the program start point
X340.000 B0.000 F10000
Y0.000
M0
G91 G64 F50000
;program data
;all the positions of the first cycle
A18089.6992 X320.0000 ;F54008.45
A18089.6992 X-320.0000 ;F54008.45
A18089.6993 X320.0000 ;F54008.45
A18089.6992 X-320.0000 ;F54008.45
A18089.7031 X320.0000 ;F54008.45
A18089.7031 X-320.0000 ;F54008.45
A89.7032 ;F53999.85
;jump to the begin of the first cycle until all cycles are done
;decrease Variable #60 by 1 and jump to N1 if greater then zero
#60=#60-1
IF[#60>0]GOTO1
N2 M30 ;program end
```

APPENDIX B

CPRODUCED G-CODE FOR REFERANCE ROD WINDING

;increment the line numbers (the block numbers after 'N') by 2
;Created by CADWIND

;goto pattern start point

;G01=linear interpolation
;G90=aboslute positioning
;X0=position cross-carriage first in zero position to avoid collison
;F60=60mm/min
G01 G90 Y0 F10000

;go to the program start point
X799.479 B88.200 F10000

;last position cross-carriage to avoid collison
Y-165.000

;Pause and wait for fibre attachment
M0

;switch to G91=relative positioning. G64 for smooth movement
G91 G64 F50000

;load Variable #60 with the number of cycles
#60=14

;mark this point of the program with a label

N1

;program data
;all the positions of the first cycle
A333.0000 X216.6817 ;F55005.68
A981.0000 X638.3295 ;F55005.76
A171.0000 X111.2759 ;F55003.29
A261.0000 X169.8319 ;F55005.73
A117.0000 X76.1250 ;F55009.08
A99.0000 X64.4255 ;F55001.84
A90.0000 X58.5560 ;F55010.20
A9.0000 X5.8629 ;F52416.43
A9.0000 X5.8563 ;F39513.52
A9.0000 X5.8496 ;F26619.20
A9.0000 X5.8599 ;F13745.51
A9.0000 X-4.3275 B-0.0595 ;F17307.67
A9.0000 X-4.2198 B-0.0617 ;F29155.90
A9.0000 X-4.0972 B-0.0638 ;F40871.58
A9.0000 X-3.9954 B-0.0662 ;F52516.05
A9.0000 X-3.8882 B-0.0685 ;F58825.36
A9.0000 X-3.7896 B-0.0710 ;F58593.29
A9.0000 X-3.6924 B-0.0736 ;F58369.64
A9.0000 X-3.6038 B-0.0764 ;F58170.03
A9.0000 X-3.5106 B-0.0792 ;F57964.76
A9.0000 X-3.4263 B-0.0822 ;F57782.92
A9.0000 X-3.3441 B-0.0854 ;F57609.56
A9.0000 X-3.2581 B-0.0886 ;F57431.93
A9.0000 X-3.1876 B-0.0921 ;F57289.67
A9.0000 X-3.1200 B-0.0958 ;F57155.70
A9.0000 X-3.0420 B-0.0996 ;F57004.36
A9.0000 X-2.9869 B-0.1038 ;F56899.73
A9.0000 X-2.9086 B-0.1078 ;F56753.59
A9.0000 X-2.8530 B-0.1124 ;F56652.39
A9.0000 X-2.8010 B-0.1173 ;F56559.25

A9.0000 X-2.7393 B-0.1222 ;F56450.61
A9.0000 X-2.6876 B-0.1276 ;F56361.61
A9.0000 X-2.6331 B-0.1332 ;F56269.28
A9.0000 X-2.5955 B-0.1395 ;F56206.91
A9.0000 X-2.5486 B-0.1459 ;F56130.23
A9.0000 X-2.5057 B-0.1528 ;F56061.40
A9.0000 X-2.4670 B-0.1602 ;F56000.33
A9.0000 X-2.4257 B-0.1680 ;F55936.04
A9.0000 X-2.3887 B-0.1764 ;F55879.64
A9.0000 X-2.3558 B-0.1856 ;F55830.50
A9.0000 X-2.3342 B-0.1959 ;F55799.09
A9.0000 X-2.3040 B-0.2066 ;F55755.16
A9.0000 X-2.2716 B-0.2179 ;F55708.91
A9.0000 X-2.2570 B-0.2311 ;F55689.38
A9.0000 X-2.2275 B-0.2444 ;F55648.77
A9.0000 X-2.2159 B-0.2601 ;F55634.66
A9.0000 X-2.1896 B-0.2760 ;F55599.84
A9.0000 X-2.1877 B-0.2954 ;F55600.83
A9.0000 X-2.1649 B-0.3149 ;F55572.45
A9.0000 X-2.1600 B-0.3380 ;F55570.54
A9.0000 X-2.1472 B-0.3627 ;F55558.28
A9.0000 X-2.1464 B-0.3915 ;F55564.13
A9.0000 X-2.1375 B-0.4227 ;F55559.99
A9.0000 X-2.1406 B-0.4594 ;F55574.87
A9.0000 X-2.1360 B-0.4996 ;F55580.94
A9.0000 X-2.1433 B-0.5473 ;F55607.26
A9.0000 X-2.1432 B-0.6006 ;F55626.86
A9.0000 X-2.1552 B-0.6644 ;F55669.59
A9.0000 X-2.1595 B-0.7367 ;F55708.51
A9.0000 X-2.1697 B-0.8229 ;F55766.07
A9.0000 X-2.1791 B-0.9243 ;F55836.42
A9.0000 X-2.2073 B-1.0524 ;F55957.77
A9.0000 X-2.2085 B-1.1962 ;F56063.42
A9.0000 X-2.2355 B-1.3834 ;F56256.66

A9.0000 X-2.2617 B-1.6161 ;F56517.08
A9.0000 X-2.2810 B-1.9042 ;F53755.18
A9.0000 X-2.3063 B-2.2768 ;F45374.32
A9.0000 X-2.3442 B-2.7752 ;F37770.59
A9.0000 X-2.3622 B-3.4109 ;F31379.44
A9.0000 X-2.3993 B-4.2925 ;F25803.75
A9.0000 X-2.4362 B-5.4939 ;F21274.42
A9.0000 X-2.4729 B-7.1238 ;F17800.59
A9.0000 X-2.5160 B-9.2835 ;F15324.23
A9.0000 X-2.5588 B-11.8431 ;F13763.92
A9.0000 X-2.6017 B-14.1914 ;F12941.09
A9.0000 X-2.6443 B-15.2232 ;F12685.71
A9.0000 X-2.7069 B-14.3766 ;F12902.96
A9.0000 X-2.7496 B-12.0247 ;F13714.22
A9.0000 X-2.8121 B-9.4827 ;F15230.41
A9.0000 X-2.8684 B-7.2808 ;F17691.08
A9.0000 X-2.9314 B-5.6102 ;F21181.49
A9.0000 X-2.9878 B-4.3682 ;F25813.82
A9.0000 X-3.0645 B-3.4825 ;F31399.66
A9.0000 X-3.1349 B-2.8158 ;F38115.09
A9.0000 X-3.2057 B-2.3132 ;F45894.08
A9.0000 X-3.2834 B-1.9322 ;F54626.27
A9.0000 X-3.3617 B-1.6346 ;F58471.11
A9.0000 X-3.4470 B-1.4014 ;F58432.02
A9.0000 X-3.5265 B-1.2107 ;F58449.24
A9.0000 X-3.6262 B-1.0621 ;F58564.76
A9.0000 X-3.7135 B-0.9344 ;F58683.20
A9.0000 X-3.8147 B-0.8313 ;F58860.76
A9.0000 X-3.9102 B-0.7423 ;F59043.15
A9.0000 X-4.0129 B-0.6679 ;F59259.00
A9.0000 X-4.1299 B-0.6062 ;F59523.76
A9.0000 X-4.2412 B-0.5511 ;F59785.73
A9.0000 X-4.3602 B-0.5039 ;F60078.29
A9.0000 X-4.4803 B-0.4623 ;F60383.54

A9.0000 X-4.6080 B-0.4261 ;F60718.94
A9.0000 X-4.7305 B-0.3931 ;F61048.95
A9.0000 X-4.8738 B-0.3655 ;F61447.29
A9.0000 X-5.0121 B-0.3398 ;F61694.15
A9.0000 X-5.1516 B-0.3166 ;F60418.81
A9.0000 X-5.3058 B-0.2965 ;F59096.56
A9.0000 X-5.4615 B-0.2780 ;F57848.27
A9.0000 X-5.6189 B-0.2610 ;F56666.06
A9.0000 X-5.7909 B-0.2460 ;F55456.78
A9.0000 X-5.9518 B-0.2315 ;F54398.55
A9.0000 X-6.1472 B-0.2196 ;F53201.36
A9.0000 X-6.3118 B-0.2069 ;F52258.56
A9.0000 X-6.5177 B-0.1968 ;F51156.10
A9.0000 X-6.6992 B-0.1862 ;F50249.06
A9.0000 X-6.9160 B-0.1775 ;F49241.00
A9.0000 X-7.1152 B-0.1686 ;F48379.05
A9.0000 X-7.3430 B-0.1609 ;F47459.64
A9.0000 X-7.5536 B-0.1531 ;F46669.59
A9.0000 X-7.7926 B-0.1464 ;F45834.05
A9.0000 X-8.0413 B-0.1401 ;F45030.37
A9.0000 X-8.2726 B-0.1336 ;F44333.28
A9.0000 X-8.5331 B-0.1280 ;F43605.33
A9.0000 X-8.7963 B-0.1226 ;F42922.83
A9.0000 X-9.0758 B-0.1177 ;F42251.04
A9.0000 X-9.3519 B-0.1128 ;F41637.18
A9.0000 X-9.6443 B-0.1083 ;F41035.19
A9.0000 X-9.9398 B-0.1039 ;F40471.26
A9.0000 X-10.2521 B-0.0999 ;F39921.18
A9.0000 X-10.5745 B-0.0961 ;F39395.24
A9.0000 X-10.9071 B-0.0925 ;F38895.14
A9.0000 X-11.2435 B-0.0889 ;F38427.92
A9.0000 X-11.6036 B-0.0857 ;F37966.90
A9.0000 X-11.9613 B-0.0825 ;F37544.55
A9.0000 X-12.3362 B-0.0795 ;F37135.62

A9.0000 X-12.7220 B-0.0766 ;F36748.54
A9.0000 X-13.1255 B-0.0739 ;F36375.74
A9.0000 X-13.5469 B-0.0713 ;F36017.34
A9.0000 X-13.9598 B-0.0687 ;F35694.47
A9.0000 X-14.4105 B-0.0664 ;F35370.50
A9.0000 X-14.8600 B-0.0640 ;F35073.69
A9.0000 X-15.3344 B-0.0618 ;F34785.58
A9.0000 X-15.8169 B-0.0597 ;F34516.74
A9.0000 X-6.6604 B-0.0047 ;F34672.35
A9.0000 X-5.8628 ;F46151.62
A261.0000 X-169.8319 ;F55005.58
A873.0000 X-568.0550 ;F55005.71
A711.0000 X-462.6451 ;F55005.53
A198.0000 X-128.8387 ;F54882.07
A9.0000 X-5.8563 ;F39522.11
A9.0000 X-5.8555 ;F26635.80
A9.0000 X-5.8562 ;F13751.48
A9.0000 X4.7058 B0.0618 ;F16186.60
A9.0000 X4.5732 B0.0641 ;F28204.46
A9.0000 X4.4477 B0.0665 ;F40094.90
A9.0000 X4.3246 B0.0689 ;F51861.43
A9.0000 X4.2061 B0.0715 ;F59606.36
A9.0000 X4.0927 B0.0742 ;F59321.41
A9.0000 X3.9841 B0.0771 ;F59054.81
A9.0000 X3.8786 B0.0801 ;F58801.70
A9.0000 X3.7782 B0.0832 ;F58566.01
A9.0000 X3.6822 B0.0865 ;F58345.67
A9.0000 X3.5890 B0.0899 ;F58136.56
A9.0000 X3.4998 B0.0935 ;F57940.49
A9.0000 X3.4145 B0.0973 ;F57757.34
A9.0000 X3.3325 B0.1013 ;F57585.00
A9.0000 X3.2554 B0.1056 ;F57426.23
A9.0000 X3.1801 B0.1101 ;F57277.12
A9.0000 X3.1091 B0.1148 ;F57134.25

A9.0000 X3.0406 B0.1198 ;F57001.81
A9.0000 X2.9766 B0.1252 ;F56880.44
A9.0000 X2.9143 B0.1309 ;F56764.58
A9.0000 X2.8566 B0.1369 ;F56659.38
A9.0000 X2.8012 B0.1433 ;F56560.31
A9.0000 X2.7482 B0.1502 ;F56467.32
A9.0000 X2.6989 B0.1576 ;F56382.41
A9.0000 X2.6524 B0.1655 ;F56303.68
A9.0000 X2.6085 B0.1740 ;F56230.74
A9.0000 X2.5670 B0.1831 ;F56163.05
A9.0000 X2.5293 B0.1931 ;F56102.60
A9.0000 X2.4934 B0.2038 ;F56046.05
A9.0000 X2.4602 B0.2154 ;F55994.77
A9.0000 X2.4301 B0.2281 ;F55949.37
A9.0000 X2.4022 B0.2420 ;F55907.98
A9.0000 X2.3768 B0.2571 ;F55871.32
A9.0000 X2.3540 B0.2738 ;F55839.42
A9.0000 X2.3340 B0.2923 ;F55812.60
A9.0000 X2.3163 B0.3127 ;F55789.98
A9.0000 X2.3007 B0.3354 ;F55771.47
A9.0000 X2.2880 B0.3607 ;F55758.40
A9.0000 X2.2779 B0.3893 ;F55750.47
A9.0000 X2.2698 B0.4213 ;F55746.85
A9.0000 X2.2639 B0.4577 ;F55748.60
A9.0000 X2.2605 B0.4991 ;F55756.38
A9.0000 X2.2603 B0.5469 ;F55772.30
A9.0000 X2.2615 B0.6018 ;F55794.41
A9.0000 X2.2661 B0.6660 ;F55827.36
A9.0000 X2.2718 B0.7408 ;F55869.54
A9.0000 X2.2812 B0.8298 ;F55928.34
A9.0000 X2.2924 B0.9359 ;F56005.06
A9.0000 X2.3058 B1.0639 ;F56107.06
A9.0000 X2.3222 B1.2203 ;F56245.85
A9.0000 X2.3407 B1.4138 ;F56436.26

A9.0000 X2.3618 B1.6566 ;F56705.09
A9.0000 X2.3857 B1.9662 ;F52270.51
A9.0000 X2.4117 B2.3673 ;F43857.07
A9.0000 X2.4403 B2.8970 ;F36402.90
A9.0000 X2.4715 B3.6096 ;F29941.40
A9.0000 X2.5056 B4.5851 ;F24512.85
A9.0000 X2.5423 B5.9338 ;F20158.78
A9.0000 X2.5815 B7.7859 ;F16891.33
A9.0000 X2.6237 B10.2156 ;F14658.40
A9.0000 X2.6684 B12.9959 ;F13322.74
A9.0000 X2.7159 B15.2537 ;F12686.34
A9.0000 X2.7666 B15.7224 ;F12588.52
A9.0000 X2.8203 B14.0717 ;F13001.42
A9.0000 X2.8764 B11.3577 ;F14048.45
A9.0000 X2.9360 B8.7254 ;F15935.64
A9.0000 X2.9988 B6.6339 ;F18845.74
A9.0000 X3.0648 B5.0920 ;F22875.27
A9.0000 X3.1337 B3.9768 ;F28044.61
A9.0000 X3.2060 B3.1665 ;F34329.27
A9.0000 X3.2820 B2.5687 ;F41699.86
A9.0000 X3.3613 B2.1196 ;F50131.10
A9.0000 X3.4443 B1.7757 ;F58791.35
A9.0000 X3.5306 B1.5076 ;F58706.16
A9.0000 X3.6211 B1.2956 ;F58722.30
A9.0000 X3.7153 B1.1249 ;F58807.68
A9.0000 X3.8132 B0.9860 ;F58943.16
A9.0000 X3.9158 B0.8715 ;F59120.04
A9.0000 X4.0215 B0.7758 ;F59327.14
A9.0000 X4.1324 B0.6955 ;F59565.17
A9.0000 X4.2476 B0.6272 ;F59829.04
A9.0000 X4.3669 B0.5687 ;F60116.56
A9.0000 X4.4907 B0.5181 ;F60427.44
A9.0000 X4.6201 B0.4743 ;F60764.84
A9.0000 X4.7536 B0.4358 ;F61124.23

A9.0000 X4.8927 B0.4021 ;F61509.52
A9.0000 X5.0363 B0.3721 ;F61473.19
A9.0000 X5.1859 B0.3456 ;F60120.27
A9.0000 X5.3412 B0.3218 ;F58811.72
A9.0000 X5.5014 B0.3005 ;F57545.88
A9.0000 X5.6682 B0.2813 ;F56314.02
A9.0000 X5.8404 B0.2639 ;F55128.39
A9.0000 X6.0190 B0.2481 ;F53978.34
A9.0000 X6.2041 B0.2337 ;F52869.76
A9.0000 X6.3960 B0.2206 ;F51800.05
A9.0000 X6.5943 B0.2085 ;F50768.43
A9.0000 X6.7995 B0.1974 ;F49773.58
A9.0000 X7.0125 B0.1872 ;F48817.79
A9.0000 X7.2327 B0.1777 ;F47896.90
A9.0000 X7.4602 B0.1689 ;F47014.74
A9.0000 X7.6961 B0.1608 ;F46164.60
A9.0000 X7.9400 B0.1532 ;F45351.79
A9.0000 X8.1924 B0.1461 ;F44569.23
A9.0000 X8.4535 B0.1395 ;F43822.82
A9.0000 X8.7232 B0.1333 ;F43107.02
A9.0000 X9.0027 B0.1275 ;F42422.35
A9.0000 X9.2919 B0.1220 ;F41766.17
A9.0000 X9.5902 B0.1169 ;F41143.48
A9.0000 X9.8994 B0.1120 ;F40545.44
A9.0000 X10.2191 B0.1074 ;F39977.15
A9.0000 X10.5495 B0.1031 ;F39434.77
A9.0000 X10.8899 B0.0990 ;F38920.01
A9.0000 X11.2445 B0.0951 ;F38426.06
A9.0000 X11.6075 B0.0914 ;F37961.66
A9.0000 X11.9868 B0.0879 ;F37515.81
A9.0000 X12.3766 B0.0845 ;F37093.37
A9.0000 X12.7790 B0.0813 ;F36693.32
A9.0000 X13.1961 B0.0783 ;F36313.83
A9.0000 X13.6271 B0.0754 ;F35952.94

```
A9.0000 X14.0731 B0.0726 ;F35611.02
A9.0000 X14.5325 B0.0700 ;F35287.26
A9.0000 X15.0081 B0.0675 ;F34981.20
A9.0000 X15.4999 B0.0650 ;F34690.41
A10.2856 X22.3241 B0.0881 ;F33031.35
;jump to the begin of the first cycle until all cycles are done
;decrease Variable #60 by 1 and jump to N1 if greater then zero
#60=#60-1
IF[#60>0]GOTO1
N2 M30 ;program end
```

APPENDIX C

SMEARED PROPERTY CALCULATOR IN MATLAB

```
clear
clc

% function Pcr = objective_function(x)
   Nplies = 12;
   thetadt = [x(1) -x(1) x(2) -x(2) x(3) -x(3) x(4) -x(4) x(5) -x(5) x(6) -x(6)];

%     thetadt = [ 45 -45 45 -45 45 -45 45 -45 45 -45 45 -45];
%     thetadt = [ 30 -30 30 -30 30 -30 30 -30 30 -30 30 -30];
 %    thetadt = [ 30 -30 30 -30 30 -30 20 -20 20 -20 20 -20];
     disp(['Stacking sequence is equal to ', num2str(thetadt)]);

   h_ply = 0.125;
   h = Nplies * h_ply;
   Length = 800; % mm
   R_outer=11.5;
   R_inner=10;
   Torque = 2000; % N*mm
   Radi = 10.75; % mm, average radius
   E1 = 90e3; % MPa
   nu12 = 0.32;
   E2 = 8.5e3; % MPa
   G12 = 4.3e3; % MPa
   nu21 = nu12 * E2 / E1;

   Q11 = E1 / (1 - nu12 * nu21);
   Q12 = nu12 * E2 / (1 - nu12 * nu21);
   Q21 = Q12;
```

```
Q22 = E2 / (1 - nu12 * nu21);
Q66 = G12;
Q = [Q11 Q12 0; Q21 Q22 0; 0 0 Q66];
AA = zeros(3, 3);
B = zeros(3, 3);
D = zeros(3, 3);
% Calculate zbar
for i = 1:Nplies
   zbar(i) = - (h + h_ply)/2 + i*h_ply;
end
for i = 1:Nplies
   theta = thetadt(i) * pi / 180;
   m = cos(theta);
   n = sin(theta);
   T = [m^2 n^2 2*m*n; n^2 m^2 -2*m*n; -m*n m*n (m^2 - n^2)];
   Qbar = inv(T) * Q * (inv(T))';
   AA = AA + Qbar * h_ply;
   B = B + Qbar * h_ply * zbar(i);
   D = D + Qbar * (h_ply * zbar(i)^2  + h_ply^3 / 12);
end
ABD = [AA B; B D];
 Exx = (((AA(1,1)*AA(2,2))-(AA(1,2)^2))/AA(2,2))*(1/h);
Gxy = (1/h)*AA(3,3);
J = (pi/64)*((23^4)-(20^4));
I = (pi/4)*((R_outer^4)-(R_inner^4));
mass = 0.144; % kg
m_p_l = mass/Length;
  fn = 60*((1/2*pi)*(sqrt((Exx*I)/(m_p_l*Length^4))));
  A_o_t = ((Torque*Length)/(J*Gxy))*57.2957795; %rad to degree
  Pcr = (4*Exx*I*pi^2)/(Length)^2; % both end clamped.
 disp(['Exx is equal to ' num2str(Exx) ' MPa']);
disp(['Pcr is equal to ' num2str(Pcr) ' N']);
disp(['fn is equal to ' num2str(fn) ' Hz']);
disp(['Angle of twist is equal to ' num2str(A_o_t) ' degree']);
```

APPENDIX D

BUCKLING MODES

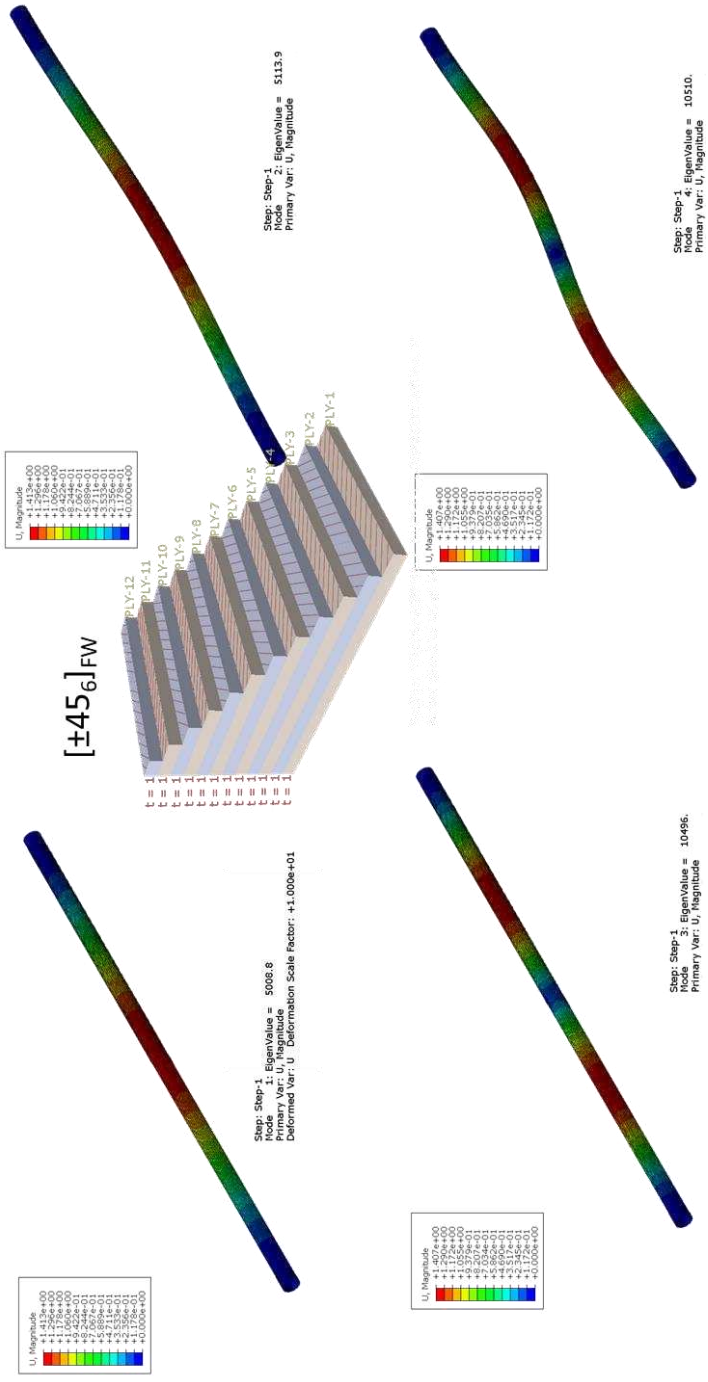

Figure D. 1. First four buckling modes of CFRP rods.

VITA

Seçkin MARTİN

EXPERIENCES

- Helicopter Rotor Blade Analysis Engineer, TAI June 2023 – Present
- Research Assistant, Izmir Institute of Techonology Mechenical Eng. Dep. May 2018 – June 2023

EDUCATION

- **Ph.D.** in English, 2024, Mechanical Engineering, İzmir Institute of Technology, IZMIR.
- **M.Sc.** in English, 2019, Mechanical Engineering, İzmir Institute of Technology, IZMIR.
- **B.Sc.** in Turkish, 2016, Mechanical Engineering, Pamukkale University, DENİZLİ.

Selected publications

- S.Martin, M. Tanoğlu, S. Dehneliler " Design, Optimization, and Manufacturing of Cylindrical Composite Structures Produced by Filament Winding Method Against Buckling Failure" , Aerospace Science and Technology, Submitted, June 2024
- S.Martin, M. Tanoğlu, S. Dehneliler, "Filament Sarım Yöntemiyle Üretilen Silindirik Kompozit Yapıların Burkulma Hasarına Karşı Optimizasyonu", SAVTEK Defense Technologies Congress, 13-15/2022.
- S.Martin, M. Antonov, "Investigation of the high temperature dry sliding wear behavior of graphene nanoplatelets reinforced aluminum matrix composites", Journal of Composite Materials, First Published December 6, 2020 (https://doi.org/10.1177/0021998320979037)
- K. Nuhoğlu, E. Aktaş, M. Tanoğlu, S. Martin et. al. "Analysis of adhesively bonded joints of laser surface treated composite primary components of aircraft structures", International Journal of Adhesion and Adhesives, August 2023 (https://doi.org/10.1016/j.ijadhadh.2023.103456)
- H. Iplikçi, M. Barışık,C. Türkdoğan, S. Martin et al, "Effects of nanosecond laser ablation parameters on surface modification of carbon fiber reinforced polymer composites Journal of Composite Materials, May 2023 (https://doi.org/10.1177/00219983231178892)